DOCTORAL THESIS IN ENGINEERING MECHANICS
STOCKHOLM, SWEDEN 2014

Transitional and turbulent fibre suspension flows

MATHIAS KVICK

KTH ROYAL INSTITUTE OF TECHNOLOGY
SCHOOL OF ENGINEERING SCIENCES

Transitional and turbulent fibre suspension flows

by

Mathias Kvick

September 2014
Technical Reports from
Royal Institute of Technology
KTH Mechanics
SE-100 44 Stockholm, Sweden

Akademisk avhandling som med tillstånd av Kungliga Tekniska Högskolan i Stockholm framlägges till offentlig granskning för avläggande av teknologie doktorsexamen den 24 Oktober 2014 kl 10.15 i sal L1, Drottning Kristinas väg 30, Kungliga Tekniska Högskolan, Stockholm.

Universitetsservice US–AB, Stockholm 2014

Mathias Kvick 2014, **Transitional and turbulent fibre suspension flows**
Wallenberg Wood Science Center & Linné FLOW Centre
KTH Mechanics
SE–100 44 Stockholm, Sweden

Abstract

In this thesis the orientation of macro-sized fibres in turbulent flows is studied, as well as the effect of nano-sized fibrils on hydrodynamic stability. The focus lies on enabling processes for new materials where cellulose is the main constituent. When fibres (or any elongated particles) are added to a fluid, the complexity of the flow-problem increases. The fluid flow will influence the rotation of the fibres, and therefore also effect the overall fibre orientation. Exactly how the fibres rotate depends to a large extent on the mean velocity gradient in the flow.

In addition, when fibres are added to a suspending fluid, the total stress in the suspension will increase, resulting in an increased apparent viscosity. The increase in stress is related to the direction of deformation in relation to the orientation of the particle, *i.e.* whether the deformation happens along the long or short axis of the fibre. The increase in stress, which in most cases is not constant neither in time nor space, will in turn influence the flow.

This thesis starts off with the orientation and spatial distribution of fibres in the turbulent flow down an inclined plate. By varying fibre and flow parameters it is discovered that the main parameter controlling the orientation distribution is the aspect ratio of the fibres, with only minor influences from the other parameters. Moreover, the fibres are found to agglomerate into streamwise streaks. A new method to quantify this agglomeration is developed, taking care of the problems that arise due to the low concentration in the experiments. It is found that streakiness, *i.e.* the tendency to agglomerate in streaks, varies with Reynolds number.

Going from fibre orientation to flow dynamics of fibre suspensions, the influence of cellulose nanofibrils (CNF) on laminar/turbulent transition is investigated in three different setups, namely plane channel flow, curved-rotating channel flow, and the flow in a flow focusing device. This last flow case is selected since it is can be used for assembly of CNF based materials. In the plane channel flow, the addition of CNF delays the transition more than predicted from measured viscosities while in the curved-rotating channel the opposite effect is discovered. This is qualitatively confirmed by linear stability analyses. Moreover, a transient growth analysis in the plane channel reveals an increase in streamwise wavenumber with increasing concentration of CNF. In the flow focusing device, *i.e.* at the intersection of three inlets and one outlet, the transition is found to mainly depend on the Reynolds number of the side flow. Recirculation zones forming downstream of two sharp corners are hypothesised to be the cause of the transition. With that in mind, the two corners are given

a larger radius in an attempt to stabilise the flow. However, if anything, the flow seems to become unstable at a smaller Reynolds number, indicating that the separation bubble is not the sole cause of the transition. The choice of fluid in the core flow is found to have no effect on the stability, neither when using fluids with different viscosities nor when a non-Newtonian CNF dispersion was used. Thus, Newtonian model fluids can be used when studying the flow dynamics in this type of device.

As a proof of concept, a flow focusing device is used to produce a continuous film from CNF. The fibrils are believed to be aligned due to the extensional flow created in the setup, resulting in a transparent film, with an estimated thickness of 1 μm.

Descriptors: Fluid mechanics, fibre suspension, turbulence, laminar-turbulent transition, image analysis, hydrodynamic stability, cellulose nanofibrils.

Mathias Kvick 2014, **Transient och turbulent flöde av fiber-suspensioner**

Wallenberg Wood Science Center & Linné FLOW Centre
KTH Mechanics
SE–100 44 Stockholm, Sweden

Sammanfattning

I denna avhandling studeras orientering av makro-fibrer i turbulent flöde samt effekten av nano-fibrer på transitionen mellan laminärt och turbulent flöde. När fibres (eller andra avlånga partiklar) tillsätts i en vätska ökar komplexiteten på flödesproblemet. Flödet påverkar rotationen och positionen av fibrerna och har därför en direkt inverkan på orienteringen. Exakt hur fibrerna påverkas beror framför allt på hastighetsgradienten i flödet.

På grund av att fibrerna inte deformeras på samma sätt som vätskan runt omkring dem, samt uppkomsten av skjuvspänningar på fibrernas ytor, uppstår en extra spänning i suspensionen, vilket direkt resulterar i en ökad viskositet. Storleken på den extra spänningen beror på deformationens riktning i relation till fibrernas orientering, den beror alltså på om deformationen sker längs fiberns långa eller korta axel. Denna spänningsökning, som troligen inte är konstant varken i tiden eller rummet, kommer i sin tur att påverka flödet.

Denna avhandling fokuserar inledningsvis på orienteringen samt den rumsliga fördelningen av fibrer i ett turbulent flöde nedför ett lutande plan. Genom att variera fiber och flödes parametrar upptäcks att det är fibrernas slankhet som till största delen bestämmer deras orientering. Övriga faktorer orsakar endast små variationer. Dessutom observeras det att fibrerna agglomererar i stråk i strömningsriktningen. För att analysera dessa stråk utvecklas en ny metod, vilken löser de problem som uppstår på grund av låg fiberkoncentration. Det visar sig att stråkigheten (fibrernas tendens att agglomerera i stråk) varierar med Reynolds tal och har ett maximum inom det område som undersöks.

Inverkan av nano-fibrillär cellulosa (CNF) på laminär/turbulent transition undersöks i tre olika fall: flödet i en plan kanal, flödet i en krökt och roterande kanal, samt flödet i en flödesfokuseringsapparat. Det sista flödesfallet valdes på grund av dess användbarhet i produktion av CNF baserade material. Genom att tillsätta CNF i det plana kanalflödet fördröjs transitionen mer än vad som förutsägs från viskositetsmätningar medan i den krökta, roterande, kanalen observeras det motsatta. Detta bekräftas kvalitativt av linjära stabilitets analyser, inkluderadande transient tillväxt. Dessutom upptäcks, genom analys av den transienta tillväxten, att våglängden i strömningsled minskar med ökad koncentration av fibrer.

I flödesfokuseringsapparaten, alltså i korsningen mellan tre inlopp och ett utlopp, ses att transitionen mellan stationär och oscillerande strömning till största delen beror på Reynolds tal för flödena i sidokanalerna. En hypotes är att de återcirkulationsområden som skapas nedströms av två skarpa hörn är

orsaken till transitionen, därför rundas dessa hörn i ett försök att stabilisera flödet. Den förväntade stabiliseringen sker dock inte, vilket tyder på att något annat är ansvarigt för transitionen. Valet av vätska i mittenflödet har ingen effekt på stabiliteten, varken när endast viskositeten ändras eller när en icke Newtonsk CNF-blandning används.

Avhandlingen avslutas med att bevisa att det är möjligt att använda flödesfokusering i produktionen av en kontinuerlig film som enbart består av CNF. Den resulterande filmen är transparant och har en uppskattad tjocklek på 1 μm.

Nyckelord: Strömningsmekanik, fiber-suspension, turbulens, bild analys, hydrodynamisk stabilitet, nano-fibrillär cellulosa.

Preface

In this thesis, the orientation and distribution of fibres in turbulent flows as well as the effect of fibres on the laminar-turbulent transition are studied. The thesis is divided into two parts. The first part provides an introduction to fibre suspension flows, with focus on orientation, rheology and hydrodynamic stability in different configurations. The second part of the thesis consists of seven papers, where the layout of the published papers have been adjusted to match the format of the rest of the thesis. Part II consists of the following seven papers:

Paper 1 Kvick, M., Håkansson, K. M. O., Lundell, F., Prahl Wittberg, L. & Söderberg, L. D. 2014 Fibre orientation and fibre streaks in turbulent wall bounded flow *To be submitted*

Paper 2 Håkansson, K. M. O., Kvick, M., Lundell, F., Prahl Wittberg, L. & Söderberg, L. D. 2013 Measurement of width and intensity of particle streaks in turbulent flows. *Exp. Fluids* **54** (6), 1555

Paper 3 Kvick, M., Lundell, F., Prahl Wittberg, L. & Söderberg, L. D. 2013 Effect of fibrils on curvature- and rotation-induced hydrodynamic stability. *Acta Mech.* **224** (10), 2249–2261[1]

Paper 4 Kvick, M., Lundell, F., Prahl Wittberg, L. & Söderberg, L. D. 2013 Effect of fibres on hydrodynamic stability in a curved rotating channel. In *8th Int. Conf. on Multiphase Flow*, *ICMF2013* 674. Jeju, Korea

Paper 5 Kvick, M., Watanabe, K., Miyazaki, M., Matsubara, M., Lundell, F. & Söderberg, L. D. 2014 Fibre suspension flow in a plane channel: transition delay by cellulose nanofibrils *Manuscript*

Paper 6 Kvick, M., Lundell, F., Prahl Wittberg, L. & Söderberg, L. D. 2014 Stability of the flow in a flow-focusing device *Manuscript*

Paper 7 Kvick, M., Lundell, F. & Söderberg, L. D. 2014 Producing film from cellulose nanofibrils using a flow focusing device *Manuscript*

September 2014, Stockholm
Mathias Kvick

[1] An erratum of the publication has been submitted due to a calculation error of the effective viscosity. In this thesis the corrected version is used.

Related publications The following list contains publications where the author has performed parts of the work that are not included in this thesis:

International journals

Kvick, M., Håkansson, K., Lundell, F., Söderberg, L. & Prahl Wittberg, L. 2010 Streak formation and fibre orientation in near wall turbulent fibre suspension flow. *ERCOFTAC Bull.* **84**, 19–22

Carlsson, A., Håkansson, K., Kvick, M., Lundell, F. & Söderberg, L. D. 2011 Evaluation of steerable filter for detection of fibers in flowing suspensions. *Exp. Fluids* **51**, 987–996

Håkansson, K. M. O., Fall, A. B., Lundell, F., Yu, S., Krywka, C., V., R. S., Santoro, G., Kvick, M., Prahl Wittberg, L., Wågberg, L. & Söderberg, L. D. 2014 Hydrodynamic alignment and assembly of nanofibrils resulting in strong cellulose filaments. *Nat. Commun.* **5**, 4018

Refereed conference proceedings

Kvick, M., Håkansson, K., Lundell, F., Söderberg, L. & Prahl Wittberg, L. 2010 Fibre streaks in wall bounded turbulent flow. In *7th Int. Conf. on Multiphase Flow*, *ICMF2010* 6.5.4. Tampa, USA

It doesn't matter how beautiful your theory is, it doesn't matter how smart you are. If it doesn't agree with experiment, it's wrong.

– Richard P. Feynman

Contents

Part I

Overview & summary

CHAPTER 1

Introduction

1.1. Background

The introduction of plastics into our society in the middle of the 20th century provided the necessary components to produce cheap, strong, durable materials for a wide range of applications (Meikle 1995). By adding fibres of different kinds, at first cellulose fibres that later would be followed by glass fibres, the strength of the materials increased even more. However, in spite of the excellent material properties there is a major drawback when using plastics and composites containing plastics. Due to the strong connection between the components it is very hard to separate and recycle these types of materials (Shent *et al.* 1999), in addition they are produced from a non-renewable resource, namely oil, thereby resulting in a sustainability problem.

Due to increased environmental awareness at the end of the 20th century, the development of bio-composites formed a logical step in order to replace the oil-based components with biopolymer matrices and natural fibres. By using bio-based, biodegradable materials made from renewable resources, sustainability no longer becomes an issue. However, the thermal and mechanical properties of the bio-composites are not as good as those for plastics, and in many cases the substitution of plastics by bio-based composites is not convenient or even possible (Mohanty *et al.* 2000). As a compromise between the two materials, wood-plastic composites were reintroduced and is today extensively used, *e.g.* in the car industry. These wood-plastic composites are often referred to as "green composites" (Berglund & Peijs 2010). How "green" these materials actually are can be questioned (Gerngross & Slater 2000), however, there is most likely an environmental benefit when using natural fibres instead of glass- or carbon-fibres (Shen & Patel 2008). The amount of CO_2 released by combustion of the material after its lifecycle is of the same order as the amount collected during the growth of the fibrous raw material (Ashori 2008). The most common choice of natural fibres are cellulose fibres, that can be extracted from a variety of plants. Wood is one of the typical sources and has been used for a long time as a raw material for cellulose fibres. In this thesis, the flows of cellulosic fibre suspensions are investigated with focus on fibre orientation and flow dynamics, with material processing as the underlying motivation.

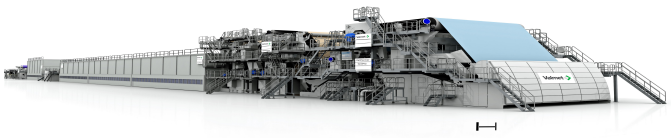

FIGURE 1.1. **Paper Machine.** Large scale assembly device for fibrous materials, here illustrated by a paper machine[1] (the scale bar is ~ 1 m).

1.2. Processing of bio-based materials

In a fibre-matrix composite, the mechanical properties of the material depend on the properties of the fibres and the strength of the connection between the fibres and the matrix. Due to its anisotropy a fibre will carry most weight in its elongated direction, indicating the importance of the orientation of the fibres in the matrix (Cox 1952) and different orientation of the fibres can be sought depending on the application. Some of the practical problems related to fibre orientation in composites are described in Rowbotham (1948), examining several components form the automotive industry.

There are a plenitude of processes in which products are manufactured from fibrous raw materials. One of the oldest and most widely used being the manufacturing of paper, where a suspension consisting of 1% cellulose fibres and 99% water is formed into a thin sheet whereafter the water is drained through pressing and drying. The orientation of the fibres in the resulting paper is to a large extent decided by the part of the process that takes place immediately before the forming of the sheet. Many other production facilities for composites follows the same general steps as the paper machine; (i) the suspension is mixed and transported to the beginning of the assembly unit (see chapter 3), (ii) the assembly unit distributes the suspension (or matrix-fibre mixture) according to its design (see chapter 2) and (iii) the fibres and matrix are locked into their position (see chapter 4). The time spent in each of these steps depends on the process and the material used. The size and output rate of these processes vary from the paper machine that is 10 m wide and several hundreds meters long, with production rates around 30 m/s (Fig. 1.1) down to microfluidic devices with velocities of the order of 0.1 m/s (Fig. 1.2). Independent on the type of process, one of the main goals is always to run the production with maximum efficiency while maintaining the desired quality of the end product. This results in a need to understand the flow of fibre suspensions, either to

[1] Valmet Paper

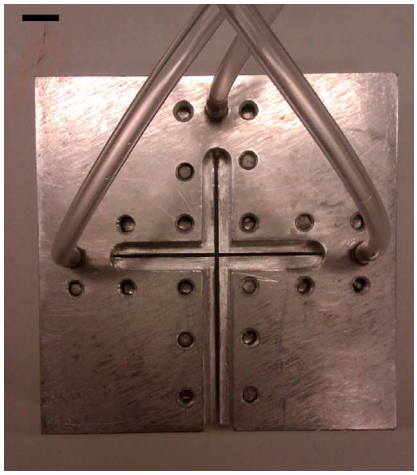

FIGURE 1.2. **Microfluidic assembly unit.** Microfluidic flow device for assembly of cellulose nanofibrils[2] (the scale bar is 10 mm).

ensure that there are no undesired influences on the process itself, or in order to use the knowledge as a tool to improve the properties of the product.

1.3. The Swedish forest as a material source

More than half of the land area in Sweden is covered by forests and it is therefore not surprising that wood and wood-based products are one of Swedens main exports (122 billion SEK 2012, $\sim$ 10% of the value of the total export (Skogsstyrelsen 2013)).

A large part of the Swedish forest has for a long time been used to produce paper. However, in recent years the demand on newsprint has declined. In Sweden the production of copy-paper has also reduced while packaging is still increasing (Skogsindustrierna 2014). In order to keep or to increase the value of the forest, research regarding more advanced uses of raw materials originating from the forest is necessary.

Recently, research in the area of wood-fibre based products has been partly focused into the use of cellulose nanofibrils (CNF) in various applications (Eichhorn *et al.* 2010). CNF consists of bundles of cellulose polymers which together form fibrils with diameters of $\sim$ 20 nm and lengths of $\sim$ 4 μm. The production of CNF has been known since the 1980s when Turbak *et al.* (1983) described a possible production method and potential markets. However, at that time, the energy consumption of the process was not commercially viable. Recently an improved method where paper pulp is first subjected to an

[2]Håkansson *et al.* (2014)

enzymatic pre-treatment followed by high pressure homogenisation has been developed (Pääkkö *et al.* 2007), effectively reducing the production cost for CNF, resulting in an increased interest in its possible uses.

1.4. Aim of the present thesis

The underlying motivation for the work carried out in this thesis is to obtain knowledge enabling new products from the forest sector. It is already well known that the structure of a fibrous material determines its material properties, and the structure is to a large extent set by the flow in the (continuous) assembly process. The aim of this thesis is therefore to increase the knowledge on how flows affect fibres and how fibres affect flows.

The first point of interest is to understand what controls the orientation and spatial distribution of fibres in a turbulent flow close to a wall. This is done in order to provide experimental data for model development and verification. This is of importance in all processes where a fibre suspension flows close to a wall, in particular papermaking.

When investigating how the presence of fibres affects the flow, the focus is on the laminar/turbulent and steady/oscillatory transition of CNF suspensions in different flow situations. The main question is whether viscosity measurements of the fibre suspensions are sufficient to predict changes in the transition. The theoretical counterpart is to find out to what extent a simple rheological model can predict the effect of fibres on the laminar/turbulent transition. In the case of steady/oscillatory transition in a flow focusing device, the parameter governing the onset of oscillations is sought. In this context, it is also of interest to understand if the use of model fluids is possible when investigating the flow dynamics, or if shear thinning and extensional viscosity of the CNF suspension is of importance.

The last question handled in this thesis is if it is possible to utilise one of the flow cases in order to produce films from CNF with controlled orientation. If successful, continuous films could be made with a defined orientation and thickness and therefore also a tuneable heat transfer or strength.

CHAPTER 2

Fluids, fibres & walls

In this chapter the behaviour of fibres in a turbulent shear flow is discussed with an emphasis on the parameters affecting the fibre orientation. Selected results from Paper 1 & 2 are presented in this context. Furthermore the concept of rheology is introduced and it is described how fibres influence the viscosity of a suspension, where the orientation of the fibres will be of importance.

2.1. Fluid flow

The flow of an incompressible fluid in any geometry can, with the correct boundary conditions, be described by the momentum and continuity equations:

$$\frac{\partial u_i}{\partial t} + u_j \frac{\partial u_i}{\partial x_j} = -\frac{1}{\rho}\frac{\partial p}{\partial x_i} + \frac{1}{\rho}\frac{\partial \sigma_{ij}}{\partial x_j} \tag{2.1}$$

$$\frac{\partial u_i}{\partial x_j} = 0, \tag{2.2}$$

where u_i are the velocities in the principal directions, ρ is the fluid density and σ_{ij} is the deviatoric stress tensor. For a Newtonian fluid, the relation between the fluid stress and strain is given by:

$$\sigma_{ij} = \mu\left(\frac{\partial u_i}{\partial x_j} + \frac{\partial u_j}{\partial x_i}\right), \tag{2.3}$$

where μ is the shear viscosity of the fluid. Solving this set of equations, *e.g.* through Direct Numerical Simulations (DNS), the flow field in many geometries can in principle be obtained. However, using DNS in order to obtain the time-resolved flow field is computationally expensive and therefore not a viable option in many cases, especially not in more complex geometries. Therefore, models with different levels of approximation are often used as a means to acquire knowledge of flows. In order to validate models, experimental results are crucial.

2.2. Fibre orientation & fibre streaks in turbulent flow

A simple geometrical model of a fibre is an elongated particle, the motion of a single ellipsoidal particle in a shear flow was first derived by Jeffery (1922),

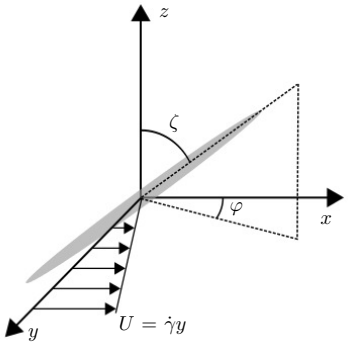

FIGURE 2.1. **Fibre coordinate system.** Coordinate system for a fibre in simple shear.

assuming creeping flow and inertia-free particles. The rotational motion of the particle is described by the angular velocities given by:

$$\dot{\varphi} = -\frac{\dot{\gamma}}{r_p^2+1}(r_p^2 \sin^2\varphi + \cos^2\varphi) \tag{2.4}$$

$$\dot{\theta} = \left(\frac{r_p^2-1}{r_p^2+1}\right)\frac{\dot{\gamma}}{4}\sin 2\phi \sin 2\theta, \tag{2.5}$$

where φ and θ are the angles describing the orientation of the particle, as depicted in Fig. 2.1, $\dot{\gamma}$ is the shear rate, where the dot indicates differentiation with respect to time and $r_p = l/d$ is the aspect ratio of the particle, where l and d is the length and diameter of the particle. This description of the rotational motion is valid only in special cases and experiments studying the orientation of fibres in various flows are needed in order to validate new models that are being incorporated into DNS (Andersson *et al.* 2012; Andrić *et al.* 2013).

In Kvick *et al.* (2014*a*), Paper 1 in this thesis, the orientation and spatial distribution of fibres in a flow down an inclined plate is investigated (see Appendix A.1 for details on the experimental setup). When fibres are introduced into a system, the complexity of the system grows quickly. In Paper 1 the number of non-dimensional numbers needed to describe the flow of a fibre suspension in a half channel is shown to increase from one (1) when considering pure fluid to six (6) when fibres are added, the non-dimensional numbers are presented in table 2.1. The parameters used to construct the non-dimensional numbers are; friction velocity ($u_\tau = \sqrt{\tau_w/\rho_f}$, where τ_w is the shear stress at the wall), height of the water layer (h), kinematic viscosity of the fluid (ν), shear rate at the wall ($\dot{\gamma}_w$), particle length and diameter (l_p and d_p), fluid and particle density (ρ_f and ρ_p) and fibre concentration per area (n_2).

$\mathrm{Re}_\tau = \frac{u_\tau h}{\nu}$	Friction Reynolds number of the bulk flow.
$\mathrm{Re}_p = \frac{\dot{\gamma}_w l_p^2}{\nu}$	Particle Reynolds number quantifying the effects of fluid inertial on particle rotation in the mean shear.
$St_p = \frac{\rho_p}{\rho_f}\mathrm{Re}_p$	Particle Stokes number quantifying the effects of particle inertia on particle rotation in the mean shear.
$n_2 l_p^2$	Mean number of particles in a square prism with side l_p.
$r_p = \frac{l_p}{d_p}$	Aspect ratio of the fibres.
$S = T_{Jeff}/T_{sed}$	Time for a Jeffery orbit over the time to sediment from a height of $l_p/2$ to the wall.

TABLE 2.1. Six non dimensional groups describing the flow of a fibre suspension in a channel, with a short description of the physical phenomena they measure.

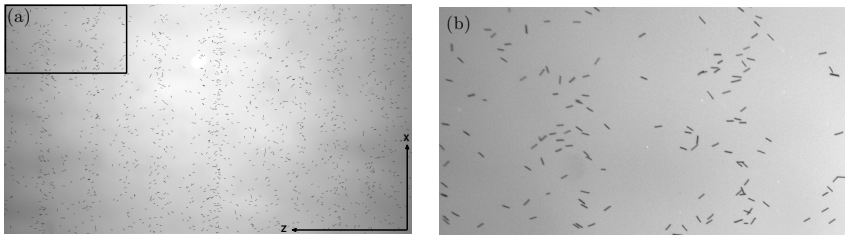

FIGURE 2.2. **Fibres in turbulent half channel flow.** a) Example of an image obtained during the experiments performed in Paper 1, the fibres have been dyed black and the flow is in positive x-direction. b) Magnification in order to visualise the orientation of the fibres. The fibres have a length of 0.5 mm.

In Paper 1 three of the non-dimensional numbers presented in table 2.1 (Re_τ, r_p and $n_2 l_p^2$) are varied independently, and images of the fibres in the flow, as the ones given in Fig. 2.2, are acquired. It is shown that the main parameter controlling the fibre orientation distribution is the fibre aspect ratio (r_p), with

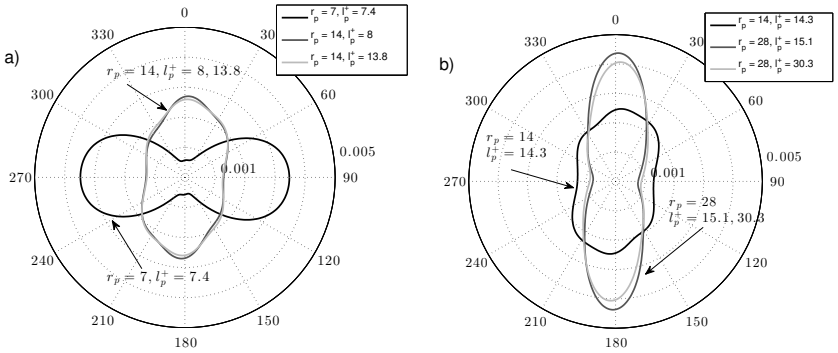

FIGURE 2.3. **Fibre orientation distributions**. Orientation distributions for fibre with aspect ratios (a) $r_p = 7, 14$ and (b) $r_p = 14, 28$ for different non-dimensional fibre lengths, l_p^+. Zero is in the streamwise- and 90∘ is the spanwise direction, respectively.

minor influences from the turbulence (Re_τ) and number concentration ($n_2 l_p^2$). It is found that fibres with aspect ratio $r_p = 28$ align in the flow direction, while shorter fibres with aspect ratio $r_p = 7$ orient in the spanwise direction. This is illustrated in Fig. 2.3 where the orientation distributions are shown for independently varied aspect ratios and non-dimensional fibre lengths (made non-dimensional with the viscous length scale). The orientations of the fibres are defined such that the angle of orientation is zero in the streamwise direction.

While it previously was mentioned that the scales of the turbulence does not have a major impact on the fibre orientation, it may influence the spatial distribution of fibres. It is well known that particles in a turbulent flow tend to agglomerate in the streamwise low-speed streaks (Kaftori *et al.* 1995; Mortensen *et al.* 2008; Zhao *et al.* 2010; Marchioli *et al.* 2010), this was also found in the experiments in Paper 1, as shown in Fig. 2.2 (to the authors knowledge the first experimental evidence of such agglomeration of fibres). There exist methods to quantify agglomeration; *e.g.* box counting (Fessler *et al.* 1994) and Voronoi analysis (Monchaux *et al.* 2010). However, these methods are found to fail at low concentrations, such as the ones used in Paper 1. Therefore, a new method was developed in Håkansson *et al.* (2013) (Paper 2). A corrected auto-correlation of images summed in the direction of the streaks is found to provide a quantitative method for both the width of the streaks and their intensity, *i.e.* streakiness (Ξ). In Paper 1 the streakiness (of the fibre streaks) was found to vary with the friction Reynolds number, as shown in Fig. 2.4a, and a maximum at which the agglomeration was strongest can be identified. Moreover, the sizes of the fibre streaks were found to be slightly larger than the size of the velocity streaks in turbulent boundary layers ($\sim 50 l^+$, where l^+ is

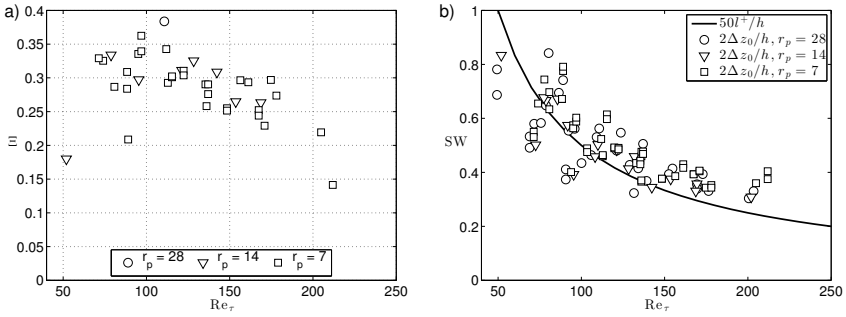

FIGURE 2.4. **Intensity and width of fibre streaks.** a) Streakiness, Ξ, as a function of the friction Reynolds number and b) width of the fibre streaks normalised with the height of the water layer. Also shown is the width of velocity streaks in a turbulent boundary layer (solid line).

the viscous length scale (Zacksenhouse *et al.* 2001)). This clearly demonstrates that the effect of turbulence on the fibres in a suspension cannot be modelled as a diffusion when the distribution of the fibres is of interest, at least not when a region close to the wall is investigated.

2.3. Rheology of fibre suspensions

So far, only the effect of the flow on the fibres has been discussed. However, since the flow affect the fibres, the fibres will in return influence the flow. The rheology (the science of the deformation and flow of matter) of a material is normally described by an equation relating the shear stress (τ) to the strain rate ($\dot{\gamma}$), which for a Newtonian fluid are related through the shear viscosity (μ) by $\tau = \mu\dot{\gamma}$. When particles are added to a Newtonian fluid, the rheology will change, since the added particles do not deform in the same manner as the surrounding fluid. The change in viscosity that occurs when particles are added is directly related to the change in stress needed to perform the same deformation as in the suspending liquid without the particles. How the addition of particles influences the rheology of the suspension depends on the physical properties of the particles; volume fraction, shape, size, particle-particle interaction and distribution. This is not studied directly in this thesis, however a model describing the rheology of fibre suspensions is being used in Paper 3, 4 & 5 and a short introduction is in order.

The increase in viscosity due to the presence of a single sphere was first derived by Einstein (1906) (as reported in Mueller *et al.* (2010)) as:

$$\mu_{sph} = \mu_l(1 + 2.5\Phi), \tag{2.6}$$

where μ_l is the dynamic viscosity of the suspending liquid and Φ is the volume fraction. In order to understand how fibre effect the rheology, we will start with a general description of the stress due to the deformation of a fluid, given by:

$$\tau_{ij} = -P\delta_{ij} + B_{ijkl}\varepsilon_{kl}, \tag{2.7}$$

where P is the isotropic contribution and is usually included into the pressure, B_{ijkl} is a tensor describing the fluid/suspension and ε_{kl} is the rate of strain tensor (Kundu & Cohen 2004). If the tensor B_{ijkl} is isotropic and symmetric, the familiar Newtonian stress for a fluid, as given in given in Eq. 2.3, can be obtained (Batchelor 1970). By using slender body theory, as is appropriate for a fibre suspension where the length is much larger than the diameter, an expression for the extra stress can be derived (Batchelor 1970; Leal & Hinch 1973):

$$\sigma^f = \mu_l \Phi \Big[Q(\boldsymbol{\varepsilon} \ : \mathbf{a_4}) + R(\boldsymbol{\varepsilon} \ \cdot \mathbf{a_2} + \mathbf{a_2} \cdot \boldsymbol{\varepsilon} \ ) + S\boldsymbol{\varepsilon} \ + \mathbf{T}\mathbf{a_2} \Big], \tag{2.8}$$

where Q, R, S and $\mathbf{T}$ are rheological parameters, Φ is the volume fraction, $\boldsymbol{\varepsilon}$ is the strain rate tensor, " : " denotes the double dot product and $\mathbf{a_4}$ and $\mathbf{a_2}$ are the fourth and second order orientation tensors for the fibres (Advani & Tucker III 1987). The rheological parameters in Eq. 2.8 are of the order (Batchelor 1971; Phan-Thien & Graham 1991; Petrie 1999):

$$Q \sim r_p^2 \tag{2.9}$$

$$R \sim r_p^{-2} \tag{2.10}$$

$$S = 2 \tag{2.11}$$

$$\mathbf{T} \sim D_r r_p^2, \tag{2.12}$$

where D_r is the rotational diffusivity and r_p is the aspect ratio of the fibres. In the current work the calculation of the extra stress will only be applied to fibres with large aspect ratio ($r_p = 340$) and small rotational diffusivity ($D_r = 0.05$), leading to a simplified expression for the extra stress as (Shaqfeh & Fredrickson 1990; Dinh & Armstrong 1984):

$$\sigma_{ij}^f = \nu Q \Phi (a_{ijkl} - \frac{1}{3}\delta_{ij}a_{kl})\varepsilon_{kl}, \tag{2.13}$$

where the subtraction is performed to remove the isotropic part of the stress which is included into the pressure. The parameter Q for a semidilute suspension is, as given by Batchelor (1971):

$$Q = \frac{r_p^2}{3\ln(\sqrt{2\pi/\Phi})}, \tag{2.14}$$

where a semidilute suspension indicates that there is, on average, between 1-60 fibres inside a cube with sides equal to the length of the fibre. This is deemed to be a more appropriate measure of concentration for fibre suspensions, due to the slenderness of the fibres (Kerekes 2006), taking into account how often the fibres collide with each other.

From the expression given in Eq. 2.13 it is possible to calculate the shear viscosity by setting all components except the transverse elements (ε_{xy} and ε_{yx}) in the strain rate tensor to zero and calculate the resulting shear stress component σ_{xy}, leading to:

$$\mu_{eff} = \mu_l(1 + Q\Phi a_{xyxy}). \tag{2.15}$$

In order to calculate the extra stress (or the effective viscosity) the tensors describing the configuration of the fibres, a_{ijkl} and a_{ij}, need to be obtained. For an exact description of this tensor, the orientation of all fibres in the flow would need to be calculated at each instant in time. However, a simpler way to describe the fibre orientation will be used here. As earlier mentioned, using the equations of Jeffery (1922) the angular motion of an ellipsoidal particle may be calculated assuming creeping flow and inertia-free particles, it will also be assumed that (i) all fibres rotate (perform orbits) in the plane defined by the direction of the mean velocity and the mean velocity gradient, and (ii) that the orientation distribution will be constant in the whole domain at all times. The angular velocity of the fibres can then be described by Eq. 2.4. Since all fibres rotate in a plane, the angle ζ in Fig. 2.1 is set to $\pi/2$. Once the angular velocity has been obtained, the fibre orientation distribution can be calculated through the Smoluchowski equation (Doi & Edwards 1986):

$$\frac{\partial}{\partial\varphi}(\dot{\varphi}\Psi - D_r\frac{\partial\Psi}{\partial\varphi}) = 0, \tag{2.16}$$

where Ψ is the fibre orientation distribution. The elements in the orientation tensor can now be obtained as (Advani & Tucker III 1987):

$$a_{ij} = \int_\zeta\int_\varphi p_i p_j \Psi d\zeta d\varphi \tag{2.17}$$

$$a_{ijkl} = \int_\zeta\int_\varphi p_i p_j p_k p_l \Psi d\zeta d\varphi, \tag{2.18}$$

where p_i are the elements of the orientation vector described by:

$$p_x = \sin\zeta \sin\varphi \tag{2.19}$$

$$p_y = \sin\zeta \cos\varphi \tag{2.20}$$

$$p_z = \cos\zeta. \tag{2.21}$$

It should be evident at this point that this model does not capture the complexity described earlier, where the fibre orientation in a turbulent flow was discussed. This is however not the aim of the present effort, instead the goal is to investigate if this simplified model is enough to qualitatively and quantitatively capture the effect the addition of fibres has on flow stability, as will be discussed in the following chapter.

CHAPTER 3

Disturbances: waves & velocity streaks

How a flow transitions from being steady and laminar at low velocities to oscillatory and eventually turbulent at an increased velocity is of great interest. In material processing one may aim at turbulent flow in order to achieve a homogenous mixing on a macro scale, or desire to keep the flow laminar and as a result preserve the homogeneity at a micro scale. In this chapter modelling of the transition by linear stability analysis (eigenmodes and transient growth) is explained and it is shown how the influence of fibres are taken into account. The theoretical calculations are performed as a complement to experiments, where CNF is used as the added fibres. The effect of fibres on the transition is investigated in three different flow cases, (i) plane channel flow, (ii) curved-rotating channel flow and (iii) the flow in a flow focusing device.

3.1. Linear stability theory applied to fibre suspension flows

3.1.1. *Laminar to turbulent transition*

In an initially laminar flow, disturbances may grow up to a level where non-linear effects becomes important which may result in a turbulent flow. Schmid & Henningson (2001) discuss three different transition scenarios for the parallel boundary layer flow; (i) *Secondary instability of Tollmien-Slichting waves*, where spanwise waves with exponentially growing amplitude starts to oscillate and cause a breakdown to turbulence. (ii) *Streak breakdown* where streamwise streaks experience transient growth and eventually result in breakdown to turbulence. (iii) *Oblique transition* in which a pair of oblique waves interact nonlinearly resulting in the generation of streamwise streaks, that in turn will experience transient growth. In all cases, the transition is initiated by initial disturbances growing due to linear dynamics at some point during the transition scenario.

3.1.2. *Linear Stability theory*

How a particular flow responds to small disturbances is a measure of the stability of the flow. By introducing disturbances into the equations governing a flow, it can be deduced whether these disturbances will decay or grow. Decaying or growing disturbances indicates whether the flow will remain laminar or become turbulent.

The stability of a flow is determined by linearising the governing equations around a mean flow. Starting with the Navier-Stokes equation:

$$\frac{\partial u_i^*}{\partial t^*} + u_j^* \frac{\partial u_i^*}{\partial x_j^*} = -\frac{1}{\rho}\frac{\partial p^*}{\partial x_i^*} + \nu \frac{\partial^2 u_i^*}{\partial x_j^* \partial x_j^*} \tag{3.22}$$

$$\frac{\partial u_i^*}{\partial x_i^*} = 0, \tag{3.23}$$

where ρ is the fluid density and star (*) indicate dimensional values. In a plane channel flow, the velocity vector is given by:

$$\mathbf{u}^* = u^* \mathbf{e_x} + v^* \mathbf{e_y} + w^* \mathbf{e_z}, \tag{3.24}$$

where (x, y, z) are the streamwise, wall normal and spanwise directions. Disturbances are introduced on the parallel mean flow, U_m, and the pressure $\mathcal{P}$ as:

$$\mathbf{U} = (U_m(y) + u'^*, v'^*, w'^*) \tag{3.25}$$

$$p = \mathcal{P} + p'^*. \tag{3.26}$$

If the disturbances are assumed to be of the form:

$$(u', v', w', p') = (X(y), Y(y), Z(y), P(y)) e^{i(\alpha x + \beta z - \omega t)}, \tag{3.27}$$

where α and β are the streamwise and spanwise wavenumbers and ω is the temporal frequency, the decomposition in Eqns. (3.25)-(3.26) can be inserted into Eq. (3.23). After subtraction of the equations describing the mean flow, neglecting the non-linear terms and non-dimensionalisation, the equations describing the stability of the flow in a plane channel are obtained as:

$$\left[i\alpha U_m - \frac{1}{Re}\left(D^2 - \alpha^2 - \beta^2 \right) \right] X + U_m' Y + i\alpha P = i\omega X \tag{3.28}$$

$$\left[i\alpha U_m - \frac{1}{Re}\left(D^2 - \alpha^2 - \beta^2 \right) \right] Y + DP = i\omega Y \tag{3.29}$$

$$\left[i\alpha U_m - \frac{1}{Re}\left(D^2 - \alpha^2 - \beta^2 \right) \right] Z + i\beta P = i\omega Z \tag{3.30}$$

$$i\alpha X + DY + i\beta Z = 0, \tag{3.31}$$

where $D = \partial/\partial y$ and Re is the Reynolds number given by:

$$\mathrm{Re} = \frac{\rho U_m h}{\mu}, \tag{3.32}$$

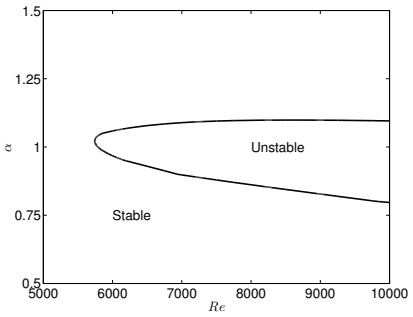

FIGURE 3.1. **Stability diagram.** Neutral stability curve for plane Poiseuille flow, with spanwise wavenumber $\beta = 0$.

where h is the height of the channel and ρ and μ are the density and viscosity of the fluid, respectively. If nothing else is stated, properties of the suspending liquid will be used when calculating the Reynolds number. For a given set of Re and real α and β Eqns. (3.28)-(3.31) constitute an eigenvalueproblem for ω. Here, eigenvalueproblems are solved on a discrete Chebyshev-collocated grid. Solving the eigenvalueproblem results in a complex frequency ω (and its corresponding eigenmodes), where the imaginary part tells if the disturbance will grow ($\omega_i > 0$) or decay ($\omega_i < 0$). By performing this calculation for a wide range of parameters, the neutral stability curve can be mapped out, *i.e.* the curve at which disturbances will start to grow. In Fig. 3.1 the neutral stability curve for plane Poiseuille flow is shown in the α-Re plane. For parameter combinations inside the curve disturbances will grow and the flow is therefore unstable.

3.1.3. *Transient Growth*

It has earlier been discovered, and is today well known, that a linear stability analysis is not always sufficient in order to capture the point at which the transition from laminar to turbulent flow occurs. This is the case in plane Poiseuille flow, where the linear stability analysis predicts a critical Reynolds number $\mathrm{Re}_L = 5772$ (Orszag 1971), while experiments have shown that the transition occurs at $\mathrm{Re}_T \approx 1000$. However, subcritical growth, *i.e.* initial growth even when all eigenmodes decay, is possible if the eigenmodes are non-orthogonal. From the illustration in Fig. 3.2 it is evident, that even if two modes decay, an initial amplification of the total disturbance may occur if the rate at which they decay is different. By using the eigenmodes from the previously solved eigenvalue problem, the amplification in time may be calculated as (Trefethen *et al.* 1993; Åkervik *et al.* 2008):

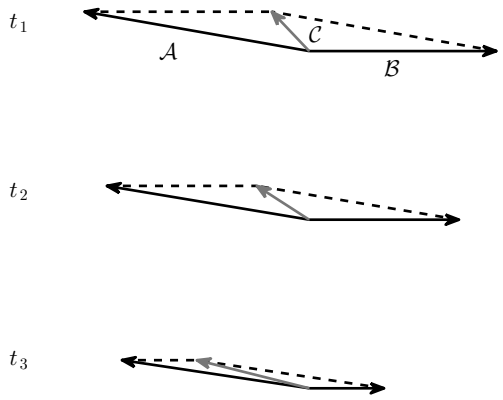

FIGURE 3.2. **Non-orthogonality** As the non-orthogonal eigenmodes ($\mathcal{A}$ and $\mathcal{B}$) decay in time, an initial amplification of the total disturbance ($\mathcal{C}$) is possible at finite times.

$$G(t) = \max\left(\frac{||\mathbf{u}'(t)||_E^2}{||\mathbf{u}_0'(t)||_E^2}\right), \tag{3.33}$$

where $\mathbf{u}_0(t)$ is the initial condition and $\mathbf{u}(t)$ is the disturbances at time t, obtained as a sum of eigenmodes. In practice, this calculation is done by obtaining the largest singular value of the term $Fe^{\Lambda t}F^{-1}$, corresponding to the largest growth at the given time, t. Λ is a diagonal matrix containing the eigenvalues ω and F is the Cholesky factorisation of the energy matrix $M = K^T\Delta K$, where K is a matrix containing the eigenfunctions and Δ is the distance between the nodes in the grid used in the calculations.

3.1.4. *Stability of fibre suspension flows*

Investigations into the effects of fibres on the linear stability have earlier been performed for different flows, Bark & Tinoco (1978); Nsom (1996); Azaiez (2000); Gupta *et al.* (2002); Zhenjiang *et al.* (2004). In all of the mentioned studies, the addition of fibres was found to stabilise the flow. However, the wavenumber of the critical disturbance was in a plane channel seen to increase with increased fibre concentration (Zhenjiang *et al.* 2004), while in a curved channel it was found to be independent of fibre concentration (Nsom 1996). In table 3.1 studies where the effect of fibres on transition (by linear stability or experiments) has been of main interest are summarised. Regarding the transient growth of particle suspensions, there is little information available in the literature. Klinkenberg *et al.* (2011) investigated the effect of spherical, inertial, point-particles on the modal- and non-modal-growth in a channel flow.

For the modal stability the presence of particles where found to stabilise the flow while for the non-modal growth an increase in energy growth was seen with increasing mass fraction. The increase in energy growth was found to scale with $(1+f)^2$, with f as the added mass fraction.

As explained in chapter 2, the addition of fibres is modelled by an additional stress. Applying this stress to the Navier-Stokes equation and performing the same steps as earlier described, the linear stability equations for the fibre suspension flow in a plane channel are (as given in Paper 5):

$$\mathcal{L}X + U'Y + i\alpha P - \frac{1}{Re}Q\Phi\Big\{A_xX + A_yY + A_zZ\Big\} = i\omega X \tag{3.34}$$

$$\mathcal{L}Y + DP - \frac{1}{Re}Q\Phi\Big\{B_xX + B_yY + B_zZ\Big\} = i\omega Y \tag{3.35}$$

$$\mathcal{L}Z + i\beta P - \frac{1}{Re}Q\Phi\Big\{C_xX + C_yY + C_zZ\Big\} = i\omega Z \tag{3.36}$$

$$i\alpha X + DY + i\beta Z = 0, \tag{3.37}$$

where:

$$\mathcal{L} = \left[i\alpha U - \frac{1}{Re}(D^2 - \beta^2 - \alpha^2)\right]$$

$$\begin{aligned} A_{x_i} = &-\alpha^2(a_{xxxx_i} - \frac{1}{3}a_{xx_i}) + i\alpha D(a_{xxyx_i} - \frac{1}{3}a_{y_i}) - \alpha\beta(a_{xxzx_i} - \frac{1}{3}a_{zx_i}) + \\ &i\alpha D a_{xxyx_i} + D^2 a_{xyyx_i} + i\beta D a_{xyzx_i} - \alpha\beta a_{xxzx_i} + i\beta D a_{xyzx_i} - \beta^2 a_{xzzx_i} \end{aligned}$$

$$\begin{aligned} B_{x_i} = &-\alpha^2 a_{xxyx_i} + i\alpha D a_{xyyx_i} - \alpha\beta a_{xyzx_i} + i\alpha D(a_{xyyx_i} - \frac{1}{3}a_{xx_i}) + \\ &D^2(a_{yyyx_i} - \frac{1}{3}a_{yx_i}) + i\beta D(a_{yyzx_i} - \frac{1}{3}a_{zx_i}) - \alpha\beta a_{xyzx_i} + \\ &i\beta D a_{yyzx_i} - \beta^2 a_{yzzx_i} \end{aligned}$$

$$\begin{aligned} C_{x_i} = &-\alpha^2 a_{xxzx_i} + i\alpha D a_{xyzx_i} - \alpha\beta a_{xzzx_i} + i\alpha D a_{xyzx_i} + D^2 a_{yyzx_i} + \\ &i\beta D a_{yzzx_i} - \alpha\beta(a_{xzzx_i} - \frac{1}{3}a_{xx_i}) + i\beta D(a_{yzzx_i} - \frac{1}{3}a_{yx_i}) - \\ &\beta^2(a_{zzzx_i} - \frac{1}{3}a_{zx_i}). \end{aligned}$$

Author(s) (year)	**Flow Case**	**Method**[3]	**Main Conclusions**
Radin *et al.* (1975)	Pipe flow	EXP	Delayed and extended transitional region.
Bark & Tinoco (1978)	Poisuielle	LS	Fibres act stabilising at small β, stabilisation scales with Φr_p^2.
Pilipenko *et al.* (1981)	Taylor	EXP	Larger influence on viscosity compared to Taylor number.
Nsom (1996)	Dean	LS	No effect on critical wavenumber.
Azaiez (2000)	Mixing layer	LS	The parameters[4] H and C_l govern the instability, stabilisation due to hydrodynamic interaction among fibres.
Gupta *et al.* (2002)	Taylor-Couette	LS	Choice of closure model has minor effects, enhanced stabilisation for increased C_l, Φ, r_p.
Zhenjiang *et al.* (2004)	Poisuielle	LS	Increased Re_{cr} and α_{cr} with increased parameters[4] H and C_l.

TABLE 3.1. Earlier studies of the effect of fibres on transition in various configurations.

[3]LS: Linear Stability, EXP: Experiment
[4]$H = Q\Phi/Re$

This eigenvalueproblem may now be treated in the same way as previously described and the transient growth is also obtained in the same manner. This type of analysis is performed in Papers 3, 4 & 5 for two different flow cases, discussed in the following sections. In all papers, the analysis is performed as a complement to experiments with CNF.

3.2. Effect of fibres on plane channel flow

The influence of fibres on the flow in a plane channel was investigated by Kvick *et al.* (2014*d*) (Paper 5). The experimental setup is presented in Appendix A.2. Pressure drop measurements and flow visualisation were used to quantify the effect of (CNF) at various concentrations. In Fig. 3.3 images of the visualised structures in the flow are shown for four different Reynolds number. It can easily be seen in the images that parts of the flow is laminar and parts are turbulent, *i.e.* the flow is intermittent. This type of behaviour is well known for the laminar/turbulent transition in both channels and pipes (Seki & Matsubara 2012; Avila & Hof 2013). As the Reynolds number is increased, the amount of turbulence in the images increases, *i.e.* disturbances from the inlet has a higher probability of sustaining the turbulence. When CNF is added, similar amount of activity in the images can be seen at much higher Reynolds number, as depicted in Fig. 3.4. How much larger the Reynolds number need to be in order to sustain turbulence will in more detail be discussed using pressure drop measurements.

In Fig. 3.5 the friction coefficient, $C_f = \tau_w/(\frac{1}{2}\rho_w U^2)$, obtained from pressure drop measurements, is shown as a function of Reynolds number for a number of concentrations. The solid lines in Fig. 3.5 are empirical fits from Patel & Head (1969). In the figure, a clear delay can be seen on the transition, *i.e.* the point at which the friction coefficient deviates from the laminar line. It can also be seen that the minimum value of the friction coefficient is decreasing with increasing mass fraction, up to $c_m = 600$ ppm, where a maximum drag reduction of 30% is reached in the transitional region. In Paper 5, the effect of ageing of the suspensions is also demonstrated, where ageing before or after the dilution process give different effect on the transition. No definitive conclusions are drawn regarding the ageing, it should however always be considered when results using biodegradable material are presented.

Since the transition from laminar to turbulent flow in a plane channel cannot be described by the linear stability analysis alone, the transient growth of disturbances for different Reynolds numbers and fibre concentrations were used to investigate the effect of the addition of fibres to the flow. The maximum possible amplification obtained for each Reynolds number is shown in Fig. 3.6a. As the concentration of fibres is increased, the growth of the disturbances is attenuated in a well-ordered manner. The rate at which this attenuation occurs is in Fig. 3.6b scaled with an empirically obtained formula $m\mathrm{Re}^k$, where m and k are given by:

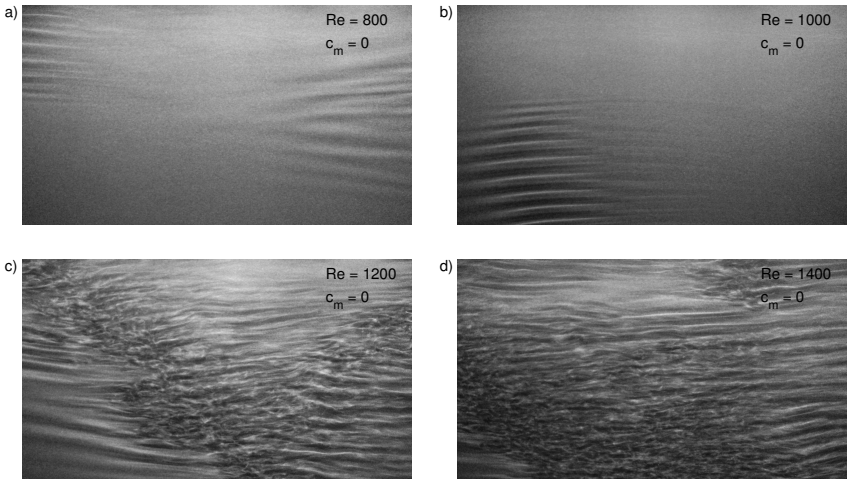

FIGURE 3.3. **Visualisation of flow in a plane channel, $\mathbf{c_m = 0}$.** Examples of images of the flow captured during the experiments in the plane channel for pure water with increasing Reynolds number, Re= 800, 1000, 1200, 1400 from a) to d), the flow is from left to right.

$$m = b_{m1}\left(\frac{r_p^2}{Q}\right)^2 + b_{m2}\left(\frac{r_p^2}{Q}\right) + b_{m3} \tag{3.38}$$

$$k = b_{k1}\left(\frac{r_p^2}{Q}\right)^2 + b_{k2}\left(\frac{r_p^2}{Q}\right) + b_{k3}, \tag{3.39}$$

with:

$$(b_{m1}, b_{m2}, b_{m3}) = (0.002289, -0.05606, 1.205) \tag{3.40}$$

$$(b_{k1}, b_{k2}, b_{k3}) = (-0.06506, 2.068, -14.77). \tag{3.41}$$

This scaling is performed to illustrate that a scaling is possible. More parameter variations are necessary in order to find out what the actual scaling is.

The wavenumber at which the maximum growth occurs is shown in Fig. 3.7. With pure fluid, $\Phi = 0$, the streamwise wavenumber, α, is zero and as fibres are added it increases. The spanwise wavenumber, β, is for all concentrations and Reynolds number approximately $\beta \sim 2$. The experimental and theoretical results will be further analysed and compared in section 3.4.

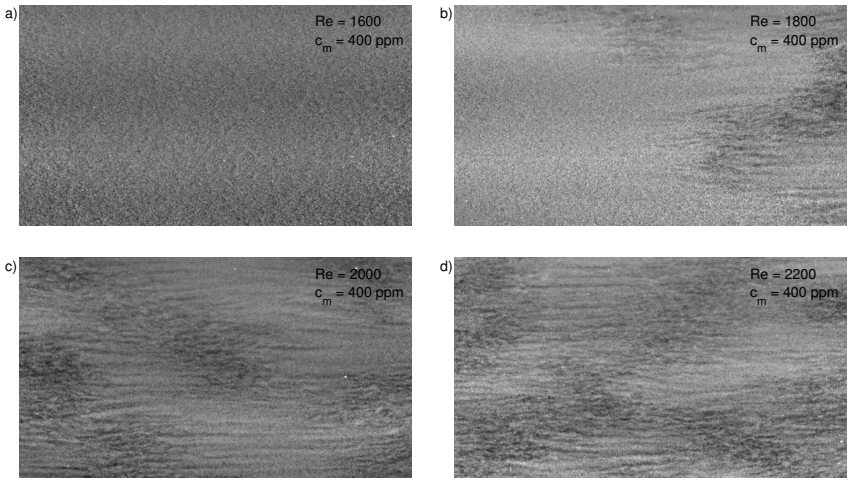

FIGURE 3.4. **Visualisation of flow in a plane channel, $\mathbf{c_m = 400}$ ppm.** Examples of images of the flow captured during the experiments in the plane channel for a CNF suspension with a mass fraction of $c_m = 400$ ppm, with increasing Reynolds number, Re$= 1600, 1800, 2000, 2200$ from a) to d), the flow is from left to right.

3.3. Effect of fibres on curvature and rotational instabilities

In Kvick *et al.* (2013*b*) and Kvick *et al.* (2013*a*) (Papers 3 & 4) the influence of fibres on the transition in a curved channel with rotation is studied, the setup is explained in detail in Appendix A.3. Unlike the previously discussed Poiseuille flow, the transition in this type of channel is well defined. The transition is governed by the centrifugal force arising from the curvature of the channel and can either be stabilised or destabilised by the Coriolis force that occurs as an effect of the rotation. The direction and strength of the Coriolis force are decided by the direction and speed of the rotation. At a certain strength of the sum of the centrifugal and Coriolis forces, the viscous forces resisting disturbance growth will be overcome, resulting in the generation of streamwise vortices. This is illustrated in Fig. 3.8, where images from experiments with a constant Reynolds number and increasing rotation number is shown. With a negative rotation number, the Coriolis force will counteract the centrifugal force and as soon as the rotation number changes sign, the two forces will have the same direction and an enhancement of the transition is seen with increasing rotation number. A more detailed explanation on the stability of pure fluid flow in a curved, rotating, channel is given by Matsson & Alfredsson (1990) and Matsson & Alfredsson (1992) .

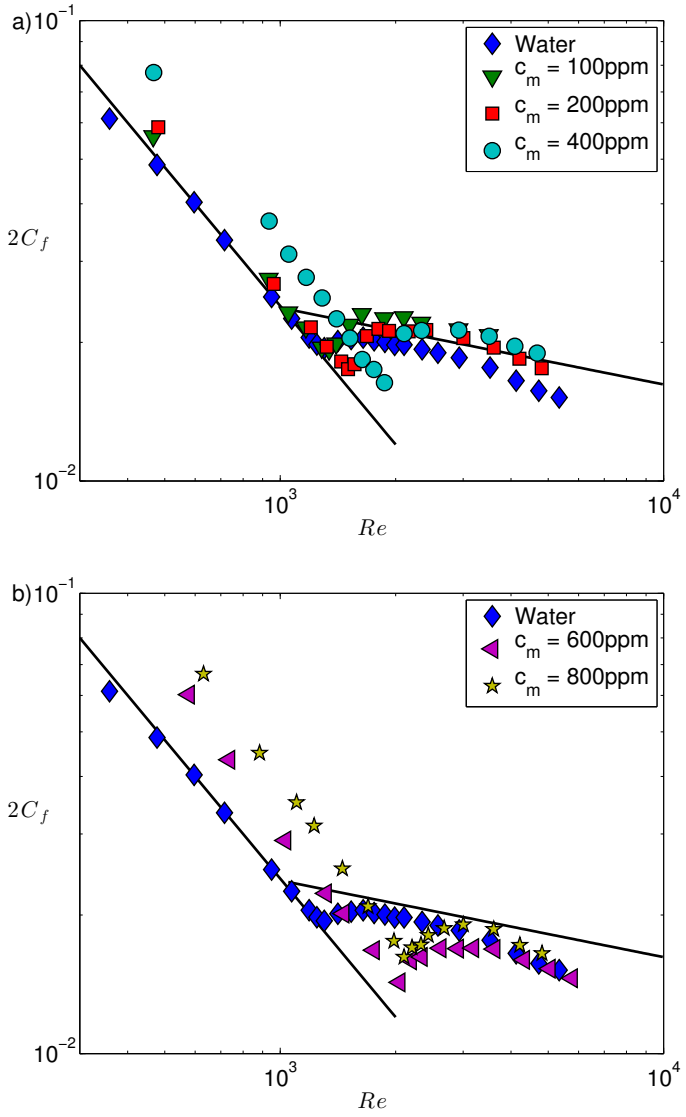

FIGURE 3.5. **Friction coefficient in plane channel.** Friction coefficients versus Reynolds number for a number of different concentrations of CNF. The solid lines are for low Reynolds numbers the laminar ($C_f = 12/Re$) and for large Reynolds numbers the turbulent ($C_f = 0.0376Re^{-1/6}$) friction coefficient estimations, as given by Patel & Head (1969).

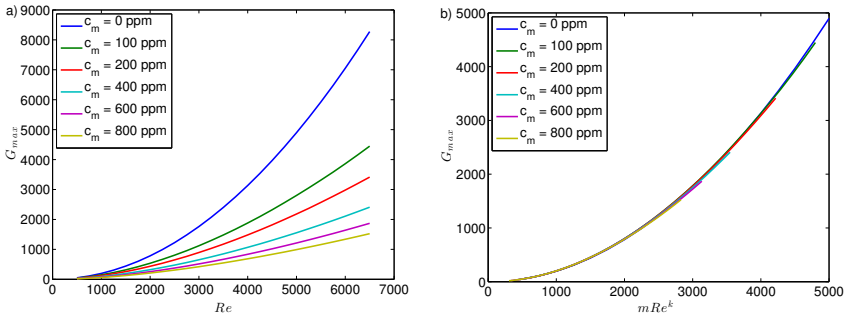

FIGURE 3.6. **Transient growth.** a) Maximum transient growth for different fibre-concentrations, in b) the Reynolds number has been scaled by $m\mathrm{Re}^k$, where m and k are given in Eqns. (3.38) - (3.39).

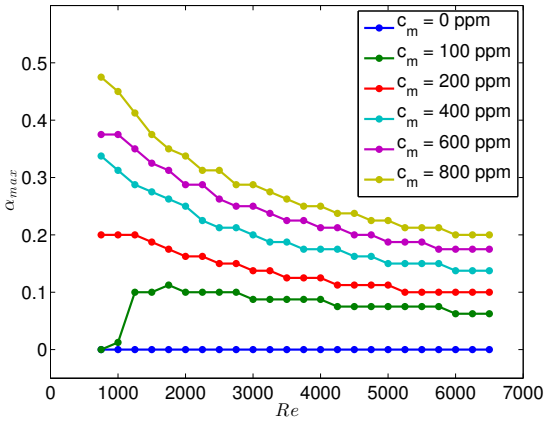

FIGURE 3.7. **Wavenumber at maximum growth.** Streamwise wavenumber at which the maximum transient growth occurs in a plane channel for different concentrations of fibres.

The flow visualisations and the linear stability analysis performed in Paper 3 allows for a region of laminar/stable flow to be established. This is carried out for water as well as a CNF suspension. In Fig. 3.9 contours of the laminar regions (solid lines) as well as the neutral stability curves (dashed lines) are shown for a few different volume fractions. The stability diagram is given in the Reynolds/rotation-number plane, given by:

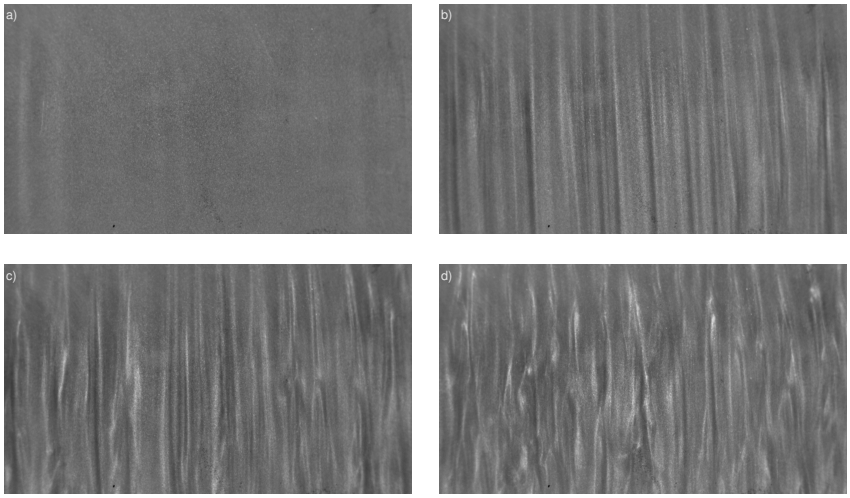

FIGURE 3.8. **Flow visualisations in curved channel.** Images captured during experiments in the rotating curved channel flow for pure water with Re=595 and increasing Rotational number, Ro= $-0.024, 0.0058, 0.039, 0.076$ from a) to d), flow is from top to bottom.

$$\mathrm{Re} = \frac{U_b d}{\nu} \tag{3.42}$$

$$\mathrm{Ro} = \frac{\Omega d}{U_b}, \tag{3.43}$$

where Ω is the rotational velocity, positive in the direction of the flow, d is the channel width, U_b is the bulk velocity and ν is the viscosity of the suspending liquid. A qualitative agreement can be seen between the curves, with a large difference at the peak where the maximum possible Reynolds number is reached. The reason for this difference could be the sensitivity of the flow to changes in rotational velocity in that region, where a small disturbance on the rotational speed can trigger the transition. However, of more interest is the fact that as the concentration of fibres is increased, the laminar region in the experiments and the stable region in the calculations grow. How large this growth is and how it compares with the increase in viscosity will be discussed next.

3.4. Scalings of $\mathbf{Re}_{susp}$ with μ_{susp}

The influence of fibres on transition in the plane channel (PF) and curved, rotating, channel (CC) are summarised in table 3.2. In the table, the condition

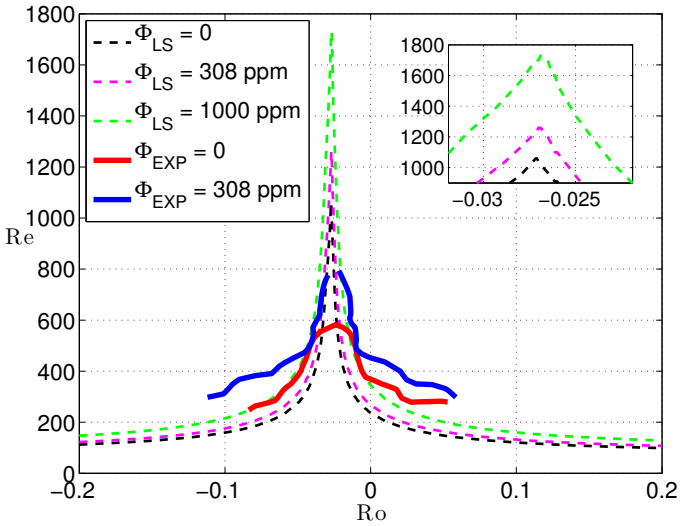

FIGURE 3.9. **Stablity diagram for curved, rotating, channel.** Neutral stability curves from the linear stability analysis (dashed lines) and the laminar region obtained from the experiments (solid lines) in the curved, rotating channel for different volume fractions Φ.

for each critical Reynolds number (Re_{Cr}) and the definitions of the suspension Reynolds numbers ($\mathrm{Re}_{susp} = \mathrm{Re}_{Cr}/\mu_{susp}$) are given. The viscosities used in the scalings have either been obtained from the increase in pressure drop in the laminar region (μ^{PF}_{EXP}), rotational viscometer measurements (μ^{CC}_{EXP}) or from the rheological model in Eq. 2.15 (μ^{PF}_{LS} and μ^{CC}_{LS}). All viscosities have been normalised with the viscosity of the suspending liquid.

The suspension Reynolds numbers are shown as a function of the concentration of fibres in Fig. 3.10. For the curved channel flow, the linear stability analysis qualitatively predicts the scaling for the Reynolds number; with a small decrease in suspension Reynolds number as the concentration increase. For the plane Poiseuille flow the effect is opposite, an increase can be seen in the suspension Reynolds number as the concentration increase. Even though the effects are opposite in the two experiments, the linear stability analysis/transient growth analysis, qualitatively captures the effect.

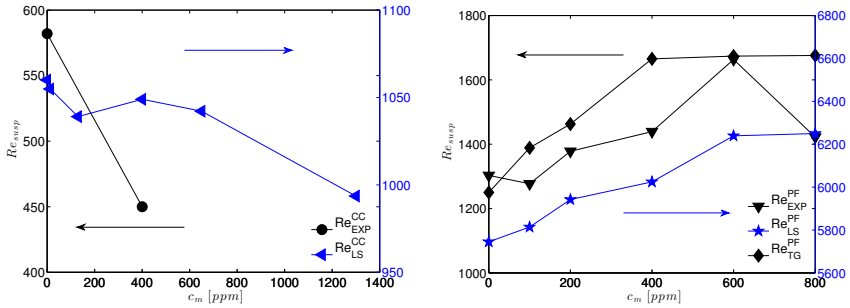

FIGURE 3.10. **Scaling of Reynolds numbers.** Critical Reynolds number scaled with the viscosity as shown in table 3.2. In a) data from the investigations in the curved-rotating setup is shown and in b) the results from the plane channel are summarised.

Flow Case	**Exp.**	**LS**	**TG**	**Condition**	μ	Re_{susp}
Poiseuille	X	-	-	Rapid change in pressure drop	μ_{EXP}^{PF}	$\mathrm{Re}_{EXP}^{PF} = \frac{\mathrm{Re}_{Cr}^{PF}}{\mu_{EXP}^{PF}}$
Poiseuille	-	X	-	Min Re with $\omega_i > 0$	μ_{LS}^{PF}	$\mathrm{Re}_{LS}^{PF} = \frac{\mathrm{Re}_{Cr}^{PF}}{\mu_{LS}^{PF}}$
Poiseuille	-	-	X	Re with $G_{max} = 700$	μ_{LS}^{PF}	$\mathrm{Re}_{TG}^{PF} = \frac{\mathrm{Re}_{G700}^{PF}}{\mu_{LS}^{PF}}$
Curved	X	-	-	Maximum laminar Re	μ_{EXP}^{CC}	$\mathrm{Re}_{EXP}^{CC} = \frac{\mathrm{Re}_{Cr}^{CC}}{\mu_{EXP}^{CC}}$
Curved	-	X	-	Max Re with $\omega_i < 0$	μ_{LS}^{CC}	$\mathrm{Re}_{LS}^{CC} = \frac{\mathrm{Re}_{Cr}^{CC}}{\mu_{LS}^{CC}}$

TABLE 3.2. Definition of suspension Reynolds numbers and the condition for critical Reynolds numbers for the experiments, linear stability analysis and transient growth analysis in the two flow cases. All viscosities are non-dimensionalised with the viscosity for pure fluid.

3.5. Flow stability in a microchannel

Up until this point the cases investigated have been generic, aiming at direct comparison between experiments and theory in order to provide insights in the design and modelling of large scale processes. In this section we will focus on the factors that governs the stability of the flow in a millimeter sized assembly unit. A similar unit has been used in the assembly of filaments from CNF, resulting in a strong continuous thread made from cellulose with a controlled orientation of the fibrils (Håkansson *et al.* 2014). The unit in question is a flow focusing device, described in Appendix A.4. Lashgari *et al.* (2014) studied the global stability in such a device numerically, showing that the point of transition was governed by the Reynolds number of the side flow alone. Using a high viscosity liquid in the core flow, Kvick *et al.* (2014*b*) (Paper 6) performed experiments mapping out fluctuations of the core flow in the plane spanned by the Reynolds numbers for the two flows, defined by:

$$\mathrm{Re}_s = \frac{U_{s,max}\frac{h}{2}}{\nu_s} \tag{3.44}$$

$$\mathrm{Re}_c = \frac{U_{c,max}\frac{h}{2}}{\nu_s} \tag{3.45}$$

where ν_s is the viscosity of the fluid in the sheath, $U_{s,max}$ and $U_{c,max}$ are the maximum velocity in the core and side channels respectively and h is the height of the channel.

Visualisations of the flow is shown in Fig. 3.11 where, starting from a laminar flow, the two Reynolds numbers are varied independently, clearly showing how the increase of the Reynolds number of the side flow causes the flow to oscillate while an increase in the core Reynolds number has only minor effects. This is in qualitative agreement with the results from Lashgari *et al.* (2014), even though the Reynolds numbers differs by a factor 5. The temporal *rms* of the position of the interface between the core and side flows is used as a measure of the stability of the flow, y_{rms} is low when the core flow is not moving and assumes a high value when it oscillates. In Fig. 3.12a the results from experiments with a $c_m = 0.33\%$ CNF solution in the core flow are shown as well data form experiments where the viscosity of the fluid in the core has been reduced from the reference of $\mu = 40$ mPas to $\mu = 20$ mPas.

Both in the work by Lashgari *et al.* (2014) and in Paper 6 different means of control are applied in order to stabilise/destabilise the flow. Lashgari *et al.* (2014) successfully stabilised the flow by suction at the walls in the beginning of the outlet, motivating this by the presence of a recirculation bubble which was reduced by the suction. Similarly, in the present work, an attempt to reduce the recirculation bubble by changing the downstream sharp corners to ones with a 0.1 mm radius were made, this did not however effect the flow in the expected

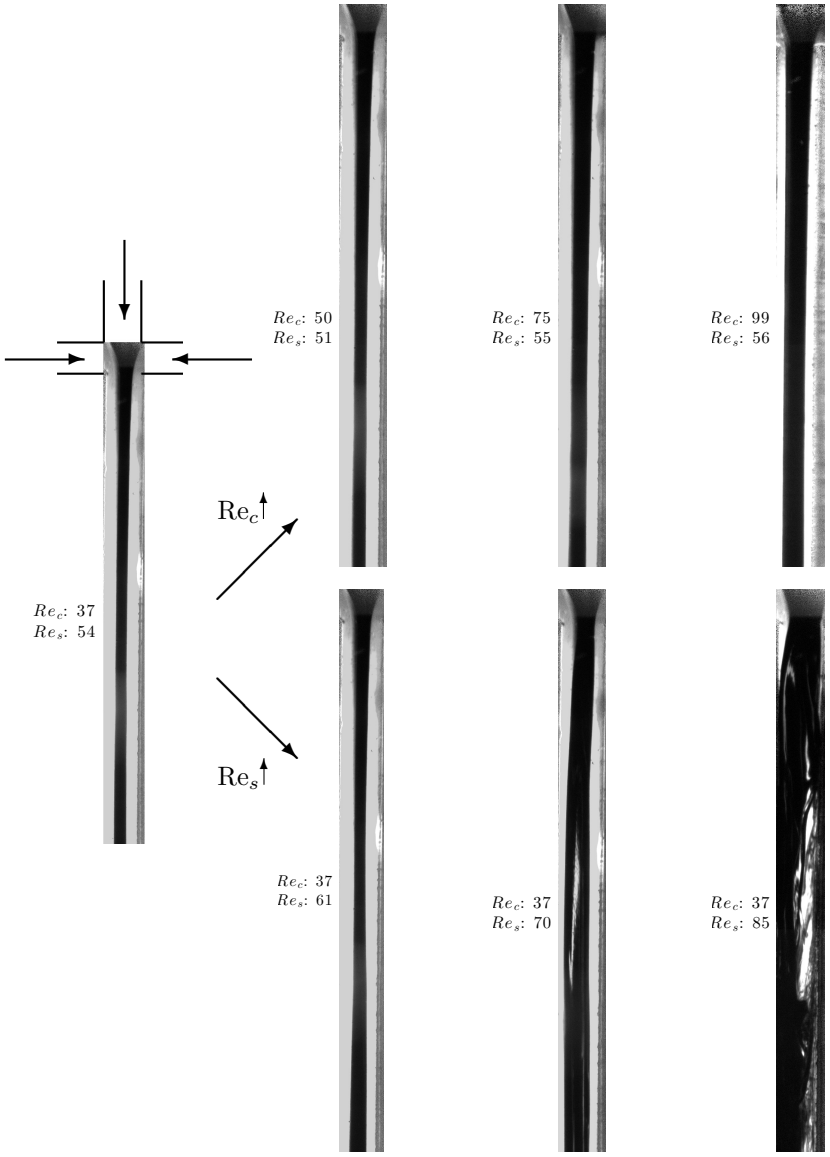

FIGURE 3.11. **Visualisations of the core flow in flow focusing.** Behaviour of the flow in a flow focusing device (case A in table 3.3) with increasing Reynolds numbers, the fluid in the core channel has been dyed black. In the top and bottom rows, the core (Re_c) and sheath (Re_s) Reynolds numbers are increased respectively from the reference case shown (left).

Case	Channel	Core fluid	Core fluid viscosity
A	α	Water-Glycerol	40 mPas
B	α	Water-Glycerol	20 mPas
C	α	CNF	see Fig 3 in Paper 6
D	β	Water-Glycerol	40 mPas

TABLE 3.3. Summary of the different setups used in Paper 6. In channel α all corners have sharp corners while in channel β the downstream corners has a radius of $Ra = 0.1$ mm.

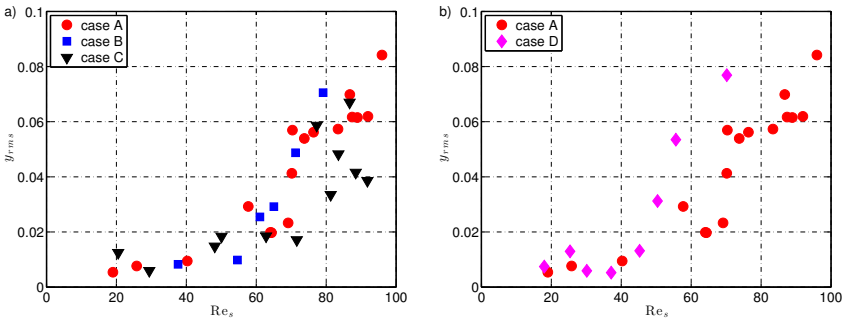

FIGURE 3.12. **Quantified stability of core flow.** Temporal rms (y_{rms}) of the interface between the fluids as a function of sheath Reynolds number for a) experiments with different core fluid viscosity and b) right and rounded downstream corners. The different experiments are summarised in table 3.3.

way. If anything, the attempt to stabilise the flow in this way resulted in a destabilisation, as can be seen from the temporal *rms* of the interface position between the core and sheath flows in Fig. 3.12b.

If the recirculation bubble is responsible for the transition in the channel, the point at which the transition occurs should have moved to a larger value of the sheath Reynolds number. It is unclear whether the absence of stabilisation is due to the transition being governed by some other physical mechanics or if the attempts to influence the recirculation bubble failed. At larger sheath Reynolds numbers, the oscillations were smaller than in the reference case. Indicating that the recirculation bubble was prevented from growing, provided that a bubble exist and is responsible for the onset of oscillations.

The experiments with CNF are connected to the production of cellulose threads, as described in Håkansson *et al.* (2014), and investigates whether it is sufficient to perform studies of the flow in the channel with a substitute for the CNF. Since no apparent effect on the onset of oscillations can be seen when

changing fluids, the use of a high viscosity liquid in place of the CNF suspension is deemed suitable to map out operational windows in a device such as the one used here.

CHAPTER 4

Alignment, assembly & consolidation of nanofibrils

The understanding of fibre suspension flow is not only important in order to find an optimal operational window; the flow may also be used to effectively control the individual fibres. In this chapter, it is described how a flow focusing unit was used by Kvick *et al.* (2014*c*) (Paper 6) in order to produce a continuous sheet/film from CNF. This is an extension of the method earlier developed by Håkansson *et al.* (2014) used to manufacture continuous, strong, filaments from CNF. Håkansson *et al.* (2014) were able to utilise flow focusing in such a way that control of the orientation of the fibrils in the flow filament was achieved.

4.1. Alignment of nanofibrils by extensional flow

In a flow focusing device, such as the one depicted in Fig. 4.1, the intersections of the flows will cause an acceleration of the core flow. This setup is very similar to the flow focusing device described in the previous chapter, the difference being that the device has two serial intersections. Introducing CNF in the core flow will subject the fibrils to an extensional flow, resulting in an alignment of the fibrils in the streamwise direction. After reaching a peak value, the alignment of the fibrils will decay due to rotational Brownian diffusion. Preventing

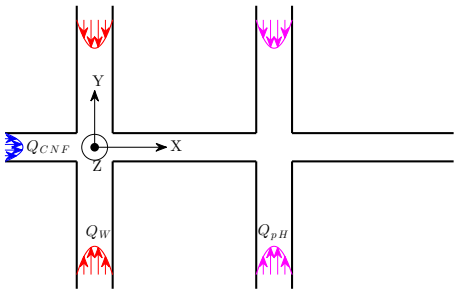

FIGURE 4.1. **Flow focusing coordinate system.** Schematic drawing of a flow focusing device with two serial intersections. The first intersection creates a lubrication layer to avoid clogging and the second administers a low pH solution causing gelation of the CNF in the core.

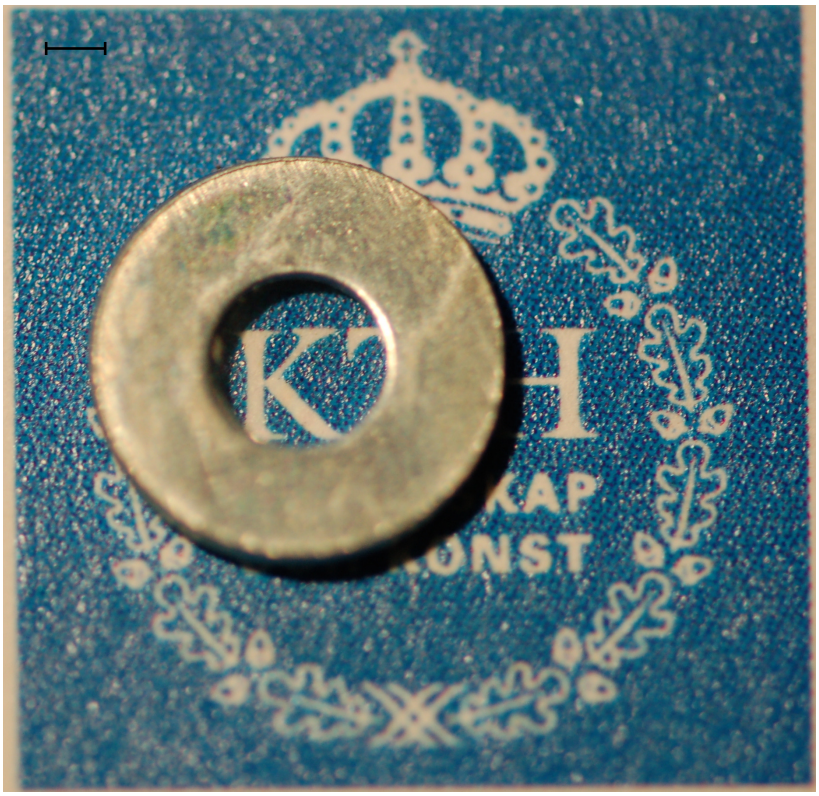

FIGURE 4.2. **CNF film.** Picture of the resulting dried film mounted over the hole on a washer, the scale bar is 1 mm.

this dealignment is essential when seeking a structure with strong alignment. It will now be described how this is achieved.

4.2. Gelation of CNF

In the manufacturing process of CNF, *i.e.* liberation of the nano-fibrils, a surface charge is introduced on the fibril surfaces by carboxymethylation (Wågberg *et al.* 1987). This charge will repel the fibrils from each other and prevent them from re-forming agglomerates after liberation. In order for a desired configuration to be kept, the surface charges can be screened by increasing the amount of ions in the fluid surrounding the fibrils, allowing the fibrils to come in contact with each other. When the fibrils are sufficiently close together, van der Waals interactions will cause them to attract each other, creating a gel, effectively locking the configuration (Fall *et al.* 2011).

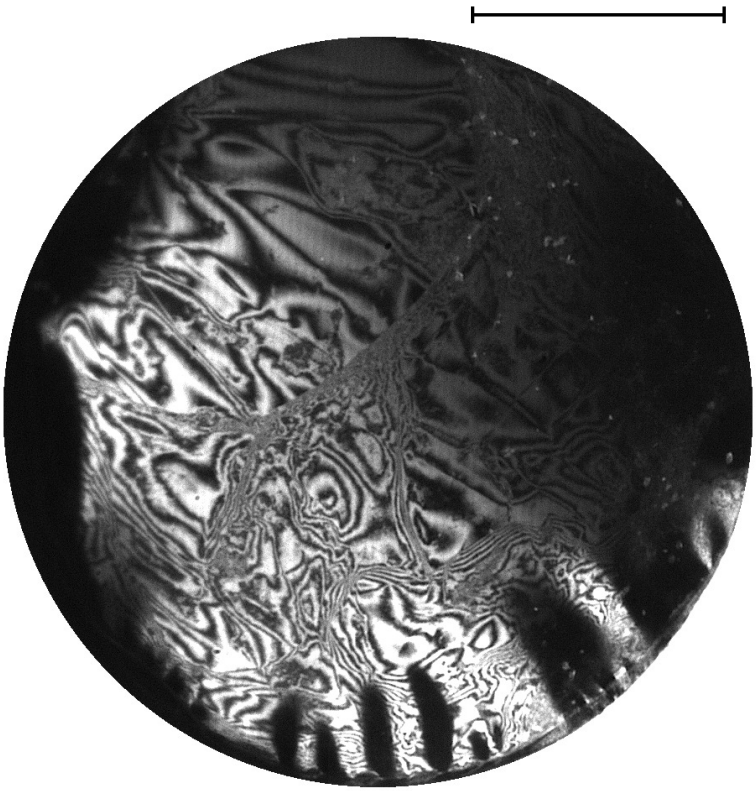

FIGURE 4.3. **CNF film interference pattern** Picture of the resulting dried film under monochromatic light. The scale bar is 1 mm.

4.3. Producing a continuous CNF film

The process of using flow focusing as a tool to produce a film from CNF will now be explained. The device used has a cross section as the one illustrated in Fig. 4.1. Each individual channel has a heigh of 1 mm and a depth of 10 mm. The incoming flow rates are $(Q_{CNF}, Q_W, Q_{pH}) = (0.2, 0.1, 0.8)$ l/h, corresponding to Reynolds numbers of $(\mathrm{Re}_{CNF}, \mathrm{Re}_W, \mathrm{Re}_{pH}) = (4, 2, 17)$, based on the viscosity of water.

The first of the two intersections provides a lubrication layer (water) to avoid clogging of the device, while the second accelerates the core flow and administers a low pH solution, resulting in a coagulation of the CNF dispersion. The gelation of the dispersion hinders the de-alignment due to rotational Brownian diffusion, locking the structure in its current configuration. The resulting

gel sheet is thereafter ejected into a low pH solution, extracted onto a metal frame and allowed to dry in ambient conditions. An example of the resulting film, made from pure CNF, is shown in Fig. 4.2. In Fig. 4.3 the film has been placed under monochromatic light. The difference in the interference pattern indicates a non-uniform thickness of the film. This is at the moment believed to be a result of the drying conditions.

It should be noted that the Reynolds number of the second sheath $\mathrm{Re}_{pH} = 17$ is not far from the critical Reynolds number where the core start to oscillate ($\mathrm{Re}_s \approx 50$), as discussed in the previous chapter. This rather large flow rate, is needed in order to ensure a 2-dimensional flow. If the flow rate is too low, the core flow will migrate to the one of the corners in the channel. This also indicated that the operational window, where the production of film in this device is possible, is not large. Especially when considering the need to balance the timescales for; (i) alignment, (ii) ion diffusion to the core, (iii) dealignment due to Brownian diffusion and (iv) convection of the thread out of the device, as reported in Paper 7 and Håkansson *et al.* (2014).

CHAPTER 5

Conclusions & Outlook

In this chapter the main conclusions are summarised and areas of interest for future work are discussed.

5.1. Fluid flow as a tool in a manufacturing process

In Paper 7 it is proved that it is possible to use a flow focusing device in order to manufacture film from cellulose nanofibrils (CNF). The film is transparent and estimated to have a thickness of ~ 1 μm. This study was performed solely as a proof of concept, and no optimisation was performed in terms of flow or drying conditions. In order for the process to become a reliable option, parameter studies and measurements of the material properties of the film are needed. It is also of importance to understand how an increasing depth of the channels effects the orientation of the fibrils in both planes. The orientation in the flow-gradient plane can be obtained either by X-ray diffraction measurements during a production phase and/or by 3-dimensional simulations. The 3-dimensional simulations are necessary in order to check how the fibrils orient themselves in the plane of the film during the process, this orientation is in the current setup not possible to measure and numerical studies are essential.

5.2. Fibre orientation/distribution for model validation

The orientation and spatial distribution of fibres in a flow down an inclined plate are in Paper 1 investigated for varying friction Reynolds number, fibre aspect ratio and concentration. It is found that the main parameter governing the orientation distributions is the fibre aspect ratio, with only minor effects from other parameters. The shorter fibres ($r_p = 7$) are found to have a preferential alignment in the spanwise direction, while the longer fibres ($r_p = 28$) tend to adapt an orientation close to the flow direction. Moreover, in the range of parameters investigated, the fibres agglomerated into streamwise streaks. In Paper 2 a method was developed in order to quantify this *streakiness*, resulting in a maximum agglomeration at $\mathrm{Re}_\tau = 110$. The streaks were also found to be slightly wider than the value normally associated with near wall low velocity streaks in turbulent boundary layers. It is found that the concentration needs to be handled with great care in order to obtain a valid measure of the streakiness, which can be compared to other experiments.

The data collected in can be used as a qualitative validation when modelling fibres in turbulent wall bounded flow. It should be realised that in order to understand the motion of fibres in a flow, single fibre experiments and simulations could be of interest and provide insight in to the behaviour of fibre-wall interactions. It would however be hard to achieve the statistical convergence obtained here and a combination of single fibre and fibre suspension experiments and simulations are necessary to provide the full picture. With more detailed models and knowledge of the movement of fibres in flows, it can be understood when and how simplified models can be used. On order to get more detailed data, simultaneous fluid and fibre velocity measurements could be obtained using PIV. This would provide both the statistics and details about individual fibre motions needed for model development.

5.3. Continuum models in the design of material processes

The effect of fibrils on the laminar-turbulent transition is investigated in two different setups. In Papers 3, 4 & 5 experiments are combined with linear stability analyses. The setups used are a curved, rotating channel and a plane channel. In all experiments and calculations, the addition of CNF delays the laminar turbulent transition. Pressure drop measurements carried out in the plane channel results in a maximum drag reduction of 30% in the extended laminar region. However, this drag reduction occurs only in a small region of Reynolds numbers. It is found that the simplified, continuous, rheological model used to model the fibres in the linear stability analyses captures the qualitative behaviour of the transition observed in the experiments. By scaling the critical Reynolds numbers with the measured viscosity, two distinct differences between the two setups are observed. This difference is seen in both the experiments and the linear stability analyses. In the curved channel flow the scaled Reynolds number decreases, while it for the plane channel increases. An analysis of the transient growth of disturbances in the plane channel flow reveals, for the maximum transient growth, an increasing streamwise wavenumber with increasing concentration, starting from zero without fibres. The qualitative similarity between the results from the experiments and the models indicates that this simplified calculations can be used as a first step in the design process.

The fibrils used in the experiments have a range of lengths and diameters, which is not quantified here. In order to make a more quantitative comparison between experiments and linear stability analyses of fibre suspension flows, experiments with well-controlled fibre aspect ratio are necessary. One would also benefit greatly by reducing the density difference between the fibres and the suspending fluid, thereby preventing sedimentation and greatly simplifying experiments.

As mentioned earlier, the rheological model used in this work is chosen to be simple. The first step to increase its complexity, and hopefully also its accuracy, would be to implement a closure approximation for the fibre orientation, and

investigate how disturbances on the fibre orientation influence the stability. Furthermore, to understand the reason for the different trends in the two setups, an estimation of the order of the terms in the linearised equations would provide valuable information on the physical process responsible for the different trends.

5.4. Model fluids and flow control

In Paper 6 the flow stability in a flow focusing device is examined. By varying the flow rates in the core and side channels it is found that the main parameter governing the onset of oscillation of the core flow is the Reynolds number of the side flow. This is in agreement with the numerical results by Lashgari *et al.* (2014), however, the critical Reynolds number differs by a factor 5. The liquid in the core flow is varied, by using fluids with different viscosities and a CNF dispersion. No effect was observed when changing the viscosity or type of liquid, indicating the possibility to use any type of liquid when investigating the flow in this and similar devices.

In addition to altering the core fluid, efforts are made to extend the operational window, *i.e.* delay the onset of oscillations of the core, by rounding two previously sharp corners at which simulations predicted recirculation zones to form. This control of flow stability fails, and the transition happens at lower Reynolds number compared to the original device. The reason for this unexpected result could be due to the accuracy in the manufacturing (~ 10 μm) creating a small asymmetry, or a result of wall effects.

In order to stabilise the flow at higher Reynolds numbers, there are many possible variations of the setup that could achieve this; non-orthogonal side channels, downstream corners with larger radius, suction at the corner. However, all these would stabilise the flow only if there exist a recirculation bubble which is responsible for the transition, as was suggested by Lashgari *et al.* (2014). In order to discover the reason for the transition, detailed measurements of the flow in the device are needed. μPIV measurements at a few positions for a few parameter combinations would provide a solid ground for further development of flow focusing devices. In order for the simulations to approach the experiments, 3-dimensional simulations are needed for different channel depths to understand the importance of wall effects. By combining experimental measurements of the flow with 3-dimensional simulations, a deeper understanding of the reason for the onset of oscillations can be reached.

CHAPTER 6

Papers & author contributions

Paper 1
Fibre orientation and fibre streaks in turbulent wall bounded flow
M. Kvick (MK), K. M. O. Håkansson (KMOH), F. Lundell (FL), L. Prahl Wittberg (LPW) & L. D. Söderberg (DS)
To be submitted.

The orientation and spatial distribution of fibres in a turbulent wall bounded flow is studied experimentally. MK and KMOH performed a majority of the experiments and analysis in close collaboration under supervision of FL, LPW and DS. In addition, KMOH performed the LDV measurements and MK implemented the anisotropy as an analysis method. MK, KMOH, FL and LPW wrote the paper jointly with input from DS.
Parts of these results have been published in:

> *Streak Formation and Fibre Orientation in Near Wall Turbulent Fibre Suspension Flow*
> M. Kvick, K. Håkansson, F. Lundell, L. D. Söderberg & L. Prahl Wittberg
> **ERCOFTAC bulletin, 2010, Vol. 84**

> *Fibre Streaks in Wall Bounded Turbulent Flow*
> M. Kvick, K. Håkansson, F. Lundell, L. D. Söderberg & L. Prahl Wittberg
> **7$^{\text{th}}$ Int. Conf. on Multiphase Flow**
> May 30 – June 4 2010 6.5.4, *Tampa, FL, USA*

Paper 2
Measurement of width and intensity of particle streaks in turbulent flows
K. M. O. Håkansson (KMOH), M. Kvick (MK), F. Lundell (FL), L. Prahl Wittberg (LPW) & L. D. Söderberg (DS)
Published in *Experiments in Fluids* (2013) **54** (6)

A new method for the quantification of particle streaks is developed. KMOH and MK developed the method and performed the analysis under supervision of FL, LPW and DS. KMOH investigated and accounted for the dependence of concentration, image size, artificial particle size and streak width in the method. MK incorporated the Voronoi method into the analysis. KMOH, MK, FL and LPW wrote the paper jointly with input from DS.

Paper 3
Effects of fibrils on curvature- and rotation-induced hydrodynamic stability
M. Kvick (MK), F. Lundell (FL), L. Prahl Wittberg (LPW) & L. D. Söderberg (DS)
Published in *Acta Mechanica* (2013) **224** (10)

The effect of nano-fibrillated cellulose on instability is studied experimentally and theoretically in a curved rotating channel. MK performed the experiments and analysis under supervision of FL, LPW and DS. MK wrote the paper with input from FL, LPW and DS.
Due to an algebraic error in the calculation of the theoretical viscosity, a corrigendum has been submitted to *Acta Mechanica*. The corrigendum has been incorporated in the text.

Paper 4
Effect of fibres on hydrodynamic stability in a curved rotating channel
M. Kvick (MK), F. Lundell (FL), L. Prahl Wittberg (LPW) & L. D. Söderberg (DS)
Published in *Proceedings of 8^{th} International Conference on Multiphase Flows* (2013) ICMF2013-674

The effect of nano-fibrillated cellulose on instability in a curved, rotating channel is studied theoretically. MK wrote the code and performed the analysis under supervision of FL, LPW and DS. MK wrote the paper with input from FL, LPW and DS.

Paper 5
Effect of cellulose nano fibrils on transitional two-dimensional flow
M. Kvick (MK), K. Watanabe (KW), M. Miyazaki (MMI), M. Matsubara (MMA), F. Lundell (FL) & L. D. Söderberg (DS)
Manuscript in preparation

The effect of cellulose nanofibrils on transition in a plane channel is studied experimentally and theoretically. MK, KW and MMI performed the experiments with input from MMA. MK wrote the code and carried out the analysis under supervision of FL. MK and MMI wrote the paper with input from MMA, FL

and DS.

Paper 6
The stability of the flow in a flow-focusing device
M. Kvick (MK), F. Lundell (FL) & L. D. Söderberg (DS)
Manuscript in preparation

The stability of the flow in a flow-focusing device is investigated. Variations of the experimental setup and different fluids are studied. MK designed and performed the experiments with input from FL and DS. MK wrote the paper with input from FL and DS.

Paper 7
Producing film from cellulose nano fibrils using a flow focusing device
M. Kvick (MK), F. Lundell (FL) & L. D. Söderberg (DS)
Manuscript in preparation

A flow focusing device is used in order to produce thin, transparent, films made solely out of cellulose nanofibrils. MK performed the experiments with input from FL and DS. MK wrote the paper with input from FL and DS.

Part of this work has been presented by the author at:

7th International Conference on Multiphase Flow, May 30 - June 4, 2010, *Tampa, FL, USA*

513th Euromech Colloquium on "Dynamics of non-spherical particles in fluid turbulence", April 6-8, 2011, *Udine, Italy*

SPCI Event, May 17-19, 2011, *Stockholm, Sweden*

Svenska Mekanikdagarna, June 13-15, 2011, *Göteborg, Sweden*

SIAMUF Autumn meeting, October 20-21, 2011, *Göteborg, Sweden*

9th International Conference on Flow Dynamics, September 19-21, 2012, *Sendai, Japan*

4th ERCOFTAC SIG43 Workshop, October 24-26, 2012, *Trondheim, Norway*

8th International Conference on Multiphase Flow, May 26 - 31, 2013, *Jeju, Korea*

Svenska Mekanikdagarna, June 12-14, 2013, *Lund, Sweden*

Complex Fluids Symposium at Micronic Mydata AB, December 5, 2014, *Stockholm, Sweden*

Ekmandagarna, January 28-29, 2014, *Stockholm, Sweden*

COST Action FP1005 "Modelling of Fibre Suspension Flows", June 3-5, 2014, *Stockholm, Sweden*

APPENDIX A

Experimental setups

Four different experimental setups have been used throughout this thesis, they are presented in the following appendix.

A.1. Water table

In Paper 1 the orientation and spatial distribution of fibres in a turbulent wall bounded flow are investigated, a schematic drawing on the experimental setup used is shown in Fig A.1. Water is collected in the upstream reservoir, the flow down the following glass plate (2m $\times$ 0.6m) is due to an inclination (varied between) of the plate and therefore driven solely by gravity, resulting in a well defined flow with a known wall shear stress. The height of the water layer is varied between $0.5 - 2$cm. At the end of the plate, the fluid/suspension is collected and recirculated back to the upstream reservoir. A valve places after the recirculating pump is used to control the flow rate. At a downstream position where the flow is fully developed (confirmed by Laser Doppler Velocimetry), a camera is placed underneath the plate, acquiring images of the fibres in the flow.

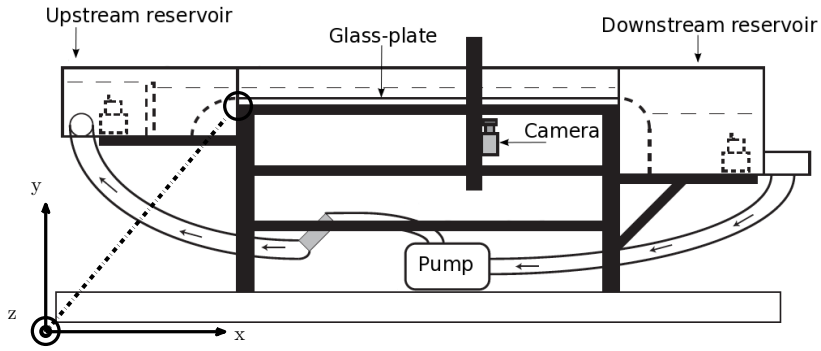

FIGURE A.1. **Water table.** Schematic setup of the water table used to study the orientation and distribution of cellulose fibres in turbulent flow close to a wall.

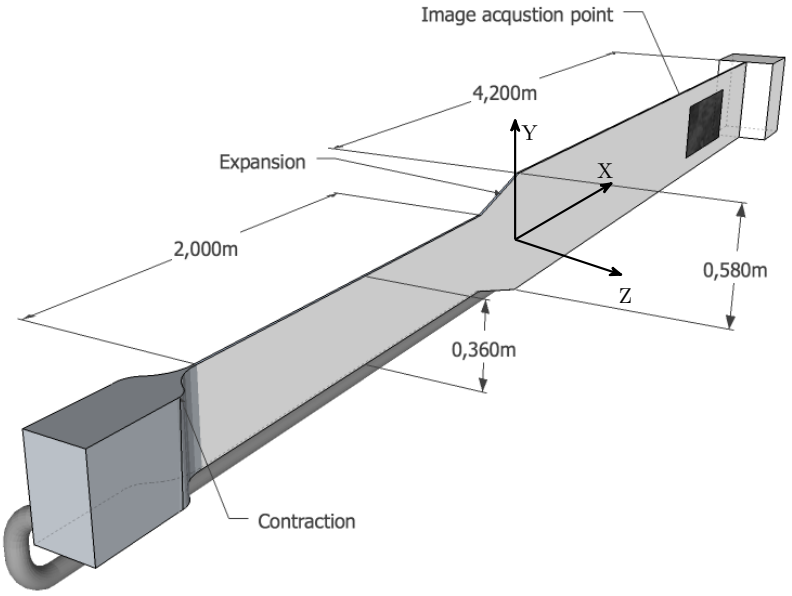

FIGURE A.2. **Plane channel.** Schematic drawing of the setup used in the plane channel flow experiments.

A.2. Plane channel

The experimental setup used in Paper 5 is shown in Fig. A.2. The main part of the channel consists of two glass plates, (4.2m $\times$ 0.58m) with a 7.1mm gap between them. The flow is after a contraction triggered to turbulence, a following spanwise expansion (with divergence angle of 15°) reduces the Reynolds number by 62%. If the flow rate is low enough, the initially turbulent flow will relaminarize, *i.e.* all disturbances will decay. The test section is placed at the end of the channel, whereafter the fluid is pumped back to the inlet. The static pressure in the channel is measured by inserting a tube from the end of the channel and measurements are performed at locations separated by a distance $\Delta x = 0.3$ m, starting at $x = 3$ m. The static pressure tube consist of a 90 mm long pipe with diameter 2.1 mm connected to the pressure transducer through a 2.5 m long aluminium tube with diameter 7.1 mm. Four 0.5 mm pressure holes are located 32 mm downstream of the tip. The flow rate is measured using an orifice flow meter located after the pump driving the flow.

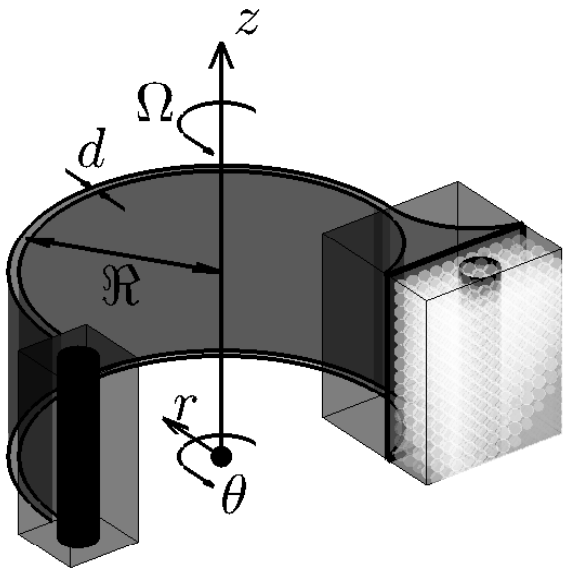

FIGURE A.3. **Curved-rotating channel.** Schematic drawing of the curved, rotating, channel. The inlet is to the right in the figure.

A.3. Curved-rotating channel

In Paper 3 & 4 the effect of fibres on the transition in a curved, rotating channel is examined. A sketch of the setup is depicted in Fig. A.3. In the inlet tank, located to the right in the figure, glass spheres are placed in order to remove large scale fluctuations. After that, a contraction is placed followed by the curved channel. The channel has a height of 0.28m and the distance between the channel walls are 9.25mm. Furthermore, the radius of curvature is 400mm. A small amount of dish shaped pearl particles are mixed with the fluid (the amount used did not affect the viscosity or the flow dynamics), and images of the structures in the flow are captured by a camera placed 65 channel widths downstream of the inlet. The flow rate is adjusted by valves placed before the inlet and and after the outlet and is measured using a rotameter. The rotation rate is controlled using a power source.

A.4. Flow focusing device

The stability of the flow in a flow focusing device, shown in Fig. A.4, is investigated in Paper 6. A similar device is used in Paper 7 where a process to manufacture film from CNF is demonstrated. The flow focusing device consists of an intersection of four channels, three inlets and one outlet. The device is manufactured in stainless steel with plexiglas and aluminium. In Paper 7,

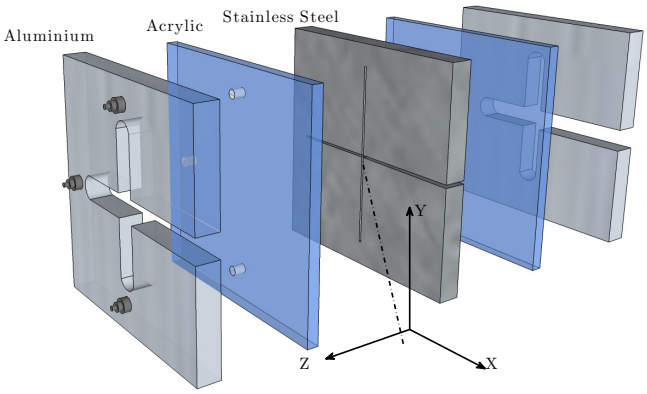

FIGURE A.4. **Flow focusing unit.** Sketch of the flow focusing device.

the device consists of 2 serial intersections, where the purpose of the first intersection is to create a lubrication layer, thereby preventing clogging of the channel.

Acknowledgements

The *Wallenberg Wood Science Center* (WWSC), through the *Knut and Alice Wallenberg foundation* is greatly acknowledged for the funding of this work.

——

I would like to thank my supervisors for helping me through these years; Fredrik Lundell for his everlasting enthusiasm and for teaching me how to be a scientist, Daniel Söderberg for helping me understand how my research relates to the real world and explaining the bigger picture, Lisa Prahl Wittberg for aiding me in my writing and teaching me how to express myself.

Thank you Karl, for all the fun we had, both in the lab and around the world.

A great thanks to technicians, Joakim Karlström, Göran Rådberg, Jonas Vikström and Rune Lindfors, for their help in the design and manufacturing of experimental equipment. A big thank you also to Malin Landin, for being there and answering questions of a more non-scientific nature.

Professor Masaharu Matsubara, Kenta Watanabe and Makato Miyazaki are greatly acknowledged for taking care of me during my stays in Nagano.

Till slut, tack mamma och pappa för att ni stöttat mig under den här tiden.

Thank you!

September 2014, Stockholm
Mathias Kvick

References

Advani, S. G. & Tucker III, C. L. 1987 The use of tensors to describe and predict fiber orientation in short fiber composites. *J. Rheol.* **31** (8), 751–784.

Åkervik, E., Ehrenstein, U., Gallaire, F. & Henningson, D. S. 2008 Global two-dimensional stability measures of the flat plate boundary-layer flow. *Eur. J. Mech. B-Fluids* **27** (5), 501–513.

Andersson, H. I., Zhao, L. & Barri, M. 2012 Torque-coupling and particle-turbulence interactions. *J. Fluid Mech.* **696**, 319–329.

Andrić, J., Fredriksson, S. T., Lindström, S. B., Sasic, S. & Nilsson, H. 2013 A study of a flexible fiber model and its behavior in DNS of turbulent channel flow. *Acta Mech.* **224** (10), 2359–2374.

Ashori, A. 2008 Wood-plastic composites as promising green-composites for automotive industries! *Bioresource Technol.* **99** (11), 4661–4667.

Avila, M. & Hof, B. 2013 Nature of laminar-turbulence intermittency in shear flows. *Phys. Rev. E* **87**, 063012.

Azaiez, J. 2000 Linear stability of free shear flows of fibre suspensions. *J. Fluid Mech.* **404**, 179–209.

Bark, F. H. & Tinoco, H. 1978 Stability of plane Poiseuille flow of a dilute suspension of slender fibres. *J. Fluid Mech.* **87**, 321–333.

Batchelor, G. K. 1970 The stress system in a suspension of force-free particles. *J. Fluid Mech.* **41** (03), 545–570.

Batchelor, G. K. 1971 The stress generated in a non-dilute suspension of elongated particles by pure straining motion. *J. Fluid Mech.* **46** (04), 813–829.

Berglund, L. A. & Peijs, T. 2010 Cellulose biocomposites from bulk moldings to nanostructured systems. *MRS Bulletin* **35**, 201–207.

Cox, H. L. 1952 The elasticity and strength of paper and other fibrous materials. *Brit. J. Appl. Phys.* **3** (3), 72.

Dinh, S. M. & Armstrong, R. C. 1984 A rheological equation of state for semi-concentrated fiber suspensions. *J. Rheol.* **28** (3), 207–227.

Doi, M. & Edwards, S. F. 1986 *The Theory of Polymer Dynamics*. Oxford University Press.

Eichhorn, S., Dufresne, A., Aranguren, M., Marcovich, N., Capadona, J., Rowan, S., Weder, C., Thielemans, W., Roman, M., Renneckar, S.,

Gindl, W., Veigel, S., Keckes, J., Yano, H., Abe, K., Nogi, M., Nakagaito, A., Mangalam, A., Simonsen, J., Benight, A., Bismarck, A., Berglund, L. & Peijs, T. 2010 Review: current international research into cellulose nanofibres and nanocomposites. *J. Mater. Sci.* **45**, 1–33.

Einstein, A. 1906 Eine neue Bestimmung der Moleküldimensionen. *Ann. Phys.* **324** (2), 289–306.

Fall, A. B., Lindström, S. B., Sundman, O., Ödberg, L. & Wågberg, L. 2011 Colloidal stability of aqueous nanofibrillated cellulose dispersions. *Langmuir* **27** (18), 11332–11338.

Fessler, J. R., Kulick, J. D. & Eaton, J. K. 1994 Preferential concentration of heavy particles in a turbulent channel flow. *Phys. Fluids* **6** (11), 3742–3749.

Gerngross, T. U. & Slater, S. C. 2000 How green are green plastic? *Sci. Am.* pp. 36–41.

Gupta, V. K., Sureshkumar, R., Khomami, B. & Azaiez, J. 2002 Centrifugal instability of semidilute non-Brownian fiber suspensions. *Phys. Fluids* **14** (6), 1958–1971.

Håkansson, K. M. O., Fall, A. B., Lundell, F., Yu, S., Krywka, C., V., R. S., Santoro, G., Kvick, M., Prahl Wittberg, L., Wågberg, L. & Söderberg, L. D. 2014 Hydrodynamic alignment and assembly of nanofibrils resulting in strong cellulose filaments. *Nat. Commun.* **5**, 4018.

Håkansson, K. M. O., Kvick, M., Lundell, F., Prahl Wittberg, L. & Söderberg, L. D. 2013 Measurement of width and intensity of particle streaks in turbulent flows. *Exp. Fluids* **54** (6), 1555.

Jeffery, G. B. 1922 The motion of ellipsoidal particles immersed in a viscous fluid. *P. Roy. Soc. A* **102** (715), 161–179.

Kaftori, D., Hetsroni, G. & Banerjee, S. 1995 Particle behavior in the turbulent boundary layer. I. Motion, deposition, and entrainment. *Phys. Fluids* **7** (5), 1095–1106.

Kerekes, R. J. 2006 Rheology of fibre suspensions in papermaking: An overview of recent research. *Nordic Pulp Paper Res. J.* **21**, 598–612.

Klinkenberg, J., de Lange, H. C. & Brandt, L. 2011 Modal and non-modal stability of particle-laden channel flow. *Phys. Fluids* **23** (6).

Kundu, K. P. & Cohen, I. M. 2004 *Fluid Mechanics*, 3rd edn. Elsevier Inc.

Kvick, M., Håkansson, K. M. O., Lundell, F., Prahl Wittberg, L. & Söderberg, L. D. 2014*a* Fibre orientation and fibre streaks in turbulent wall bounded flow *To be submitted.*

Kvick, M., Lundell, F., Prahl Wittberg, L. & Söderberg, L. D. 2013*a* Effect of fibres on hydrodynamic stability in a curved rotating channel. In *8th Int. Conf. on Multiphase Flow*, *ICMF2013* 674. Jeju, Korea.

Kvick, M., Lundell, F., Prahl Wittberg, L. & Söderberg, L. D. 2013*b* Effect of fibrils on curvature- and rotation-induced hydrodynamic stability. *Acta Mech.* **224** (10), 2249–2261.

Kvick, M., Lundell, F., Prahl Wittberg, L. & Söderberg, L. D. 2014*b* Stability of the flow in a flow-focusing device *Manuscript.*

Kvick, M., Lundell, F. & Söderberg, L. D. 2014*c* Producing film from cellulose nanofibrils using a flow focusing device *Manuscript*.

Kvick, M., Watanabe, K., Miyazaki, M., Matsubara, M., Lundell, F. & Söderberg, L. D. 2014*d* Fibre suspension flow in a plane channel: transition delay by cellulose nanofibrils *Manuscript*.

Lashgari, I., Tammisola, O., Citro, V., Juniper, M. P. & Brandt, L. 2014 The planar X-junction flow: stability analysis and control. *J. Fluid Mech.* **753**, 1–28.

Leal, L. & Hinch, E. 1973 Theoretical studies of a suspension of rigid particles affected by brownian couples. *Rheologica Acta* **12** (2), 127–132.

Marchioli, C., Fantoni, M. & Soldati, A. 2010 Orientation, distribution, and deposition of elongated, inertial fibers in turbulent channel flow. *Phys. Fluids* **22** (3), 033301.

Matsson, O. J. E. & Alfredsson, P. H. 1990 Curvature- and rotation-induced instabilities in channel flow. *J. Fluid Mech.* **210**, 537–563.

Matsson, O. J. E. & Alfredsson, P. H. 1992 Experiments on instabilities in curved channel flow. *Phys. Fluids A-Fluid* **4** (8), 1666–1676.

Meikle, J. L. 1995 *American Plastic: A Cultural History*. Rutgers University Press.

Mohanty, A. K., Misra, M. & Hinrichsen, G. 2000 Biofibres, biodegradable polymers and biocomposites: An overview. *Macromol. Mater. Eng.* **276–277** (1), 1–24.

Monchaux, R., Bourgoin, M. & Cartellier, A. 2010 Preferential concentration of heavy particles: A Voronoï analysis. *Phys. Fluids* **22** (10), 103304.

Mortensen, P., Andersson, H., Gillissen, J. & Boersma, B. 2008 On the orientation of ellipsoidal particles in a turbulent shear flow. *Int. J. Multiphase Flow* **34** (7), 678–683.

Mueller, S., Llewellin, E. W. & Mader, H. M. 2010 The rheology of suspensions of solid particles. *Proc. Roy. Soc. A* **466** (2116), 1201–1228.

Nsom, B. 1996 Stability of fiber suspension flow in curved channel. *J. Phys. II* **6** (10), 1483–1492.

Orszag, S. A. 1971 Accurate solution of the Orr-Sommerfeld stability equation. *J. Fluid Mech.* **50**, 689–703.

Pääkkö, M., Ankerfors, M., Kosonen, H., Nykänen, A., Ahola, S., Österberg, M., Ruokolainen, J., Laine, J., Larsson, P. T., Ikkala, O. & Lindström, T. 2007 Enzymatic hydrolysis combined with mechanical shearing and high-pressure homogenization for nanoscale cellulose fibrils and strong gels. *Biomacromolecules* **8** (6), 1934–1941.

Patel, V. C. & Head, M. R. 1969 Some observations on skin friction and velocity profiles in fully developed pipe and channel flows. *J. Fluid Mech.* **38**, 181–201.

Petrie, C. J. 1999 The rheology of fibre suspensions. *J. Non-Newton Fluid* **87** (2–3), 369–402.

Phan-Thien, N. & Graham, A. L. 1991 A new constitutive model for fibre suspensions: flow past a sphere. *Rheol. Acta* **30**, 44–57.

Pilipenko, V. N., Kalinichenko, N. M. & Lemak, A. S. 1981 Stability of the

flow of a fiber suspension in the gap between coaxial cylinders. *Soviet Physics Doklady* **26**, 646.

Radin, I., Zakin, J. L. & Patterson, G. K. 1975 Drag reduction in solid-fluid systems. *AIChE J.* **21** (2), 358–371.

Rowbotham, E. M. 1948 Fiber orientation in fiber-reinforced plastics and how it affects automotive applications. In *Automotive Engineering Congress, Detroit*. Society of Automotive Engineers.

Schmid, P. J. & Henningson, D. S. 2001 *Stability and Transition in Shear Flows*. Springer, New York.

Seki, D. & Matsubara, M. 2012 Experimental investigation of relaminarizing and transitional channel flows. *Phys. Fluids* **24** (12), 124102.

Shaqfeh, E. S. G. & Fredrickson, G. H. 1990 The hydrodynamic stress in a suspension of rods. *Phys. Fluids A* **2** (1), 7–24.

Shen, L. & Patel, M. K. 2008 Life cycle assessment of polysaccharide materials: A review. *J. Polym. Environ.* **16** (2), 154–167.

Shent, H., Pugh, R. & Forssberg, E. 1999 A review of plastics waste recycling and the flotation of plastics. *Resour. Conserv. Recy.* **25** (2), 85 – 109.

Skogsindustrierna 2014 Så går det för skogsindustrin. Om den svenska pappers-, massa- och sågverksindustrin, June.

Skogsstyrelsen 2013 Skogsstatistisk årsbok.

Trefethen, L. N., Trefethen, A. E., Reddy, S. C. & Driscoll, T. A. 1993 Hydrodynamic stability without eigenvalues. *Science* **261** (5121), 578–584.

Turbak, A., Snyder, F. & Sandberg, K. 1983 Microfibrillated cellulose, a new cellulose product: properties, uses, and commercial potential. In *J. Appl. Polym. Sci., Applied Polymer Symposium 37*.

Wågberg, L., Winter, L., Ödberg, L. & Lindström, T. 1987 On the charge stoichiometry upon adsorption of a cationic polyelectrolyte on cellulosic materials. *Colloids Surf.* **27** (4), 163 – 173.

Zacksenhouse, M., Abramovich, G. & Hetsroni, G. 2001 Automatic spatial characterization of low-speed streaks from thermal images. *Exp. Fluids* **31** (2), 229–239.

Zhao, L. H., Andersson, H. I. & Gillissen, J. J. J. 2010 Turbulence modulation and drag reduction by spherical particles. *Phys. Fluids* **22** (8), 081702.

Zhenjiang, Y., Jianzhong, L. & Zhaosheng, Y. 2004 Hydrodynamic instability of fiber suspensions in channel flows. *Fluid. Dyn. Res.* **34** (4), 251–271.

Part II

Papers

1

Paper 1

Fibre orientation and fibre streaks in turbulent wall bounded flow

By Mathias Kvick[1,2], Karl M. O. Håkansson[1,2], Fredrik Lundell[1,2], Lisa Prahl Wittberg[1,2] & L. Daniel Söderberg[1]

[1] Wallenberg Wood Science Center, KTH Mechanics, Royal Institute of Technology, SE – 100 44, Stockholm, Sweden
[2] Linné Flow Centre, KTH Mechanics, Royal Institute of Technology, SE – 100 44, Stockholm, Sweden

To be submitted

The behaviour of fibres in a wall bounded turbulent shear flow is investigated. Understanding and modelling of fibre suspension flow is necessary for improvements in many applications, e.g. papermaking. Experimental data covering wide parameter spaces is an important ingredient in this effort. As a means to address this need a dilute fibre suspension flowing down an inclined glass plate is studied. Images of the fibres in the flow are acquired from beneath the glass plate and the images are analysed using a steerable filter, providing the position and orientation of the fibres. Both fibre orientation distributions and spatial distributions are investigated. It is found that the aspect ratio of the fibres plays an important role in the overall fibre orientation distribution, while other effects such as turbulence, concentration and wall interactions are of secondary importance. Short fibres were found to orient normal to the flow, while longer fibres aligned in the flow direction. Moreover, the fibres agglomerated into streamwise streaks, with widths slightly larger than the width of the low velocity streaks.

1. Introduction

There are many reasons for studying the behaviour of elongated particles in flows. The motivation comes from both engineering (e.g. biomaterial transport, separation and processing) and geophysical flows (e.g. sediment transport and atmospheric aerosols). Here, the behaviour of fibres in turbulent channel flow is studied. The direct motivation lies in the fact that it is now possible to simulate a large number of fibres in turbulent flow with different methods and in order to validate these methods, experimental data is needed.

Turbulent channel flow has proven to be an excellent platform for extracting knowledge from direct numerical simulations ever since it was first simulated directly by Kim *et al.* (1987). With a direct simulation, we mean that

the governing equations are solved in time without any approximations. The strength of channel flow is that it is a flow case that is fairly straightforward to model with efficient numerical methods while also being possible to realise in physical experiments with good accuracy. The number of easily accessible scientific works considering different aspects of turbulent channel flow seems to be more than 15000; we will not make any attempt to review this vast literature. Instead, we focus on recent studies that has inspired this work and works on the phenomena that are at play in the channel: shear, turbulence, gravity and the wall boundary condition.

Turbulent channel flows in which fibres are contained can be simulated by different means. It could be argued that the most mature approach is point-particle fibres tracked in a direct numerical simulation of the fluid (Zhang *et al.* 2001; Marchioli *et al.* 2010; Mortensen *et al.* 2008). The particles are then assumed to be infinitesimally small. The forces and torques on each particle is in each time step calculated from the local velocity gradient assuming Stokes flow (Stokes 1856; Jeffery 1922) and coupled with the translational and rotational equations of motion of the particle. This makes it possible to calculate the translational motion and rotation of the particles in the flow field. The forces (and torques) on the particle can also be coupled back to the flow (Andersson *et al.* 2012). Parameters that can be varied are fibre aspect ratio and fibre inertia. Detected effects are fibre redistribution due to the turbulence (accumulation in low speed streaks) and fibre orientation (tendency of heavy particles to align with the flow).

If the fibres are assumed to have a finite size, the problem gets more complicated since the assumption of Stokes flow around the particle is note necessarily valid. One must then either calculate forces and torques for a large number of particle and flow configurations a priori and then use this data in a look-up table when simulating the particle motion. The look-up table approach has successfully been used for spheres (Jadoon & Revstedt 2010). However, when non-spherical particles are studied, the parameter space grows since the orientation and rotational velocities of the particle must be taken into account. Thus, no complete look-up table has been produced yet. Nevertheless, van Wachem *et al.* (2013) used a look-up table restricted to steady differently oriented particles in constant flow, together with models for particle-wall interaction and particle-particle interactions. The results showed that slight differences in particle-wall interaction can cause major differences in fibre distribution.

Using the Lattice Boltzmann Method together with External Boundary Forcing, Do-Quang *et al.* (2014) performed a full simulation of finite sized particles in a turbulent channel flow. The fibres were near buoyant, *i.e.* had a density close to the fluid. The fibres tended to assemble in high speed streaks and longer fibres (more slender) showed an increased tendency to align in the flow direction.

It is worth noticing that in spite of the ever increasing computational capacity, all studies above have been forced to make severe simplifications or restrictions regarding fluid-particle interaction, particle-particle interaction, particle-wall interaction and presence of gravity. Nevertheless, it has been demonstrated that turbulent channel flow of fibre suspensions provides a well defined test case where the importance of different aspects can be studied.

It could be argued that the major aspects of this flow case are the behaviour of the turbulent flow as such, sedimentation of particles, particles in turbulence, particles in shear, particle-wall interaction and particle-particle interaction. The present experiments involve all these aspects and will therefore be introduced briefly. It is believed that the influence of each aspect will differ depending on the controlling parameters (a dimensional analysis of the problem is presented in section 3).

A sedimenting fibre suspension is subjected to an instability that produces risers and streamers, i.e. regions of upwards and downwards flowing fluid, respectively. The fibres tend to assemble in the streamers (the increased fibre concentration actually drives the streamer) (Koch & Shaqfeh 1989; Saintillan *et al.* 2005; Gustavsson & Tornberg 2009; Zhang *et al.* 2013).

The fibres are also influenced by the presence of the wall. Experiments in a very viscous laminar flow (Carlsson *et al.* 2007; Holm & Söderberg 2007) has demonstrated that fibres can either "pole-vault" (Stover & Cohen 1990), i.e. remain aligned in the flow direction, rotate and be pushed out from the wall at each rotation or turn and sink so that their orientation is normal to the flow direction.

These effects are complemented by the effects of the wall normal velocity gradient. It is well known that elongated particles in shear show a wide variety of motions controlled by fluid and particle inertia. In viscous flow (where no inertia acts), a particle will rotate in a Jeffery orbit (Jeffery 1922) which are either tumbling, kayaking or log-rolling. As fluid and/or particle inertia is increased, some of these orbits becomes unstable and develop into attractors (Subramanian & Koch 2006; Einarsson *et al.* 2014; Lundell & Carlsson 2010). As the effects of inertia increases even more, new attractors can appear and the dynamics gets even more involved (Aidun *et al.* 1998; Rosén *et al.* 2014).

Furthermore, fibres or elongated particles in homogeneous turbulence provides an interesting flow case of its own. Recent experiments show that fibres tend to rotate around their longest axis and that the interactions between fibres and turbulent eddies depends on the relative orientation between fibres and vorticity (Bellani *et al.* 2012; Parsa *et al.* 2012).

The present work provides an extensive study of the orientation and distribution of fibres in turbulent channel flow. The fibres are slightly heavier than the fluid (density ratio 1.3) and all parameters but the density ratio and the fibre diameter are varied. Data is obtained by analysis of images of the fibres

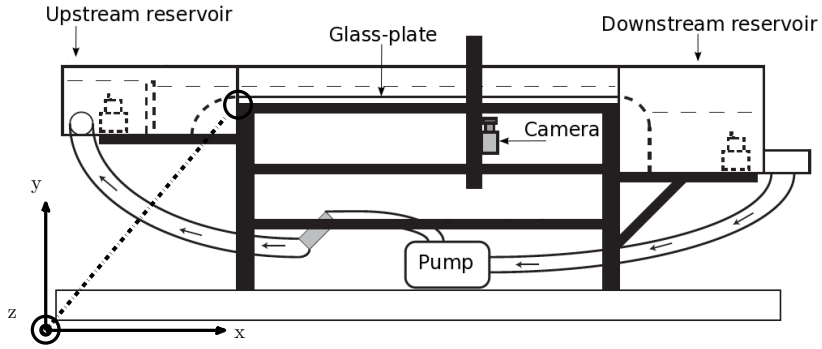

FIGURE 1. Schematic of the experimental setup, the length of the glass plate is approximately 2 m and the width 0.6 m

in the flow. In this flow case, it is noted that fibre aspect ratio seems to control the orientation and turbulence seems to control the fibre distribution.

This introduction is followed by section 2 where the flow apparatus, the fibres, image acquisition and image analysis are described. Section 3 details the physical parameters controlling the flow and introduces the six non-dimensional groups that we have chosen as the minimum necessary to describe this flow case. Quantified data on orientation distributions, fibre orientation anisotropy and fibre streaks are presented in section 4 and some aspects are discussed in section 5. Finally, the conclusions are summarised in section 6.

2. Method

2.1. *Flow apparatus and fibre suspension*

The experiments were performed at the KTH water-table seen in Fig. 1. The flow loop consists of a pump, an upper reservoir, the measurement section, a lower reservoir and piping connecting the reservoirs with the pump. In the measurement section, a liquid or suspension is allowed to flow down an inclined glass plate (2 m $\times$ 0.6 m with vertical glass side walls), where the flow is driven by gravity alone. A valve right after the pump adjusted the flow rate in the loop. The thickness of the fluid layer on the glass plate was in the range 0.5–2 cm and the surface velocity was typically 0.2 m/s. Small submersible pumps were positioned in the basins for stirring. The coordinate system (x, y, z) is defined as depicted in Fig. 1, where $x = 0$ is the start of the glass plate, $y = 0$ at the wall (glass plate) and $z = 0$ is located in the centre of the channel. The velocity components are (u, v, w).

The flow down the glass plate is an approximation of a half channel flow. The viscosity ratio between the air and the liquid is several orders of magnitude, thus, the velocity gradient in the liquid or suspension at the free surface is very

small, as it is on the centreline in a channel flow. The flow conditions are controlled by adjusting the inclination of the glass plate to the horizontal α and/or the height of the liquid or suspension layer h. Since the flow is driven by gravity alone, the wall shear stress, τ_w, can be calculated from first principles by considering a force balance between the liquid layer and the wall Acheson (1995). The wall shear stress is found to be:

$$\tau_w = \rho_f g h \sin\alpha, \tag{1}$$

where ρ_f is the density of the liquid (fluid) and g is the gravitational acceleration. The friction velocity u_τ is obtained as:

$$u_\tau = \sqrt{\frac{\tau_w}{\rho_f}} \tag{2}$$

and the friction Reynolds number Re_τ:

$$\mathrm{Re}_\tau = \frac{u_\tau h}{\nu} \tag{3}$$

where ν is the kinematic viscosity of the liquid.

The flow conditions were verified by comparing Laser Doppler Velocimetry (LDV) velocity measurements in pure water with hollow glass spheres ($d = 20\mu m$) as tracer particles with a Direct Numerical Simulation (DNS) of turbulent channel flow. Mean streamwise velocity and *rms*-profiles measured at $\mathrm{Re}_\tau = 88$ are seen in Fig 2a and Fig 2b, respectively. The velocity is normalized with u_τ: $u^+ = u/u_\tau$ and the vertical coordinate with the viscous length scale $l^+ = \nu/u_\tau$: $y^+ = y/l^+$. Measurements were performed at four positions. These positions were chosen as the standard position where fibres were visualised, one position upstream and one position on each side of this position: $(x, z) = (1100, 0)$ mm, $(800, 0)$ mm and $(1100, \pm 200)$ mm. All profiles are seen to collapse and when compared to DNS at $\mathrm{Re}_\tau = 80$, Tsukahara *et al.* (2005), a good agreement is observed. The degree to which the fibres effect the flow has not been investigated.

Tap water was used as liquid in all experiments. The particles were rigid cellulose acetate fibres with the density $\rho_p = 1300$ kg/m^3, diameter $d_p = 72$ μm and three different lengths $l_p = 0.5$, 1, 2 mm. The resulting aspect ratios $r_p = l_p/d_p$ are 7, 14 and 28. The fibres were died black and used in mono-disperse suspensions. The concentration by weight was in the range $c = 0.00042 - 0.0033\%$. One series of measurement was performed with Poly-Ethylene-Oxide (PEO), a polymer with a molecular weight of approx. $4 \cdot 10^6$ (commercial name PEG 90M) mixed with the water at a concentration of 40 ppm.

In order to ensure that the data mirrors the actual conditions, the concentration of each case is determined based on the number of fibres actually present (this number is obtained from the image analysis, see below). The number of fibres on the inclined plate could be both higher and lower than what could be

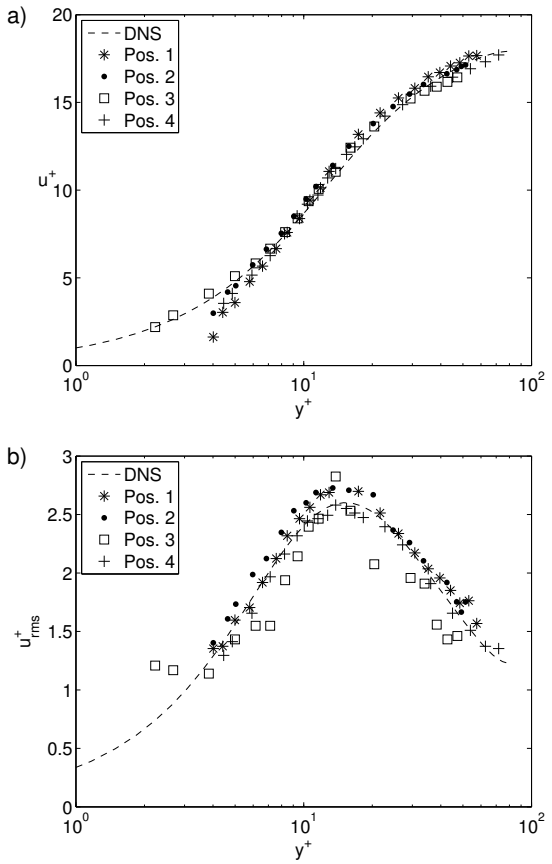

FIGURE 2. Velocity statistics measured by LDV at (∗):(x, z) = (1100, 0) mm, (•): (x,z) = (1100, 200) mm, (□): (x,z) = (1100, -200) mm and (+): (x,z) = (800, 0) mm at Re_τ=88. The experimental data is compared with data from a full channel flow DNS at $\mathrm{Re}_\tau = 88$ by Tsukahara *et al.* (2005). a) Streamwise mean velocity profiles. b) Streamwise velocity fluctuations.

expected based on the mean concentration in the suspension. The reason for this is that fibres could accumulate on the inclined plate and/or in other parts of the flow loop (upstream and downstream reservoirs and connectors).

It is important to note that the fibres are considerably heavier than the water. Therefore, the fibres sedimented towards the wall and most of the fibres appeared in a thin layer close to the wall.

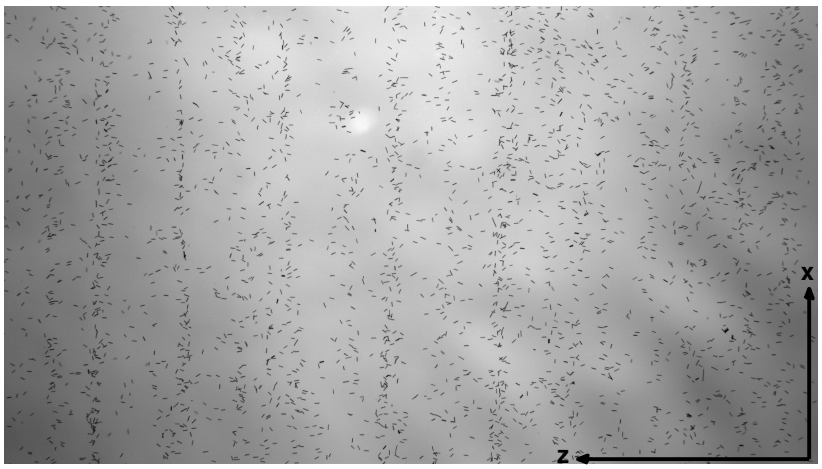

FIGURE 3. Typical image acquired during experiment. The flow is in the positive x-direction. The black fibres can clearly be seen in the flow. The image has the physical dimensions $\Delta x = 5$ cm and $\Delta z = 10$ cm.

2.2. *Image acquisition and fibre detection*

Images of the fibres in the turbulent flow were acquired by a camera (Basler piA1900-32gm) together with a flash, which was placed underneath the glass plate (see Fig. 1). The imaged area was 50×100 mm in the streamwise and spanwise directions, respectively. For standard acquisition, the camera and flash was mounted 1100 mm downstream of the start of the channel. In order to study the streamwise development of the fibre orientation, images were also acquired at $x = 700$, 800, 900, 1300 and 1500 mm.

The depth of field of the camera was always larger than the thickness of the water layer, hence, all fibres were in focus at all times. A typical image is shown in Fig. 3, where the fibres are seen as short black, straight lines. The intensity variations in the background are due to surface waves. In order to ensure statistically independent data, the time between images were chosen so that at least 95% of the fibres left the image before the next image was taken. The actual time between images was 3 s.

The two quantities determined from the images are the orientation in the plane parallel to the wall, β, ($\beta = 0$ in the flow direction), and the position in the streamwise-spanwise plane $(x - z)$ of the each fibre. The orientation and position of all fibres are extracted from the images using a second order ridge detector within the class of steerable filters (Jacob & Unser 2004), adapted for fibre detection, see Carlsson *et al.* (2011) for a detailed description and evaluation. The method detects fibre orientation with an accuracy of less than

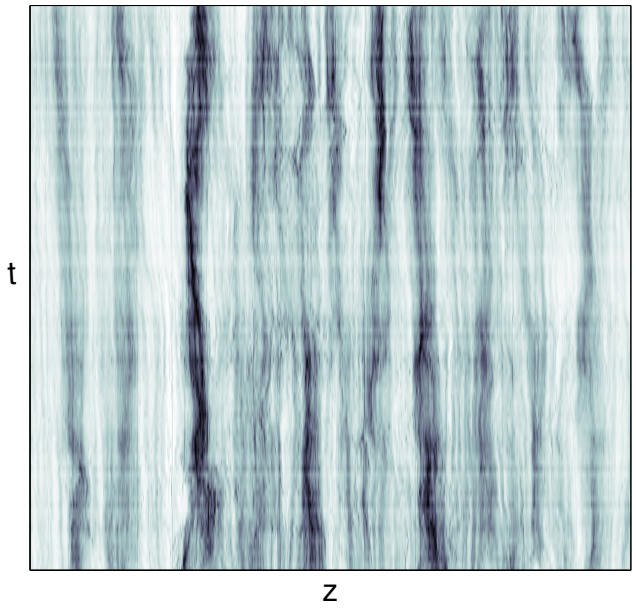

FIGURE 4. Temporal visualization of the fibre streaks, where each row corresponds to an image, such as Fig. 3, summed in the streamwise direction, $\Delta z = 10$ cm and the total time lapse $\Delta t = 7.7$ s.

1° for moderate levels of noise. At high concentrations, where individual fibres are hard to identify also for the eye, the method may fail. The actual limitations of the method in terms of concentration depend on image quality and aspect ratio of the particles. The ability of the method has to be determined by manual inspection of sample images for each case. No problems occurred when analysing the images from the present experiments.

Each image contains between 200–3000 fibres and for each case, 150 images were captured. Thus, the data for each case is based on 30,000–450,000 fibres.

2.3. *Anisotropy, streakiness and clustering*

The orientation distributions, $\Psi(\beta)$, are used to calculate an anisotropy measure, A, based on the second order orientation tensor, $\mathbf{a}_2$, (Advani & Tucker III 1987). In order to find the anisotropy, each fibre is associated with a unit vector in the plane of the image, $\mathbf{p} = (\cos\beta, \sin\beta)$. The second order orientation tensor is defined as $\mathbf{a}_2 = a_{ij} = p_i p_j$, and in this 2-dimensional case each

component takes the form:

$$a_{11} = \int \Psi(\beta) \cos^2 \beta \mathrm{d}\beta$$
$$a_{12} = a_{21} = \int \Psi(\beta) \cos \beta sin\beta \mathrm{d}\beta \tag{4}$$
$$a_{22} = \int \Psi(\beta) \sin^2 \beta \mathrm{d}\beta.$$

The anisotropy is obtained as:

$$A = a_{11}/a_{22}.$$

When observing Fig. 3, it is seen that the fibres tend to agglomerate in clear streamwise streaks. The streaks are further visualised in Fig. 4 where spanwise fibre density distributions from sequential images are shown. The spanwise distributions (rows of Fig. 4) are obtained by adding the grayscale values of each image in the streamwise direction. It is seen that the streaks are persistent during the time shown. The total time in this series is 7.7 s. The tendency of the fibres to agglomerate in streaks is quantified by a streakiness measure Ξ where $\Xi = 0$ means that the fibres have no particular order in the spanwise direction and $\Xi = 1$ means that all fibres are found in streaks that all have the same width. The mean streak width SW is also determined. The process to obtain Ξ and SW is presented and verified in a separate work, Håkansson *et al.* (2013). In short, the positions of the fibres are used together with correlation analysis with a focus on overcoming the severe concentration dependency connected to most other methods at low concentrations (e.g. Voronoi analysis or box counting methods).

Finally, we also use Voronoi (Aurenhammer 1991) analysis to distinguish between fibres inside and outside clusters (in our case, the relevant clusters are the streaks). Based on the fibre positions, the Voronoi analysis associates an polygonal area with each fibre where no other fibres are present. The Voronoi area is small for fibres in clusters and large for fibres outside clusters. Thus, the distribution of Voronoi areas can be used to select the 10% most and least clustered fibres in each image.

3. Dimensional analysis

The system at hand depends on nine independent physical variables that are tabulated in table 1. The physical variables are separated in those that control the particle-free flow and those that appear if fibres are added to the flow. The surface area density of fibres n_2 is the number of fibres in an image divided by the image area. The division of the gravitational acceleration in its parallel and orthogonal component has been made since the particle-free flow cannot distinguish a change in inclination angle from a change in gravity, as long as

Particle free flow	
h	Thickness of the fluid layer
$g_\parallel = g \sin\alpha$	Gravitational acceleration along the inclined glass plate
ρ_f	Density of the fluid
μ	Dynamic viscosity of the fluid
Flow with particles	
l_p	Length of the fibres
d_p	Diameter of the fibres
ρ_p	Density of the fibres
n_2	Surface area density of fibres
$g_\perp = g \cos\alpha$	Gravitational acceleration normal to the inclined glass plate

TABLE 1. Independent physical variables in the experiment.

the gravity does not reach zero. Thus, the gravitational acceleration along the plate is the physical parameter controlling the flow.

These variables contain three dimensions: mass, length and time. According to Buckingham's Π-theorem (Buckingham 1914), the number of non-dimensional groups necessary to describe the system is [number of variables] - [number of dimensions], in the present case $9 - 3 = 6$. Six independent groups are identified in table 2, where Re_p and S are defined. A very brief description of the physical relation described by each group is provided in the table and more detailed descriptions follow below. Through variation of r_p, h and α, wide parameter spaces are spanned (the total number of cases in this work is 116). Three projections of the parameter space covered are shown in figure 5 (a–c). The parameters Re_p, $n_2 l_p^2$ and S are shown as functions of Re_τ and the aspect ratio for each point is shown as the marker type. The sixth non-dimensional group, St_p, is obtained as $(\rho_p/\rho_f)\mathrm{Re}_p$ and since $(\rho_p/\rho_f) = 1.3$ is constant, the plot is very similar to Fig. 5 (a).

Note that even though the parameter variations might seem exhaustive at first sight, only three (Re_τ, r_p and $n_2 l_p^2$) of the six non-dimensional groups are varied independently since the density ratio, fibre diameter and gravitational acceleration normal to the plate are kept constant or near constant.

$\mathrm{Re}_\tau = \frac{u_\tau h}{\nu}$	Friction Reynolds number of the bulk flow.
$\mathrm{Re}_p = \frac{\dot{\gamma}_w l_p^2}{\nu}$	Particle Reynolds number quantifying the effects of fluid inertial on particle rotation in the mean shear.
$St_p = \frac{\rho_p}{\rho_f}\mathrm{Re}_p$	Particle Stokes number quantifying the effects of particle inertia on particle rotation in the mean shear.
$n_2 l_p^2$	Mean number of particles in a square prism with side l_p.
$r_p = \frac{l_p}{d_p}$	Aspect ratio of the fibres.
$S = T_{Jeff}/T_{sed}$	Time for a Jeffery orbit versus the time to sediment from a height of $l_p/2$ to the wall.

TABLE 2. Six non-dimensional groups with a short description of the physical phenomena they measure. A short comment on each group, including definitions of yet undefined quantities, is given in the text under separate headings. $\dot{\gamma}_w$ is the wall-normal gradient of the streamwise velocity at the wall; T_{Jeff} and T_{sed} are defined in the text.

In figure 5 (d), the parameter space spanned by an additional non-dimensional group, $l_p^+ = l_p/l^+$, i.e. the fibre length compared to the viscous length scale at the wall, is provided. Since this parameter describes the ratio of the fibre length to the smallest turbulent length scales, it could be expected that the fibre behaviour would be described by this parameter. However, it will soon be shown that the orientation distributions are not controlled by this parameter and that other effects are dominating.

3.1. *Friction Reynolds number Re_τ*

The friction Reynolds number is typically chosen to describe turbulent channel flow Kim *et al.* (1987). It is the ratio of the viscous length scale at the wall (also called frictional length scale) and half the channel height. Since our flow is half a turbulent channel flow, it is the ratio of the frictional length scale and the thickness of the water layer flowing down the inclined plate.

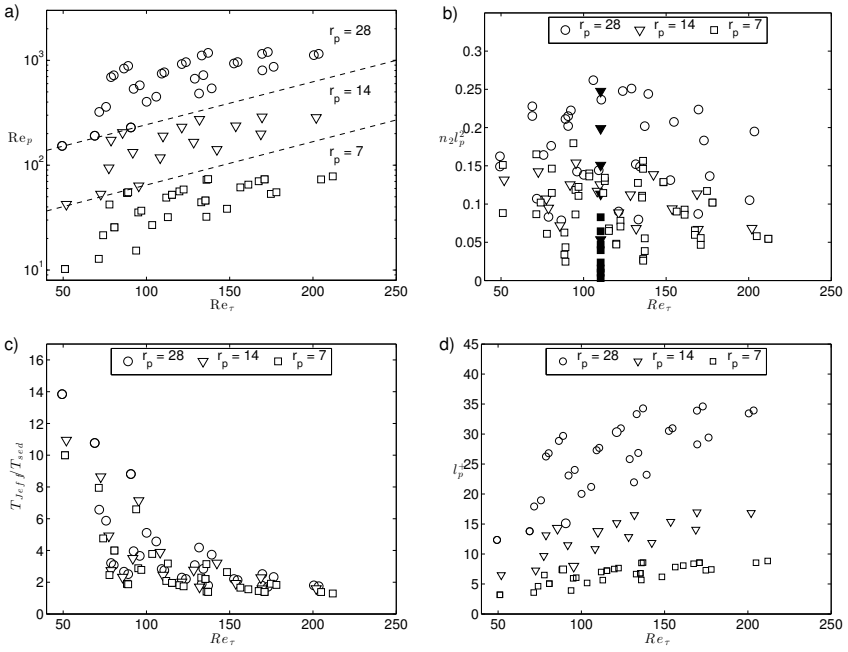

FIGURE 5. Different realizations of the parameter space studied.

3.2. *Particle Reynolds number* Re_p

Since our fibres rotate in a mean shear, the particle Reynolds number is based on the shear. We have chosen the shear at half a fibre length from the wall, since this is the closest position where a fibre aligned with the flow can perform a flip. The particle Reynolds number is one of the key parameters controlling particle rotation in shear. This has been shown in numerous analytical and numerical studies of single particles in shear, *e.g.* Aidun *et al.* (1998); Subramanian & Koch (2006); Qi & Luo (2002).

3.3. *Particle Stokes number* St_p

As the particle Reynolds number is increased, it is not only fluid inertia in the flow around the particle that comes into play. The rotational particle inertia, measured by St_p, enters the problem as well. In fact, the behaviour of a single particle in shear is actually determined by a competition (and sometimes cooperation) between fluid and particle inertia (Subramanian & Koch 2006; Lundell & Carlsson 2010; Rosén *et al.* 2013, 2014). Note that particle inertia is important also for neutrally buoyant particles, since the $St_p = Re_p$ in this case. In practice the density ratio is rarely much less than one but often much higher than one, particle inertia will therefore always be active, and often be

dominant (see Rosén *et al.* (2013, 2014) for details). Here, the particle-fluid density ratio is constant and it is therefore not possible to separate effects of particle and fluid inertia from each other. However, comparisons with single particle simulations can serve this purpose instead of tedious experiments with varying density, obtaining identical fibres with varying density is a non-trivial task and the fluid density can not be varied in a large range unless exotic (and often toxic) fluids are used.

3.4. *Concentration* $n_2 l_p^2$

Concentration in a fibre suspension is typically measured by $n_3 l_p^3$, where n_3 is the volume particle number density. This measures the mean number of particles in a cube with side length l_p and provides an estimation of to what extent fibres interact with each other. It is also the concentration parameter controlling the rheological properties of a dilute fibre suspension. Here, the non-dimensional concentration is based on surface rather than volume since the fibres are primarily present close to the wall due to sedimentation. Therefore, $n_2 l_p^2$ quantifies to what extent the fibres interact with each other: if this value is unity, fibre interactions start to occur. A volume averaged concentration measure would not give a proper description of the physical situation at hand.

3.5. *Aspect ratio* r_p

The aspect ratio controls the shape of the orbits that inertia-free fibres perform in unbounded shear flow (Jeffery 1922) and can therefore be expected to control the fibre behaviour in our experiments. In unbounded shear flow, the distance that fibre end points deviates from the flow-vorticity plane decreases as the aspect ratio increases (provided they are not perfectly aligned with the flow).

3.6. *Sedimentation parameter* S

The choice of parameter for the effects of sedimentation is not obvious. Here, the ratio between two time scales is used. The first timescale is the time it would take for an inertia-free cylinder to perform a flipping motion in the shear half a fibre length from the wall over $T_{Jeff} = 2\pi(r_e^2 + 1)/(\dot{\gamma}_{l_p/2} r_e)$ where $\dot{\gamma}_{l_p/2}$ is the shear half a fibre length from the wall (estimated from DNS data) and r_e is the equivalent ellipsoidal aspect ratio, $r_e = 1.14 r_p^{0.844}$(Harris & Pittman 1975). The second time scale is the time it would take for a fibre with horizontal alignment to sediment half a fibre length, $T_{sed} = l_p / v_{sed}$ where $v_{sed} = (\rho_p - \rho_f)(d_p^2/16\nu\rho_f)[\log(2r_p) + 0.193]g$ (Herzhaft & Guazzelli 1999; Batchelor 1970). The inverse of this ratio gives an idea of how many times a fibre end point touches the wall before its centre point reaches the wall.

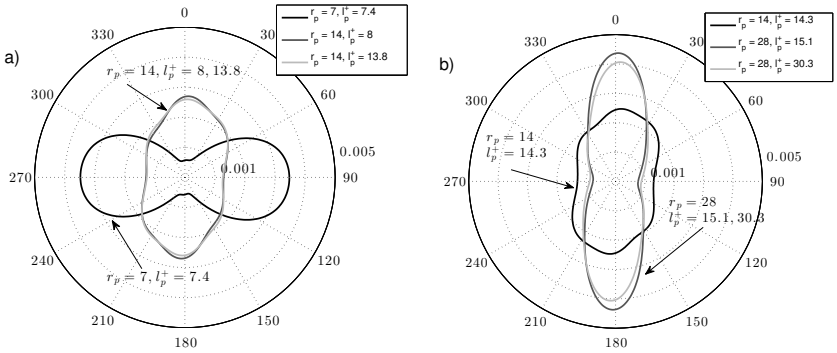

FIGURE 6. Fibre orientation distributions for (a) $r_p = 7, 14$ and (b) $r_p = 14, 28$ for different non-dimensional fibre lengths, l_p^+.

4. Results

The results will be presented in three groups: (i) orientation distributions in the plane parallel to the wall under different conditions, Figs. 6–8, (ii) anisotropy A as a function of different non-dimensional groups and the streamwise direction, Fig. 9, and (iii) streakiness[1], streak width and anisotropy inside and outside of streaks, Fig. 10. Most of the data is from a fibre suspension of pure water and fibres; two series of anisotropy data with PEO added to the water are shown in Fig. 9 (d).

4.1. *Orientation distributions*

Selected orientation distributions will be shown focusing on the importance of turbulent length scales, the effect of fibre aspect ratio and the effect of concentration. The orientation of the fibres are defined such that $\beta = 0$ is in the streamwise direction.

First, turbulent length scales and fibre aspect ratios will be addressed. In Fig. 6, r_p and l_p^+ are varied. In (a), $(r_p, l_p^+) = (7, 7.4)$, $(14, 8)$ and $(14, 13.8)$ are shown. At $r_p = 7$, the distribution shows a distinct orientation in the spanwise direction ($\beta = 90°$ and $270°$) whereas the $r_p = 14$ cases have a slight tendency to align in the streamwise direction ($\beta = 0°$ and $180°$). The distributions for $r_p = 14$ are almost identical but l_p^+ differs almost a factor of two. However, the distribution for $r_p = 7$ is clearly different, even though its l_p^+ is very close to one of the $r_p = 14$ distributions ($l_p^+ = 7.4$ and 8, respectively).

[1]The tendency for fibres to agglomerate into streaks

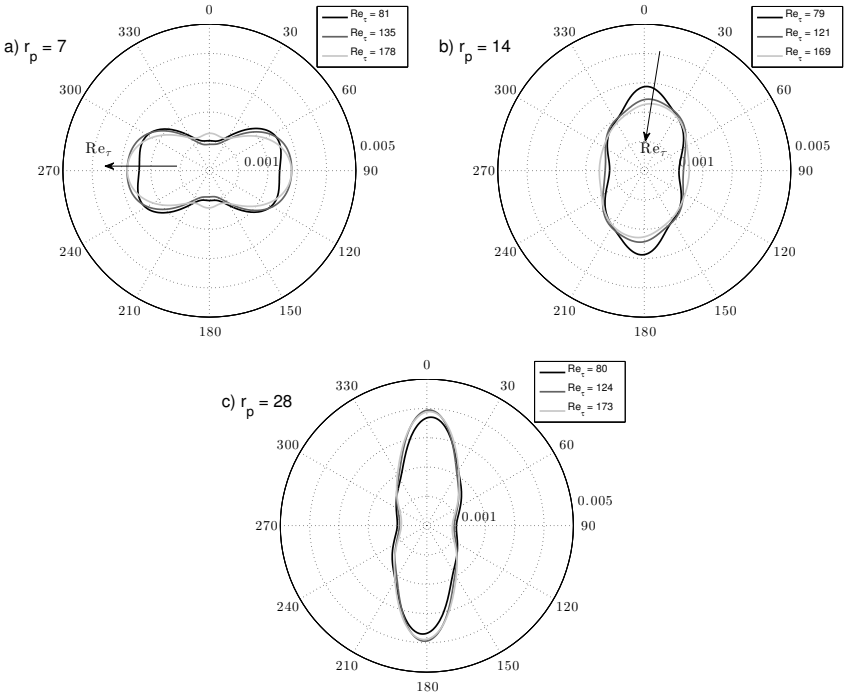

FIGURE 7. Fibre orientation distributions for (a) $r_p = 7$, (b) $r_p = 14$ and (c) $r_p = 28$, with similar friction Reynolds numbers for each aspect ratio.

Similarly in Fig. 6 (b), two orientation distributions for $r_p = 28$ ($l_p^+ = 15.1$ and 30.3) and one for $r_p = 14$, $l_p^+ = 14.4$ are shown. The variation of the non-dimensional fibre length result only in a slight difference between the orientation distributions while the aspect ratio once again has a large impact. The longer fibres ($r_p = 28$) are almost completely aligned in the streamwise direction whereas the shorter ones ($r_p = 14$) only show a weak tendency to do so.

In Fig. 7, fibre orientation distributions are shown for the three different aspect ratios from (a) to (c). For each aspect ratio, three friction Reynolds numbers are shown(the friction Reynolds numbers are similar for the three aspect ratios). As before, the fibres with $r_p = 7$ in (a) have a preferred orientation in the spanwise direction whereas the most slender fibres with $r_p = 28$ in (c) are aligned in the streamwise direction. At $r_p = 14$, (b), there is a small tendency for alignment in the streamwise direction. For each aspect ratio, variations of Re_τ produces only small changes that will be quantified in terms of anisotropy later.

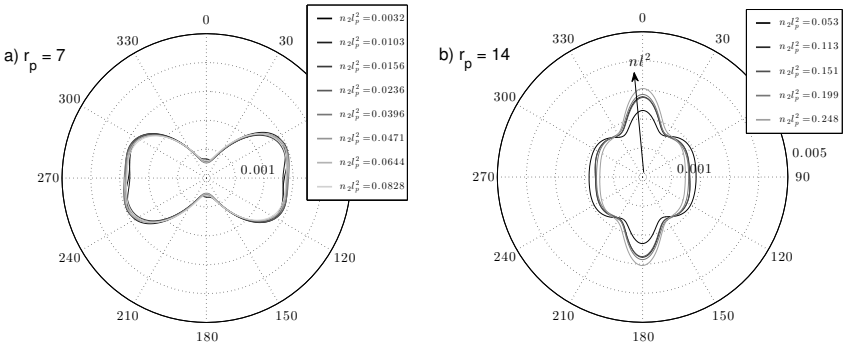

FIGURE 8. Fibre orientation distributions for (a) $r_p = 7$ and (b) $r_p = 14$, with varying concentrations and constant flow condition ($\mathrm{Re}_\tau = 110$).

The final orientation distributions focus on effects of fibre concentration. In Fig. 8, fibre orientation distributions for two aspect ratios, ($r_p = 7$, 14) and different local fibre concentrations, $n_2 l_p^2$ (actual values given in the legends) are shown. The results in these figures have all been obtained at the same flow conditions, at a friction Reynolds number of $\mathrm{Re}_\tau = 110$. For the shorter fibres, with $r_p = 7$, Fig. 8 (a), the changes in concentration have a very small effect. However, for the fibres with aspect ratio $r_p = 14$ in (b), an increase in concentration causes more fibres to orient in the flow direction.

4.2. *Fibre orientation anisotropy*

The fibre orientation anisotropy data is shown in Fig. 9. In Fig. 9(a), the anisotropy is shown as a function of the friction Reynolds number. The orientation anisotropy for $r_p = 28$ seems to be unaffected by the change in Re_τ, while the trend for $r_p = 7$ and 14 is an approach towards orientational isotropy ($A = 10^0$) as the friction Reynolds number is increased. For $r_p = 7$, 14 the concentration was varied at constant $\mathrm{Re}_\tau = 110$. For $r_p = 7$, all filled squares are at the same anisotropy but for $r_p = 14$, there is a change with concentration.

The concentration effects are detailed in Fig. 9(b) where the anisotropy is shown versus the local fibre concentration. A clear grouping of the different aspect ratios is visible, and inside each aspect ratio there is a distinct scatter, in particular for $r_p = 7$ and 14 due to the variation of Re_τ.

In addition to the experiments with water-fibre suspension, a few experiments were performed with a small amount (40 ppm) of Poly-Ethylene Oxide (PEO) added. The results from these experiments are shown in Fig. 9(c), where the filled markers are cases where the suspending fluid is the water-PEO mixture and the empty markers are the corresponding cases where pure water was used. For $r_p = 7$, no apparent change in anisotropy is visible compared

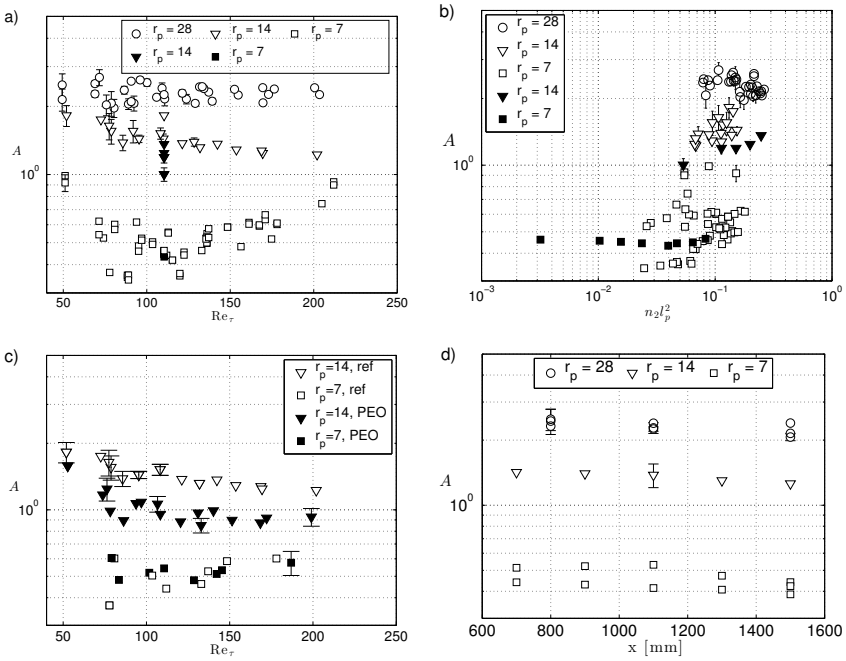

FIGURE 9. Fibre orientation anisotropy versus (a) friction Reynolds number, (b) local concentration and (d) streamwise position. In (a) and (b), the filled symbols (▼ and ■) are constant Re_τ and varying concentrations. In (c) the fibre orientation anisotropy is shown versus the friction Reynolds number for a suspension containing PEO (▼ and ■) and the reference case (▽ and □).

to the reference with pure tap water. However, for the fibres with aspect ratio $r_p = 14$, a consistent decrease in the anisotropy is seen for all experiments with the PEO solution.

It was also confirmed that the fibre orientation had enough time to converge when the fibres reached the position for the image acquisition. Images were captured at five streamwise positions between $x = 700$ and 1500 mm and the results from these measurements are shown in Fig. 9(d). The experiments were performed for different friction Reynolds numbers, ranging between $\mathrm{Re}_\tau = 100$–200 (two cases for $r_p = 7$, one for $r_p = 14$ and three for $r_p = 28$). Again, the different aspect ratios give different anisotropy and the change in the streamwise direction is very small.

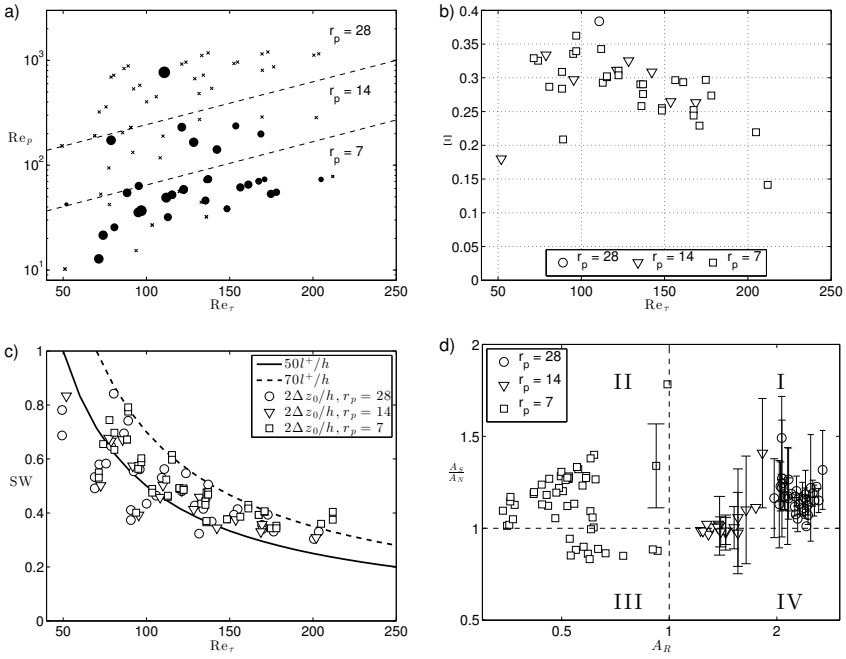

FIGURE 10. (a) Streakiness, larger dots represent a higher degree of streakiness; (×) represents measurements were streakiness data could not be determined due to insufficient or excessive fibre concentration. (b) Relative streakiness, Ξ, as function of Re_τ, higher value represents higher streakiness. (c) Fibre streak width (SW) versus Re_τ, the solid line is $SW = 50l^+/h$, the typical width of the low velocity streaks in a turbulent shear layer. (d) Fibre orientation anisotropy inside fibre streaks (A_S) relative to the anisotropy of fibres not located in fibre streaks (A_N) versus the total anisotropy (A_R).

4.3. *Fibre streaks*

In many of the experiments performed, the fibres were seen to accumulate into streamwise streaks. In Fig. 10(a), the relative streakiness Ξ is shown in the Re_p-Re_τ plane, where a larger dot represents a larger value of Ξ. The measurements marked with a cross (×) are cases where the analysis failed, either due to too low (streakiness analysis fails) or too high (fibre detection fails in the streaks and streak analysis would be incorrect) fibre concentration. Figure 10(b) shows that the streakiness decreases from $\mathrm{Re}_\tau = 110$ and up. The amount of data does not allow any other observations.

In Fig. 10(c), the width of the fibre streaks are compared to the typical width of low velocity streaks in turbulent boundary layers ($50l^+$), see *e.g.* Zacksenhouse *et al.* (2001). The scaling of the fibre streaks is of the same order as the low velocity streaks, although the fibre streaks are slightly wider. A widening of the low velocity streaks in particulate flows has been noted in DNS by Zhao *et al.* (2010) and Sardina *et al.* (2012) for spherical particles.

In order to discover differences in the fibre orientation inside streaks and elsewhere, the relative anisotropy of the orientation distribution inside (A_S) and outside (A_N) of the streaks is investigated. The parameters are found by considering the 10% most and least clustered fibres in each image, found by the Voronoi analysis. The relative anisotropy (A_S/A_N) is shown in Fig. 10(d) against the reference anisotropy (A_R), which is obtained by considering all fibres. The figure has been divided into four quadrants, data in quadrants I and III indicate a preferred orientation inside the streaks (in the flow direction in I and normal to the flow in III) as compared to the fibres outside of the streaks. The opposite is true for the quadrants II and IV, where the orientation is more isotropic inside the streaks in relation to the fibres outside. Unfortunately, the data is inconclusive. The data for $r_p = 7$ has converged to the size of the marker, but appear in both quadrant II and III. The data for $r_p = 14$, 28 has to large errors to make any conclusions.

5. Discussion

The results reveal a major impact of fibre aspect ratio on the orientation of the fibres as they have sedimented to the wall region. In comparison with the major impact of fibre aspect ratio, effects of friction Reynolds number, concentration and addition of 40 ppm PEO are of secondary importance. The additional factors only modify the fibre orientation slightly. The orientation behaviour is such that fibres with aspect ratio $r_p = 7$ are oriented normal to the flow direction whereas fibres with $r_p = 28$ are oriented in the flow direction. The intermediate fibres ($r_p = 14$) give more isotropic orientation distributions.

This orientation behaviour is similar to the one observed in experiments on fibre orientation in laminar flow by Carlsson *et al.* (2007); Carlsson (2009). In the laminar case, a combined theoretical/numerical study showed that the difference in orientation behaviour between short and long fibres occurred due to a competition between the effects of sedimentation towards the wall and wall interactions (driving the fibres towards an orientation normal to the flow) and the effects of fluid inertia (when leaving the Stokes flow limit) counteracting this tendency.

In the present work, two additional factors appear compared to the laminar case. The first is turbulent velocity fluctuations and the second is potentially strong particle and fluid inertia due to the high Re_p. The data presented here demonstrates that the length scale of the turbulent velocity fluctuations has a weaker impact than r_p (Fig. 6). Regarding particle and fluid inertia,

Fig. 5(a) shows that the effect of aspect ratio is larger than the effect of particle Reynolds number. The present effects of aspect ratio at $10 < \mathrm{Re}_p < 1500$ are nearly identical to those observed at $\mathrm{Re}_p \approx 0.01$ in laminar flow Carlsson *et al.* (2007); Carlsson (2009).

A theoretical analysis Carlsson (2009) showed that the behaviour at low Reynolds number occurred due to a competition between wall interaction effects and inertial effects. It could be hypothesized that similar effects are at hand in the present experiments. This means that the mean shear, together with hydrodynamic and direct interactions with the wall, control the fibre orientation. The exact nature of these mechanisms should be investigated in detailed single particle simulations.

When it comes to particle hydrodynamics including particle inertia, a complete description is not yet available. Nevertheless, simulations of ellipsoids (aspect ratio 2) shows that buoyant particles undergo a number of transitions as Re_p is increased (Yu *et al.* 2007; Huang *et al.* 2012; Rosén *et al.* 2014). At low nonzero Re_p, a particle drifts to alignment with the vorticity axis ($\beta = 90°$ in the present case). As Re_p increases, the angle between the particle to the vorticity axis increases and the particle starts to nutate. Eventually, the particle will be steady and aligned with the flow direction. The details of the transitions between these rotational states depend on Re_p, r_p and the particle/fluid density ratio (for high density ratios Lundell & Carlsson (2010) particle inertia will cause the particles to align with the flow direction also at $\mathrm{Re}_p = 0$). The trend in the present study: alignment with the vorticity axis at low Re_p and with the flow direction at larger Re_p is in agreement with the trends observed for a single particle at aspect ratios up to 4 (Yu *et al.* 2007; Huang *et al.* 2012; Rosén *et al.* 2014). It is clear that a detailed description of rotational states in the full parameter space (Re_p, r_p and density ratio) is necessary in order to understand our observations. However, such a description is not yet at hand for the aspect ratios of this study.

It is now time to discuss the nature of the direct wall interactions. It has been shown by Jeffery (1922) that fibres in shear at zero Re_p perform a tumbling motion when aligned in the flow direction (due to the acceleration prior to the test section, this is the dominating orientation of the fibres far from the wall). As the fibres approach the wall, they interact with the wall first hydrodynamically (since the presence of the wall changes the flow around the fibre as it sediments in the shear) and by direct contact.

A first estimate of the number of direct wall interactions is given by the inverse of the sedimentation parameter S. From Fig. 5(c), it can be argued that (i) the different fibre lengths do not touch the wall in a distinctively different manner and (ii) the number of direct wall interactions is very limited. The observations in this paper must therefore be explained with either a combination

of particle hydrodynamics and direct contact with the wall or particle hydrodynamics alone. Repeated wall contact can be ruled out as an explanation to the differences in orientation.

Thus, the present results indicate that the orientation of the fibres is governed by mean shear and wall interactions, even though the turbulence have a clear impact on organizing the fibres into streaks. This supports the idea that the fibre orientation in the parameter region under study can be modelled without explicit consideration of the instantaneous turbulent vortices or the finite fibre size. This gives hope for both Lagrangian point-particle approaches and Eulerian modelling of the orientation distribution. However, modelling of the particle distribution and organisation into streaks could be more challenging.

The streakiness data showed a clear decrease in streakiness from $\mathrm{Re}_\tau = 110$ and up. Since no streaks are expected to occur in a laminar flow (low Re_τ), there must be a maximum in streakiness and this maximum occurs for $\mathrm{Re}_\tau < 110$

Finally, a short note will be made on rotational diffusivity. The only distinct effect of concentration was an *increase* in anisotropy with increasing concentration for the fibres with $r_p = 14$ (see Fig. 9(b)), showing that the fibre interactions at high concentrations cannot be modelled as a diffusion acting on the orientation distribution.

6. Conclusions

Orientation and distribution of fibres in turbulent flow in the neighbourhood of a solid wall has been studied. The flow regime studied is $50 < \mathrm{Re}_\tau < 210$. The main conclusions are

- The fibre orientation is controlled by the fibre aspect ratio. Turbulent length scales, friction Reynolds number and concentration is of secondary importance.
- The fibres are oriented normal to the flow for $r_p = 7$ and aligned with the flow for $r_p = 28$. The intermediate fibres ($r_p = 14$), displayed more isotropic orientation distributions.
- A polymer (PEO) concentration of 40 ppm made the orientation distributions of the intermediate fibres ($r_p = 14$) more isotropic. The shorter fibres ($r_p = 7$) were not affected.
- The fibres organize themselves in streaks. The streakiness vary with Reynolds number and there is a maximum for some $\mathrm{Re}_\tau < 110$.
- For the intermediate fibres ($r_p = 14$), the anisotropy of the orientation distributions increased with increasing concentration, while it stayed constant for the shorter fibres ($r_p = 7$). This indicates that fibre interactions in the particle clusters cannot be modelled as an increase in rotational diffusivity.

Thanks to Dr. Allan Carlsson for providing valuable input during the experiment and analysis. The Knut and Alice Wallenberg Foundation, through the Wallenberg Wood Science Center, funded this work. Dr. Lundell and Dr. Prahl Wittberg have also been funded by the Swedish Research Council, VR.

References

Acheson, D. J. 1995 *Elementary Fluid Dynamics*. Oxford University Press.

Advani, S. G. & Tucker III, C. L. 1987 The use of tensors to describe and predict fiber orientation in short fiber composites. *J. Rheol.* **31** (8), 751–784.

Aidun, C. K., Lu, Y. & Ding, E. 1998 Direct analysis of particulate suspensions with inertia using the discrete Boltzmann equation. *J. Fluid Mech.* **373**, 287–311.

Andersson, H. I., Zhao, L. & Barri, M. 2012 Torque-coupling and particle-turbulence interactions. *J. Fluid Mech.* **696**, 319–329.

Aurenhammer, F. 1991 Voronoi diagrams - a survey of a fundamental geometric data structure. *ACM Comput Surv.* **23**, 345–405.

Batchelor, G. K. 1970 Slender-body theory for particles of arbitrary cross-section in Stokes flow. *J. Fluid Mech.* **44** (03), 419–440.

Bellani, G., Byron, M. L., Collignon, A. G., Meyer, C. R. & Variano, E. A. 2012 Shape effects on turbulent modulation by large nearly neutrally buoyant particles. *J. Fluid Mech.* **712**, 41–60.

Buckingham, E. 1914 On physically similar systems; illustrations of the use of dimensional equations. *Phys. Rev.* **4**, 345–376.

Carlsson, A. 2009 Near wall fibre orientation in flowing suspensions. PhD thesis, KTH Mechanics, Royal Institute of Technology.

Carlsson, A., Håkansson, K., Kvick, M., Lundell, F. & Söderberg, L. D. 2011 Evaluation of steerable filter for detection of fibers in flowing suspensions. *Exp. Fluids* **51**, 987–996.

Carlsson, A., Lundell, F. & Söderberg, L. D. 2007 Fiber orientation control related to papermaking. *J. Fluids Eng.* **129** (4), 457–465.

Do-Quang, M., Amberg, G., Brethouwer, G. & Johansson, A. V. 2014 Simulation of finite-size fibers in turbulent channel flows. *Phys. Rev. E* **89**, 013006.

Einarsson, J., Angilella, J. & Mehlig, B. 2014 Orientational dynamics of weakly inertial axisymmetric particles in steady viscous flows. *Physica D* **278–279** (0), 79–85.

Gustavsson, K. & Tornberg, A.-K. 2009 Gravity induced sedimentation of slender fibers. *Phys. Fluids* **21** (12).

Håkansson, K. M. O., Kvick, M., Lundell, F., Prahl Wittberg, L. &

Söderberg, L. D. 2013 Measurement of width and intensity of particle streaks in turbulent flows. *Exp. Fluids* **54** (6), 1555.

Harris, J. B. & Pittman, J. F. T. 1975 Equivalent ellipsoidal axis ratios of slender rod-like particles. *J. Colloid. Interf. Sci.* **50** (2), 280 – 282.

Herzhaft, B. & Guazzelli, E. 1999 Experimental study of the sedimentation of dilute and semi-dilute suspensions of fibres. *J. Fluid Mech.* **384**, 133–158.

Holm, R. & Söderberg, D. 2007 Shear influence on fibre orientation. *Rheol. Acta.* **46**, 721–729.

Huang, H., Yang, X., Krafczyk, M. & Lu, X.-Y. 2012 Rotation of spheroidal particles in couette flows. *J. Fluid Mech.* **692**, 369–394.

Jacob, M. & Unser, M. 2004 Design of steerable filters for feature detection using canny-like criteria. *IEEE Trans. Pattern Anal. Mach. Intell.* **26** (8), 1007–1019.

Jadoon, A. & Revstedt, J. 2010 Large eddy simulation of particle laden jet flow with aerodynamic three-way coupling. In *WIT Transactions on Engineering Sciences*, , vol. 69, pp. 219–229.

Jeffery, G. B. 1922 The motion of ellipsoidal particles immersed in a viscous fluid. *P. Roy. Soc. A* **102** (715), 161–179.

Kim, J., Moin, P. & Moser, R. 1987 Turbulence statistics in fully developed channel flow at low reynolds number. *J. Fluid Mech.* **177**, 133–166.

Koch, D. L. & Shaqfeh, E. S. G. 1989 The instability of a dispersion of sedimenting spheroids. *J. Fluid Mech.* **209**, 521–542.

Lundell, F. & Carlsson, A. 2010 Heavy ellipsoids in creeping shear flow: Transitions of the particle rotation rate and orbit shape. *Phys. Rev. E* **81**, 016323.

Marchioli, C., Fantoni, M. & Soldati, A. 2010 Orientation, distribution, and deposition of elongated, inertial fibers in turbulent channel flow. *Phys. Fluids* **22** (3), 033301.

Mortensen, P., Andersson, H., Gillissen, J. & Boersma, B. 2008 On the orientation of ellipsoidal particles in a turbulent shear flow. *Int. J. Multiphase Flow* **34** (7), 678–683.

Parsa, S., Calzavarini, E., Toschi, F. & Voth, G. A. 2012 Rotation rate of rods in turbulent fluid flow. *Phys. Rev. Lett* **109**, 134501.

Qi, D. & Luo, L. 2002 Transitions in rotations of a nonspherical particle in a three-dimensional moderate Reynolds number couette flow. *Phys. Fluids* **14** (12), 4440–4443.

Rosén, T., Aidun, C. & Lundell, F. 2013 The combined effect from fluid and particle inertia on the dynamical states of a prolate spheroidal particle suspended in shear flow. *J. Fluid Mech.* Under review.

Rosén, T., Aidun, C. & Lundell, F. 2014 Effect of fluid inertia on the dynamics and scaling of neutrally buoyant particles in shear flow. *J. Fluid Mech.* **738**, 563–590.

Saintillan, D., Darve, E. & Shaqfeh, E. S. G. 2005 A smooth particle-mesh ewald algorithm for stokes suspension simulations: The sedimentation of fibers. *Phys. Fluids* **17** (3).

Sardina, G., Schlatter, P., Brandt, L., Picano, F. & Casciola, C. M. 2012

Wall accumulation and spatial localization in particle-laden wall flows. *J. Fluid Mech.* **699**, 50–78.

Stokes, G. G. 1856 On the effect of the internal friction of fluids on the motion of pendulums. *Trans. Cambridge Philos. Soc.* **9** (3), 8–106.

Stover, C. & Cohen, C. 1990 The motion of rodlike particles in the pressure-driven flow between two flat plates. *Rheol. Acta* **29** (3), 192–203.

Subramanian, G. & Koch, D. 2006 Inertial effects on the orientation of nearly spherical particles in simple shear flow. *J. Fluid Mech.* **557**, 257–296.

Tsukahara, T., Seki, Y., Kawamura, H. & Tochio, D. 2005 DNS of turbulent channel flow at very low Reynolds numbers. In *Proc. of the Fourth Int. Symp. on Turbulence and Shear Flow Phenomena*, pp. 935–940.

van Wachem, B., Zastawny, M., Mallouppas, G. & Zhao, F. 2013 Modelling of gas-solid turbulent flows with non-spherical particles. In *8^{th} International Conference on Multiphase Flow*.

Yu, Z., Phan-Thien, N. & Tanner, R. I. 2007 Rotation of a spheroid in a Couette flow at moderate Reynolds numbers. *Phys. Rev. E* **76**, 026310.

Zacksenhouse, M., Abramovich, G. & Hetsroni, G. 2001 Automatic spatial characterization of low-speed streaks from thermal images. *Exp. Fluids* **31** (2), 229–239.

Zhang, F., Dahlkild, A. A. & Lundell, F. 2013 Nonlinear disturbance growth during sedimentation in dilute fibre suspensions. *J. Fluid Mech.* **719**, 268–294.

Zhang, H., Ahmadi, G., Fan, F.-G. & McLaughlin, J. B. 2001 Ellipsoidal particles transport and deposition in turbulent channel flows. *Int. J. Multiphase Flow* **27** (6), 971–1009.

Zhao, L. H., Andersson, H. I. & Gillissen, J. J. J. 2010 Turbulence modulation and drag reduction by spherical particles. *Phys. Fluids* **22** (8), 081702.

2

Paper 2

Measurement of width and streakiness of particle streaks in turbulent flows

By Karl Håkansson, Mathias Kvick, Fredrik Lundell, Lisa Prahl Wittberg & L. Daniel Söderberg

Wallenberg Wood Science Center & Linné Flow Centre, KTH Mechanics, Royal Institute of Technology, SE – 100 44 Stockholm, Sweden

With kind permission from Springer Science+Business Media.
Published in *Exp. Fluids* **54**, 1555, 2013

Fibre streaks are observed in experiments with fibre suspensions in a turbulent half channel flow. The preferential-concentration methods, most commonly used to quantify preferential particle concentration, are in one dimension found to be concentration dependent.

Two different new streak quantification methods are evaluated, one based on Voronoi analysis and the other based on artificial particles with an assigned fixed width. The width of the particle streaks, and a measure of the intensity of the streaks, *i.e.* streakiness, are sought. Both methods are based on the auto-correlation of a signal, generated by summing images in the direction of the streaks. Common for both methods is a severe concentration dependency, verified in experiments keeping the flow conditions constant while the (very dilute) concentration of fibres is altered.

The fixed width method is shown to be the most suitable method, being more robust and less computationally expensive. By assuming the concentration dependence to be related to random noise, an expression is derived, which is shown to make the streak width and the streakiness independent of the concentration even at as low concentrations as 0.05 particles per pixel column in an image. The streakiness is obtained by applying an artificial particle width equal to 20% of the streak width. This artificial particle width is in this study found to be large enough to smoothen the correlation without altering the streakiness nor the streak width. It is concluded that in order to make quantitative comparisons between different experiments or simulations, the evaluation has to be performed with care and be very well documented.

---

1. Introduction

When introducing particles into a turbulent wall bound-ed flow, it is well known that the particles tend to agglomerate into streamwise streaks close to the walls.

This has been found both in experiments, *e.g.* (Rashidi *et al.* 1990; Fessler *et al.* 1994; Kulick *et al.* 1994; Kaftori *et al.* 1995*a*,*b*; Ninõ & Garcia 1996), and in simulations, *e.g.* (Pedinotti *et al.* 1992; Rouson & Eaton 2001; Narayanan *et al.* 2003; Marchioli *et al.* 2010).

In many industry processes, *e.g.* paper making, particle suspensions are pumped and transported through different geometries at high speeds, resulting in turbulent wall bounded flows. In order to understand how the particles are influenced by the turbulent flow, it is important to obtain a quantitative measure of the strength of the tendency for the particles to agglomerate into streaks. This is also necessary if different experiments and simulations are to be compared.

Even though several methods exist to investigate clustering, these methods are not able to provide information whether particles form streaks or not.

Fessler *et al.* (1994) introduced the parameter D, quantifying 2-dimensional preferential concentration, defined by comparing the measured particle density to a random distribution:

$$D = \frac{\sigma - \sigma_p}{\lambda} \tag{1}$$

where σ is the standard deviation of the measured particle density, σ_p is the standard deviation of a random Poisson distribution and λ is the mean particle density. D becomes positive if clusters and voids are present, negative if the particle distribution is homogeneous and zero if the particles are randomly distributed. The parameter D is dependent of the box size, and by finding the box size that maximizes D, the typical cluster size can be found.

A more recent preferential concentration quantification method, based on Voronoi analysis, was proposed by Monchaux *et al.* (2010). In a Voronoi analysis, each particle is assigned a cell with an area inversely proportional to the local concentration. Comparing measured cell areas to a Poisson distribution provides the location and character of clusters.

The preferential concentration parameter, D, will be shown to be concentration dependent and thus failing to provide a consistent measure of the typical cluster size. The Voronoi analysis method displays a similar behavior. Therefore, in order to characterize the 1-dimensional streaks, more information is needed, emphasizing the need of a new method.

In this article, correlations in the spanwise direction, normal to the streaks, will be used to determine (i) a streak width and (ii) an objective quantification of the qualitative term "streakiness" (tendency to agglomerate in streaks). This correlation will be obtained in two ways, both of which make use of the position of individual particles in an image. The first is based on a Voronoi analysis; the second is a straightforward correlation similar to a sum of image intensities. The second method is determined to be most suitable. As a result a scheme to determine the streak width and the streakiness independent of particle size,

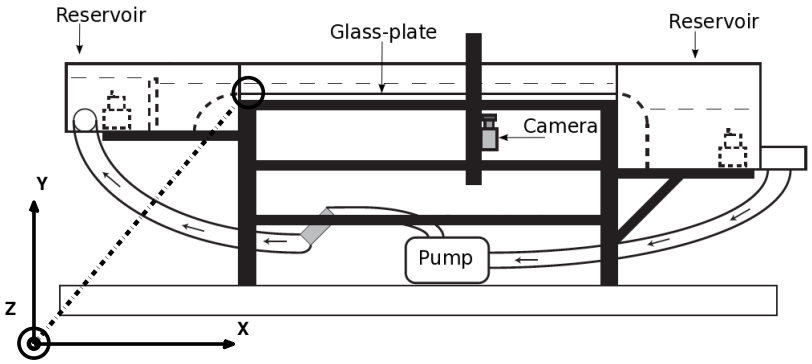

FIGURE 1. Schematic of the flow apparatus

orientation, concentration, image size and streak width is obtained, including a consistent way of setting the single input parameter. The dependence of:

- particle size and orientation is treated by identifying the center of gravity of the particles in the images.
- concentration effects on the correlation is treated using the correlation from an image with randomly placed particles.
- image size is treated by considering the finite length of the input signal into the correlation.
- streak width is treated by normalizing the input parameter with the streak width (iterations are needed).

2. Flow apparatus

Images of a fibre suspension in a turbulent half channel flow have been acquired. Fig. 1 depicts the flow apparatus where the suspension is pumped from a downstream to an upstream reservoir, allowing the suspension to flow down an inclined glass plate. A camera is mounted underneath the glass plate acquiring images of the fibres in the flow. A typical image is shown in Fig. 2a and a close up of the upper left corner is displayed in 2b, showing clearly that fibres form streaks and the individual fibres, respectively. Pumps are placed in the upstream and downstream reservoirs in order to stir the suspension, and prevent fibres from sedimenting in the reservoirs. The coordinate system is defined so that the x-axis correspond to the streamwise direction, the y-axis is in the wall normal direction and the z-axis is in the spanwise direction. The origin is positioned on the leading edge of the glass plate with $z = 0$ on its centreline.

Velocity profiles of the flow were measured with Laser Doppler Velocimetry (LDV) at the acquisition point, upstream of the acquisition point and also at

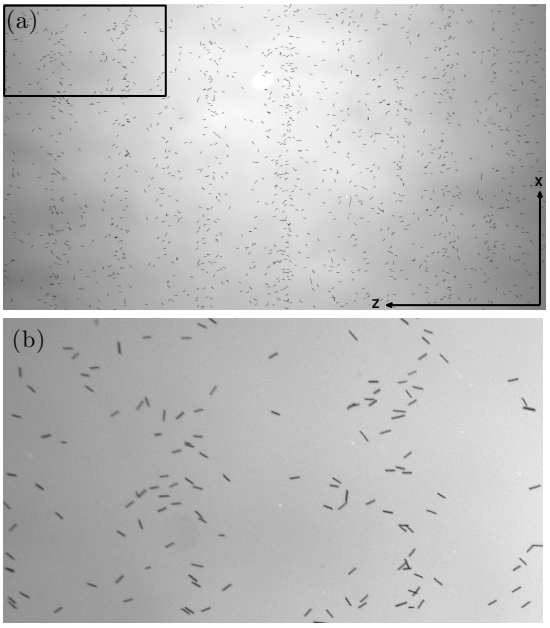

FIGURE 2. Example of an image from a turbulent fibre suspension flow with clear fibre streaks (a). The fibres are black, the differences in intensity are mostly due to the focusing of the light source, the flow is from bottom to top. A close up of the marked area in (a) is shown in (b)

two spanwise positions. The velocity profiles showed good agreement with DNS data for a full channel and the flow was confirmed to be turbulent and fully developed. More details regarding the setup and the LDV measurements can be found in Kvick *et al.* (2012), where the same setup was used.

Since the flow is driven by gravity alone, the wall shear stress, τ_w, can be calculated through the force balance at the wall;

$$\tau_w = \rho g h \sin\alpha. \tag{2}$$

Here ρ represents the density of the fluid, g is the gravitational acceleration, h is the height of the water layer on the glass plate and α is the inclination angle of the plate. The friction Reynolds number is defined as;

$$Re_\tau = \frac{hu_\tau}{\nu} = \frac{h\sqrt{gh\sin\alpha}}{\nu}, \tag{3}$$

where $u_\tau = \sqrt{\tau_w/\rho}$ and ν represent the friction velocity and the kinematic viscosity, respectively.

The suspension consists of water and cellulose acetate fibres with density 1300 kg/m^3 and concentrations $nl^3 = 0.0007 - 0.006$, where n is the number density and l is the fibre length. For each case, 150 statistically independent images (1920×1080 pixels) are acquired, *i.e.* all fibres are transported out of the field of view of the camera before the next image is taken.

The positions of the fibres in the images are obtained by the use of a steerable filter, described in Carlsson *et al.* (2011). Using this filter, it is possible to detect both fibre positions and orientations in the flow-vorticity plane. The filter can even detect crossed fibres to a certain amount. Several layers of fibres or fibres covering most of the image can not be identified by this filter. This is one of the reasons why the experiment has to be performed at low concentrations of fibres in the suspension. With index of refraction matching methods (where a only a fraction of the actual particles are visible), higher particle concentrations can be reached. However, the concentration of visible particles would still be limited, since the detection is dependent of the resolution of the camera and the size of the particles.

To evaluate the different analysis methods, the experiments are performed using constant Re_τ and aspect ratio, but different fibre concentrations. This is referred to as physical concentration in this study. An artificial concentration variation is also used, by detecting and identifying all fibres in the images, and randomly excluding fibres during post processing. If the streaks are assumed to be the result of a flow driven clustering process, aspects such as streakiness and streak width will be independent of concentration. Consequently, streakiness and streak width must not vary if fibres are randomly removed.

Firstly, five experiments at $Re_\tau = 110$, with fibres of aspect ratio $r_p = 7$ and varying fibre concentration will be considered. The particle (fibre) concentration, c, are measured in particles (fibres) per column of pixels in the image. The specifications for the five cases are displayed in table C.3. Case 3, where clear streaks are observed, will be used as an example to illustrate differences in the two new analysis methods. Thereafter quantitative results from five other cases ($\mathrm{Re}_\tau = 51 - 178$) will be shown in order to highlight differences in streakiness. Finally the experiments with different concentration will be considered.

3. Existing preferential concentration methods

3.1. *Preferential concentration parameter, D*

The preferential concentration parameter, D, defined in Eq. 1, is in this 1-dimensional case calculated using columns of pixels in the direction of the streaks instead of boxes. The width of the columns are varied and the resulting values of D are displayed in Fig. 3. Fig. 3 shows cases 1-5 where only the concentration has been varied, $0.12 < c < 0.97$ particles per column. It can be concluded that D is concentration dependent, and the jagged appearance of

TABLE C.3. Table of experiments with different concentration of fibres.

Case	Re_τ	r_p	c	Physical conc.	Artificial conc.
1	110	7	0.12	●	○
2	110	7	0.46	■	□
3	110	7	0.55	◀	◁
4	110	7	0.75	▶	▷
5	110	7	0.97	▼	▽

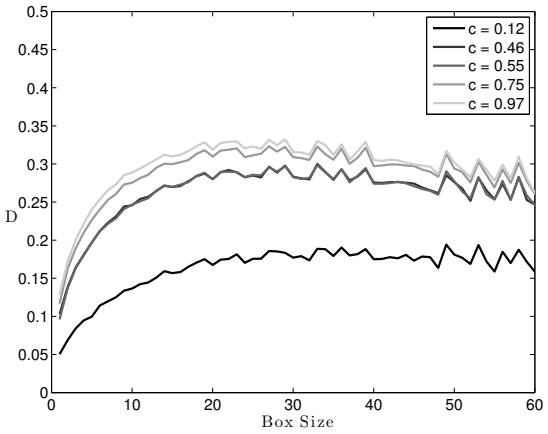

FIGURE 3. The preferential concentration parameter, D, versus box size in pixels

the curves makes it difficult to determine what a typical streak size would be. In this kind of flow the streaks are expected to appear at random streamwise positions, but having a similar size (width), as the case for low and high velocity streaks in e.g. Lagraa *et al.* (2004).

3.2. *Voronoi analysis in 1D*

A newly introduced method for measuring preferential concentration in 2 and 3 dimensions is based on Voronoi tessellation and results in a measure of the clustering and a measure of the cluster size, see *e.g.* Monchaux *et al.* (2010); Tagawa *et al.* (2012). By locating particles and determining the distance to the closest neighbors it is possible to determine if particles are located in clusters or not. A cluster is a region where the local particle density is high.

The streaks observed in the above described experiments are 1-dimensional structures. When the particles are identified, their positions can be projected on the z-axis and the centre points right in between neighbouring particles

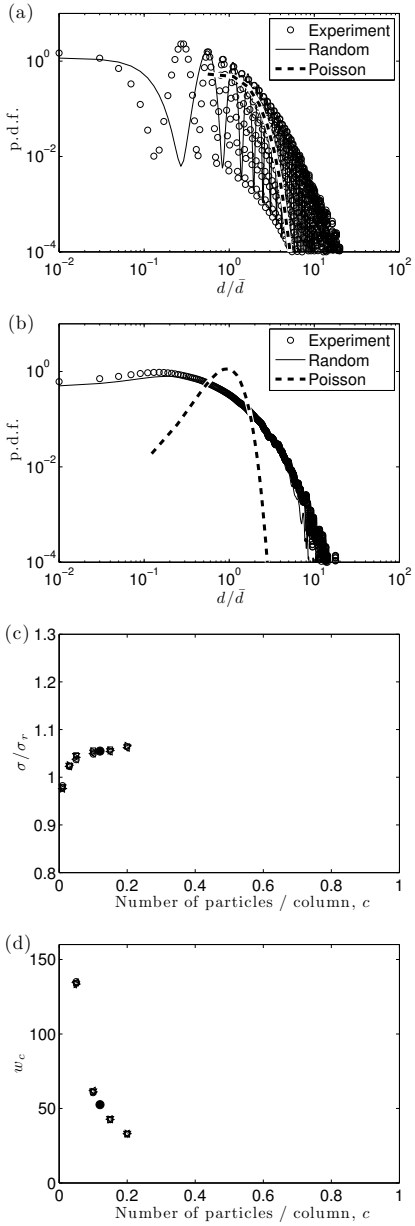

FIGURE 4. Probability density functions (p.d.f.) for normalized distances between particles, $d/\bar{d}$, at $c = 0.55$ and $c = 0.12$ in (a) and (b), respectively. The mean cluster width, w_c, is displayed in (c), and the normalized standard deviation, σ/σ_r, of the p.d.f. of d is shown in (d). The symbols in (c) and (d) are defined in table C.3

can be determined. A distance, d, can then be assigned to each particle as the distance between its nearest centre point. These distances are the 1D equivalent, to the Voronoi areas in 2D. Probability density functions (p.d.f.) of distances between particles, d, at $\mathrm{Re}_\tau = 110$ and concentrations $c = 0.55$ and $c = 0.12$ are displayed in Fig. 4a and Fig. 4b, where the distributions are normalized by the mean distance, $\bar{d}$. The distribution of a random Poisson process is also plotted in Fig. 4a-b (dashed line) as well as the distribution for randomly placed particles at the same concentration as the experiment (solid line). The Poisson distribution is used to determine wether the particles are in clusters or not. The randomly placed particles are used to quantify clustering. At the particle density of $c = 0.55$, the resolution of the images is too low. Hence, the distance $d = 0$ is dominating and the distribution seen in Fig. 4a, consist only of the jagged tail. The highest concentration for which the distributions are smooth, is for this experimental setup determined to be $c = 0.2$.

The only experimental case with the concentration lower than $c = 0.2$ is the lowest concentration case $c = 0.12$. However, by artificially removing particles from images, lower concentrations can be reached and thus the analysis can be performed for all cases with removed particles.

The first measure from the analysis is a measure of preferential concentration. Monchaux *et al.* (2010); Tagawa *et al.* (2012), proposed that the standard deviation of the measured distribution, σ should be compared to the standard deviation a random distribution, σ_r. A higher ratio of σ/σ_r is interpreted as a higher preferential concentration, it was noted by Tagawa *et al.* (2012) that this measure was dependent on number of particles. The 1-dimensional results are shown in Fig. 4c, and also here a dependency of number of particles is observed.

The second result from the Voronoi analysis is the mean cluster width, w_c, (area in the 2-dimensional case), introduced by Monchaux *et al.* (2010). The cluster width, w_c, is determined by collecting all connected particles classified as clustered and calculating the width of that cluster. The mean of the resulting cluster width distribution is seen in Fig. 4d.

Due to the concentration dependency of both the preferential parameter, D, discussed in the previous section, and the Voronoi based measures, an improvement of either method must be performed, or a new approach needs to be developed. The latter is pursued in this study.

4. New methods

4.1. *Correlation based analysis*

The analysis methods presented in this paper are based on auto-correlating a signal obtained from an image, and use the correlation curves to quantify the streaks. The signal with zero mean is denoted I and the auto-correlation of

the signal, R_{II}, is defined as:

$$\hat{R}_{II}(\Delta z) = \int I(z + \Delta z) I(z) dz, \quad R_{II} = \frac{\hat{R}_{II}}{\max \hat{R}_{II}}. \tag{4}$$

The symbols $\hat{R}$ and R are always used to denote the raw and normalised autocorrelation, respectively. The indices will vary. The signal used in the correlations are obtained in different manners by the two different new methods. However, the basic idea is the same: summing intensities in the direction along the streaks. For this idea to be valid, the particle streaks should be oriented in the summation direction (streamwise in this case) and the image needs to cover a sufficient region in the direction of the streaks, in order for the streaks to be detected. A straightforward way of obtaining the signal is to sum the intensities of the raw images in the streaky direction. This is similar to standard investigations of high and low velocity streaks in turbulent or transitional boundary layers, see *e.g.* Lagraa *et al.* (2004) or Fransson & Alfredsson (2003). In this way, information regarding the sizes and strengths of the velocity structures can be extracted fairly easy. The most important difference from the velocity investigation is that the velocities can be sampled in time until the signal have converged, while in the present case the signal is limited by the number of particles in one image.

However, using raw images as input into the analysis, several problems arises. One is the effect of differences in light intensities in the image. Another important aspect is the influence of the particle orientation in case of non-spherical particles. The signal will have a very different appearance depending on if the particles are oriented in the summing direction or perpendicular to it. To be able to assess these problems, it is necessary to use only the particle positions, and thereby reducing the number of non-controllable parameters.

The position and orientation of each particle are found in a first post processing step as mentioned earlier. With the positions known, the control over the input into the analysis is very high and comparable to the data from Lagrangian simulations.

4.2. *Correlations based on Voronoi analysis*

In order to obtain an analysis method independent of particle width and orientation, a Voronoi tessellation is applied to the particle positions. In a Voronoi diagram, the image is divided into an unstructured grid with one particle in each cell. The size and shape of each cell is determined by the surrounding particles. Particles located in regions with high local concentration has small cell areas and particles in regions were the concentration is lower has larger cell areas.

Thresholding the distribution of cell areas makes it possible to control the cells that are to be regarded as clustered and located in streaks, corresponding

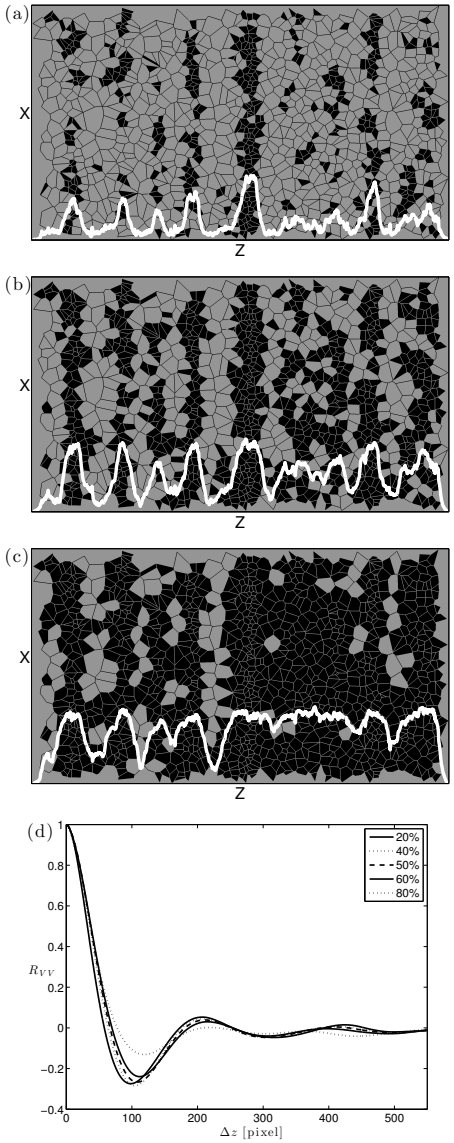

FIGURE 5. Voronoi map of the image in Fig. 2 with threshold (a) 20%, (b) 50% and (c) 80%, considered clustered with a high local density and here colored black, the resulting signal for each image is colored white. (d) R_{VV} for the complete set. The percentages in the legend corresponds to the part of the images considered to belong to streaky regions, and therefore contributing to the signal

to small areas. Assigning a value, *e.g.* 1, to the small areas and summing the image in the streamwise direction results in a signal that can be auto-correlated.

Fig. 5a–5c shows different thresholds for a Voronoi diagram based on Fig. 2, together with the resulting signals. In Figs. 5a–5c, 20%, 50% and 80% of the total image area is regarded as clustered cells, respectively. The clustered cells are colored black (value 1), and a summation of the images in the streaky direction (vertical) results in the signals displayed in white.

The signals are auto-correlated and the mean of the auto-correlations for all 150 images in the measurement set is displayed in Fig. 5d. The Voronoi based correlations, denoted R_{VV}, vary for different thresholds but display a lowest minimum for a threshold close to 50%. 50% is used as the threshold value in the rest of this paper. There are other options to threshold, for example, using the deviation of a random distribution of cell areas as the threshold, see *e.g.* Monchaux *et al.* (2010). Due to the low concentrations used in the present study, this threshold was inconsistent. The important thing to note is that a threshold needs to be chosen, and to find another criterion is out of the scope of this paper. Another constant percentage, for example 40% or 60% could have been chosen but will show a similar concentration dependence as shown below.

4.3. *Correlations based on a fixed width*

The second method uses the positions of the physical particles to construct images with artificial particles.

In order to smoothen the signal, the width, w, of the artificial particles is fixed to a value larger than one pixel. In Fig. 6a - 6c, three choices of particle widths are shown, based on the image in Fig 2. The sums of these artificial images are shown in black and, as is evident, the particle width influences the signal. Furthermore, as can be seen in Fig. 6d showing the correlation R_{ff} for the different particle widths, the choice of particle width plays an important role for the resulting correlation and must not be greater than the streak width. A particle width larger than the streak width results in that the small peaks are filtered out. In Fig. 6d it is noted that the correlations first zero crossing does not change significantly until the particle fixed width exceeds 41 pixels.

4.4. *Determination of streak width,* $2\Delta z(R_{II} = 0)$*, and streakiness,* $\Xi(R_{II})$*, from correlations*

The streak width is in this study determined as the displacement at which the minimum correlation occurs. However, this point is never well defined. Therefore the first zero-crossing, that can be interpolated, is taken as the streak half width, $\Delta z(R_{II} = 0)$, where $R_{II} = 0$ implies the first position at which the correlation is zero. The same approach was used for velocity streaks by Fransson & Alfredsson (2003) and shown to be consistent.

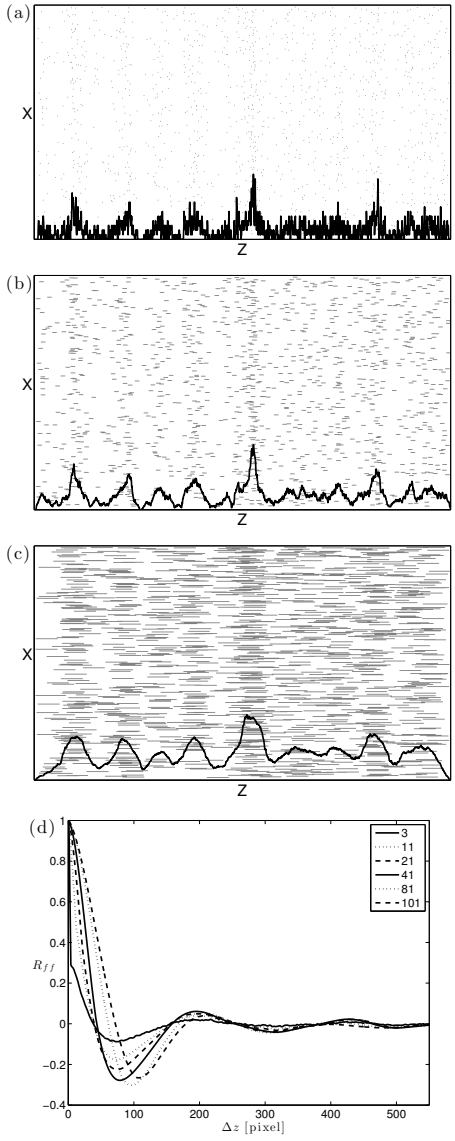

FIGURE 6. Determination of horizontal correlation using particle position from the image in Fig. 2. (a) Image with fixed particle width $w = 3$ pixel and vertical sum of this figure, (b) image with fixed particle width $w = 21$ pixels and vertical sum of this figure, (c) image with fixed particle width $w = 101$ pixels and vertical sum of this figure, (d) correlations for $w = 3, ..., 101$ pixels

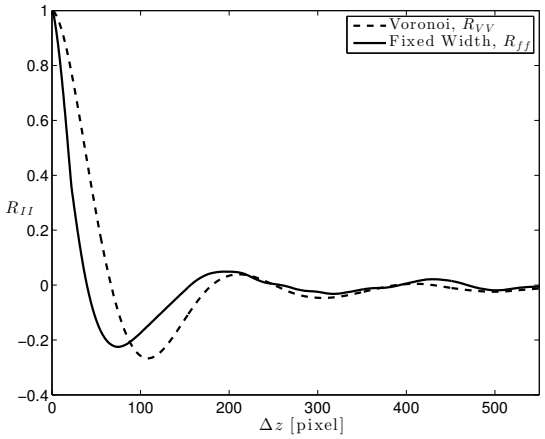

FIGURE 7. Comparison of the Voronoi based correlation, R_{VV}, and the fixed width based correlation, R_{ff}, where the fixed width has been set to 21 pixels and the threshold in the Voronoi analysis to 50%

The minimum value of the correlation is a measure of how coherent the particle structures are, *i.e.* a measure of the strength of the streaks. The streakiness is from here on defined as $\Xi(R_{II}) = |\min(R_{II})|$. A lower negative minimum value of the correlation implies higher or stronger streakiness. In other words, the particle structures in the flow are more coherent.

5. Results and Discussion

5.1. *Fixed width vs. Voronoi based correlation*

In Fig. 7, the correlation of the Voronoi based analysis with a threshold of 50% is depicted together with the correlation using the fixed width method with a particle width of 21 pixels. It can be seen that the Voronoi based method gives a lower minimum and is shifted to the right. The reason for the shift of the correlation curve will be shown to be due to the concentration dependency. An evaluation of the concentration dependency of both methods, and a solution in order to obtain the streakiness and streak width independent of concentration is described below.

5.2. *Effect of number of particles*

5.2a. *Streakiness,* $\Xi(R_{II})$. The number of particles in each image (concentration) affects the analysis independently of the method used. Since experimental images will have a fairly low concentration (even if index-of-refraction has been used and the actual concentration is quite high), the method needs to be able

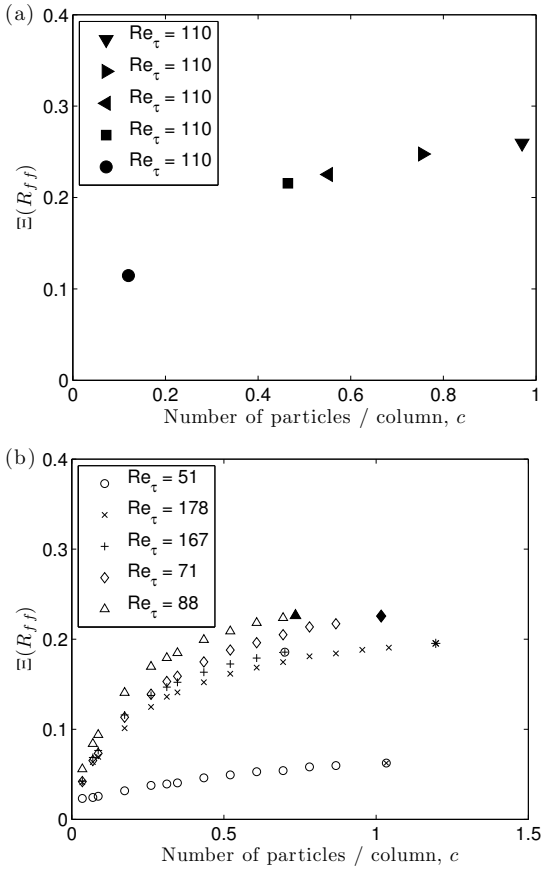

FIGURE 8. Streakiness as a function of concentration using (a) experimental and (b) artificial variation. In (b) several cases corresponding to different Reynolds numbers and concentrations are shown, $(\otimes, *, \oplus, \blacklozenge, \blacktriangle)$ is the original concentration and $(\circ, \times, +, \diamond, \triangle)$ are the artificial variations. Each symbol pair belongs to one experimental case. The fixed width method was used in both (a) and (b)

to handle low concentrations. In order to investigate how the concentration affects the outcome of the different analysis methods, experiments with different concentrations of particles in the suspension were performed, while the flow conditions were kept constant.

The other way of changing the concentration is random removal of particles from the pictures during post processing. In Fig. 8a and 8b, the streakiness,

$\Xi(R_{ff})$, versus the number of particles per pixel column, c, are shown, using the fixed width method. The column width is here kept constant (one pixel), which is different from when D was determined. Fig. 8a depicts results from a physical concentration variation at $\mathrm{Re}_\tau = 110$, case 1-5 in table C.3. In Fig. 8b the artificial concentration variations for five different flow cases are displayed, where the symbols $(\otimes, *, \oplus, \blacklozenge, \blacktriangle)$ represent the original measurements and the symbols $(\circ, \times, +, \diamond, \triangle)$ represent the artificial variations of concentration. The corresponding Reynolds numbers for the five different flow cases are $\mathrm{Re}_\tau = 51, 178, 167, 71$ and 88. The different experiments have different concentrations and different streakiness.

In Fig. 9a the Voronoi based method is used and both physical, $(\bullet, \blacksquare, \blacktriangleleft, \blacktriangleright, \blacktriangledown)$, and artificial, $(\circ, \square, \triangleleft, \triangleright, \triangledown)$, concentration variations are performed. These concentration variations are performed at a constant Reynolds number, $\mathrm{Re}_\tau = 110$. The similarity between the two different concentration variations using the Voronoi method is poor. In Fig. 9b it is shown that by excluding particles in the post processing it is possible to recreate the behavior observed in the experiments using the fixed width method. Note that a naive interpretation of the data in Fig. 8a is that the streakiness varies with concentration, whereas Fig. 9b shows that this variation is an artifact of the evaluation. In section 5.3, corrections for this artifacts are derived and demonstrated to give a consistent quantification of the streakiness.

5.2b. *Streak width,* $2\Delta z(R_{II} = 0)$. Fig. 10 shows both physical $(\bullet, \blacksquare, \blacktriangleleft, \blacktriangleright, \blacktriangledown)$ and artificial $(\circ, \square, \triangleleft, \triangleright, \triangledown)$ concentration variations of the streak half width in pixels. The Voronoi based method and the fixed with method are displayed in Fig. 10a and 10b, respectively. The fixed width method has a stable streak width for concentrations greater than ~ 0.1 particles per column. The Voronoi method on the other hand display a significant variation in streak width, explaining the shift of the Voronoi correlation curve as shown in 7. The behavior of the Voronoi analysis is logic; less particles leads to a larger average cell size, resulting in a larger streak width.

5.3. *Obtaining a consistent measure*

When comparing the two methods, three major advantages can be found for the fixed width method: (i) the streak width is independent of the concentration, (ii) the collapse of the physical and artificial concentration variation is better and (iii) it is computationally cheaper as compared to the Voronoi based method. Due to the above mentioned advantages, the fixed width method is the approach that will be considered and improved so that consistent measures are obtained. The aspects that needs to be taken into account are the concentration and the artificial particle width, w. The latter needs to be considered in relation to the actual streak width why an iteration will be needed in order to find w.

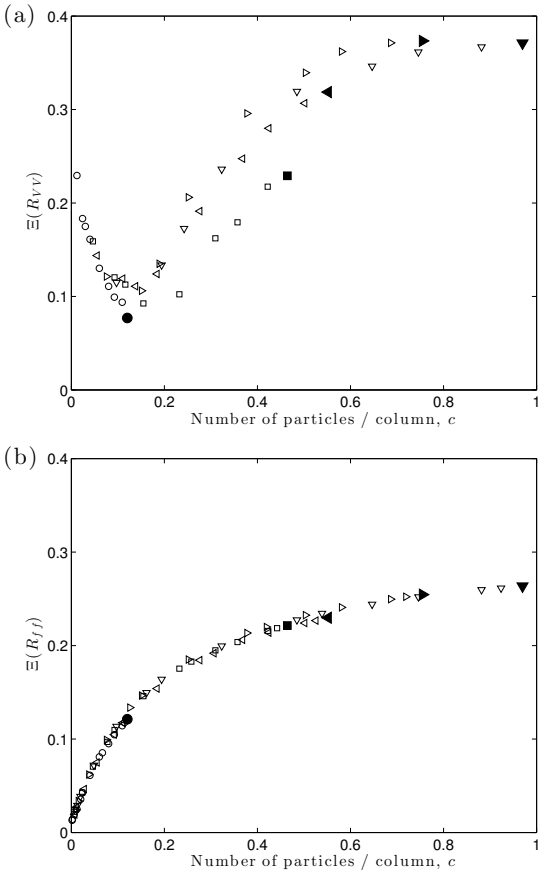

FIGURE 9. Scaling of streakiness for different number of particles, both physical ($\bullet, \blacksquare, \blacktriangleleft, \blacktriangleright, \blacktriangledown$) and artificial ($\circ, \square, \triangleleft, \triangleright, \triangledown$) concentration variations, (a) using Voronoi based correlation and (b) using fixed width correlation

In order to determine the relative streakiness, the particles are first located and given a width, the image is summed in the streak direction to obtain the signal. Thereafter, the auto-correlation is computed using the resulting signal. If the concentration between the measurements is not constant, this needs to be taken into account. Note that this implies that the procedure below has to be applied before concentration effects of streakiness are deduced.

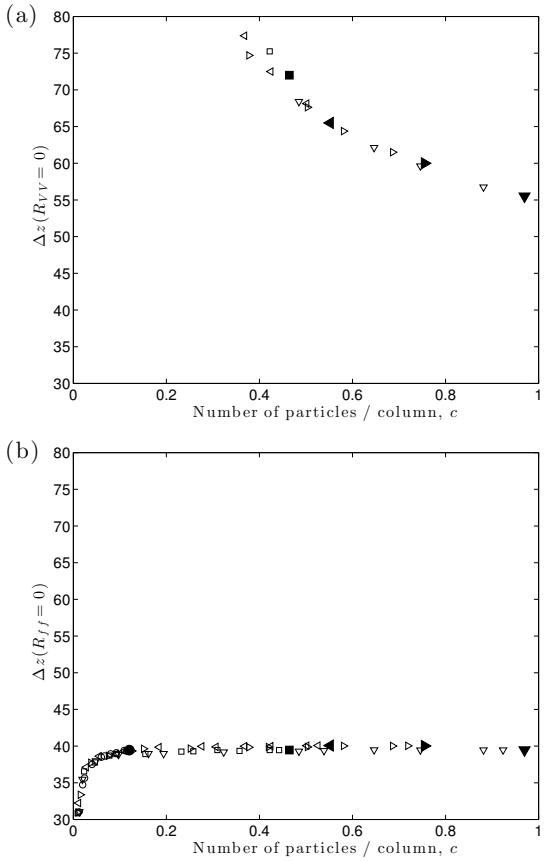

FIGURE 10. Streak width for different number of particles, both physical ($\bullet, \blacksquare, \blacktriangleleft, \blacktriangleright, \blacktriangledown$) and artificial ($\circ, \square, \triangleleft, \triangleright, \triangledown$) concentration variations, (a) using Voronoi based correlation and (b) using fixed width correlation

5.3a. *Concentration.* The concentration dependence is reduced by first assuming that the signal, $I = f(z, c)$, consists of a true signal, $g(z, c)$, and a perturbation, $g'(z, c)$, both dependent on the concentration, $c \in [0, \infty]$, as:

$$f(z, c) = g(z, c) + g'(z, c). \tag{5}$$

The auto-correlation $\hat{R}_{ff}(\Delta z, c)$ can be split into three parts:

$$\begin{aligned} &\hat{R}_{ff}(\Delta z, c) = \\ &\quad = \hat{R}_{gg}(\Delta z, c) + \hat{R}_{gg'}(\Delta z, c) + \hat{R}_{g'g'}(\Delta z, c), \end{aligned} \tag{6}$$

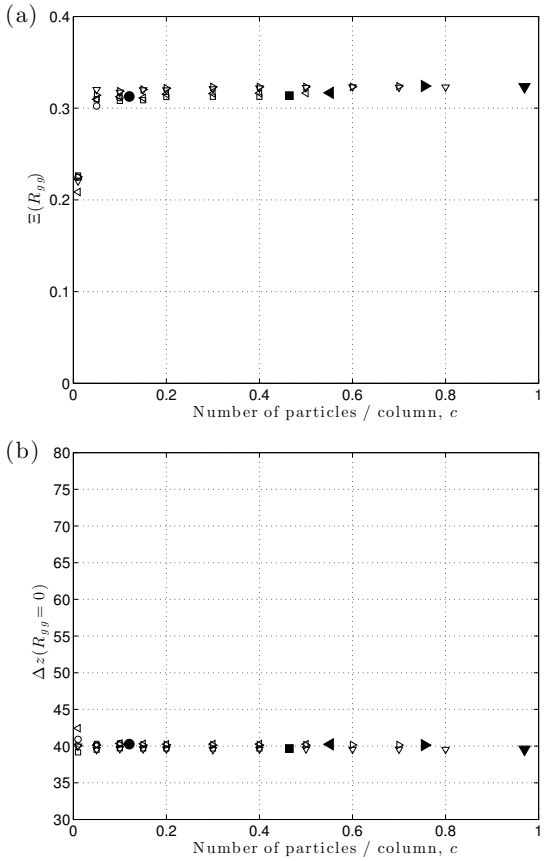

FIGURE 11. (a) Streakiness and (b) streak widths for different number of particles, both physical ($\bullet, \blacksquare, \blacktriangleleft, \blacktriangleright, \blacktriangledown$) and artificial ($\circ, \square, \triangleleft, \triangleright, \triangledown$) concentration variations, from the true correlation R_{gg} (Eq. (7)). Note that the vertical axis limits are the same as in Fig. 9 and Fig. 10

where the correlations are not yet normalized. If the perturbation, g', and the true signal, g, are independent of each other the correlation $\hat{R}_{gg'}$ will be zero, which is assumed from here on. The last term, $\hat{R}_{g'g'}$, will be taken as the auto-correlation of a random image with concentration, c, and artificial particle width, w. This correlation can be computed by placing particles at random positions, thus producing an artificial signal where the parameters c and w have been chosen to match the ones used for the experimental images.

When $\hat{R}_{gg'}$ is set to zero, and c and w are known, a perturbation-corrected correlation is obtained from Eq. (6) as:

$$R_{gg} = \frac{\hat{R}_{ff} - \hat{R}_{g'g'}}{\max(\hat{R}_{ff} - \hat{R}_{g'g'})}, \tag{7}$$

where the last step is to normalize the correlation.

The streakiness and the streak width extracted from the true correlation R_{gg}, in turn calculated from Eq. (7) are shown in Figs. 11a and 11b, respectively. As before, ($\bullet, \blacksquare, \blacktriangleleft, \blacktriangleright, \blacktriangledown$) represents physically varied concentration and ($\circ, \square, \triangleleft, \triangleright, \triangledown$) represents artificially varied concentrations. In Fig. 11a, the apparent concentration dependency of the streakiness in cases 1-5 from Fig. 8a is cancelled for concentrations greater than ~ 0.05 particles per column. Regarding the streak width, the concentration dependency is reduced even more. Note that, for concentrations lower than 0.05 the assumption that g and g' are independent may not be true.

5.3b. *Artificial particle size w.* The correction in Eq. (7) removes the concentration dependence for $c > 0.05$ particles per column. The solely free parameter is the artificial particle width. Fig. 12 depicts how (a) the streakiness and (b) the streak width vary with the artificial particle width for case 1. It is clear that both of these sought quantities depend on w. The streak width increases with increasing w, while the streakiness on the other hand, first assumes a minimum and then a maximum as w increases. It should be noted that the maximum occurs at a particle width much larger compared to the streak width and is therefore disregarded.

In Fig. 13 a close up of the correlation minima for $w = 3, 5, 7, 11, 15, 17, 21,$ 25 pixels are displayed, corresponding to the eight lowest w-values in Fig. 12a and 12b. As w increases the correlation is seen to become smoother, explaining the minimum in Fig. 12a. As low value as possible for w is wanted, but the correlation must be smooth enough to have a well defined minimum in Fig. 13. How to chose w is described in section 5.3d.

5.3c. *Streakiness dependence on streak width.* Since the positions of all particles are known it is easy to test the dependency of streakiness on streak width. When the streak width is artificially changed by multiplying all particle positions with a constant, the effect on the streakiness can be observed. Preferably the streakiness would be constant. Fig. 14 displays three different cases, first the original case ($\triangleright$), and also two cases where the positions of all particles have been multiplied by the factors 1.5 ($*$) and 2 ($\times$). The image size is kept constant. When w is normalized with the streak width, $2\Delta z(R_{gg} = 0)$, the curves collapse, see 14a.

The image finite size finally also needs to be accounted for, due to the loss in information in the auto-correlation. The correlations in Fig. 14 are

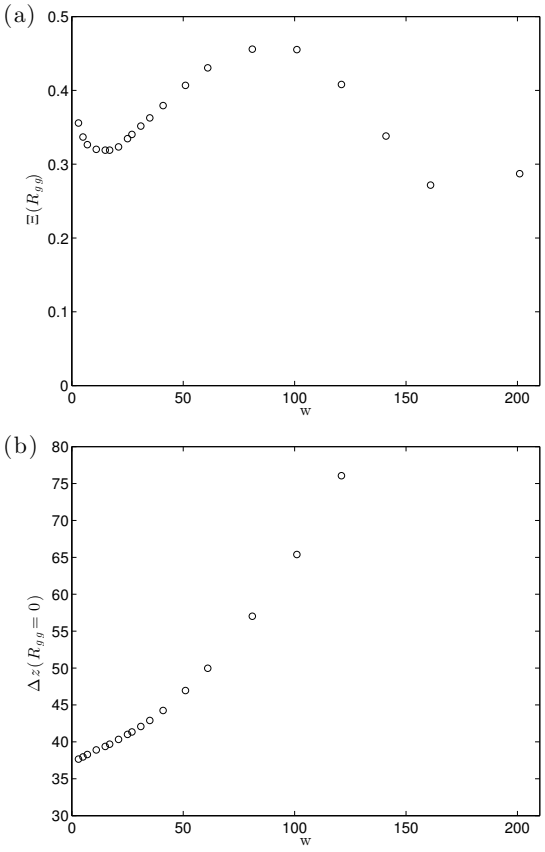

FIGURE 12. Streakiness (a) and streak widths (b) for different artificial particle width, w. The concentration 0.1 particles per column is used

therefore normalized with $(1 - \Delta z/\text{image size})$, and so are all results from here on. This step makes the method independent of image size, Isermann & Münchhof (2011).

The information from this section shows that it is possible to compare the streakiness qualitatively between two different experiments if the same value of $w/2\Delta z(R_{gg} = 0)$ is used, and the image size is taken into account through the normalization above.

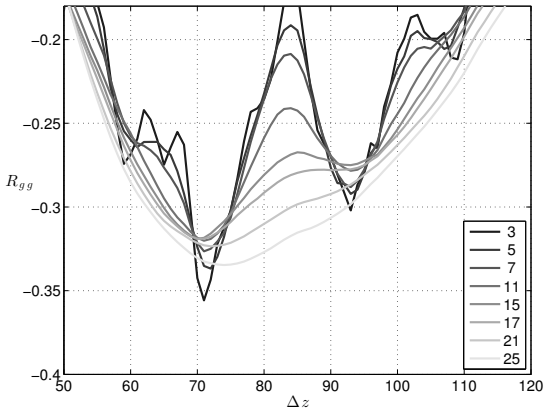

FIGURE 13. Close up off the correlation minima for different w for the same case as in Fig. 12

5.3d. *Streakiness at* $w/2\Delta z(R_{gg} = 0) = 0.2$, $\Xi(R_{gg})_{0.2}$. The final streakiness values, $\Xi(R_{gg})$, and streak widths, $\Delta z(R_{gg} = 0)$, are plotted against the artificial particle width normalized by the streak width in Fig. 15. The concentrations shown are 0.1 and 0.2 particles per column for the five cases, $(\circ, \square, \triangleleft, \triangleright, \triangledown)$, except for the lowest concentration case that has a physical concentration of only 0.12 particles per column. The spread of $\Xi(R_{gg})$, due to jagged correlations at small $w/2\Delta z(R_{gg} = 0)$, for the lowest concentration $(\circ)$, is the reason for why we in this study propose the streakiness to be taken as the value at $w/2\Delta z(R_{gg} = 0) = 0.2$. A subscript is introduced to the streakiness notation, $\Xi(R_{gg})_{0.2}$, in order to indicate which relative particle width that is used. By iteratively varying w and finding the streak width, the value of w which corresponds to $w/2\Delta z(R_{gg} = 0) = 0.2$ can be found. At $\Xi(R_{gg})_{0.2}$ both streakiness and streak width starts to increase, but the deviations up to this point are small.

6. Conclusions

A method that provides consistent measures of streakiness and streak width in particle images from different flow situations has been developed and verified. The final method is independent of particle concentration, image size and streak width as well as the parameters of the method itself.

First, two particle streak analysis methods have been compared and evaluated. The two methods were based on particle positions, summation of images and a following correlation. The streak width and the streakiness were sought. The streak half width, Δz, was taken as the first zero-crossing of the correlation and the streakiness, $\Xi(R_{II}) = |\min(R_{II})|$. The first method was based on

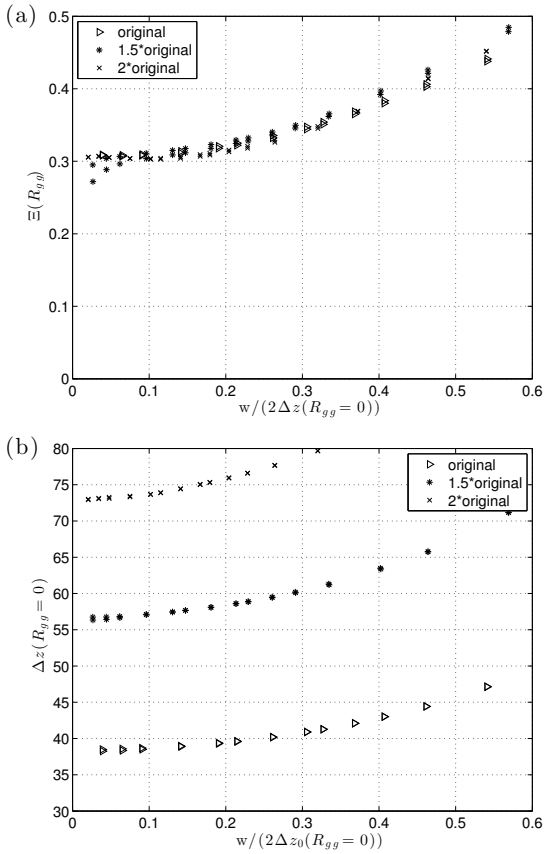

FIGURE 14. Streakiness (a) and streak widths (b) for different streak widths, a collapse of the curves is seen when plotted against $w/2\Delta z(R_{gg} = 0)$ in (a). Original streak width, ($\triangleright$), all particle positions multiplied by 1.5, ($*$) and 2, ($\times$). The image size is kept constant and two concentrations are used (0.1 and 0.2 particles per column)

Voronoi analysis and the second on artificial particles with an assigned fixed width. Both methods were shown to possess a severe concentration dependence.

However, the streak width was shown to be constant at concentrations greater than $\sim$ 0.1 particles per column for the fixed width method. The fixed width method was improved and an expression was derived to account for the concentration dependence of the streakiness. The derivation was based on the assumption that a random image significantly contributes to the total correlation at low concentrations. After this correction, the streakiness was

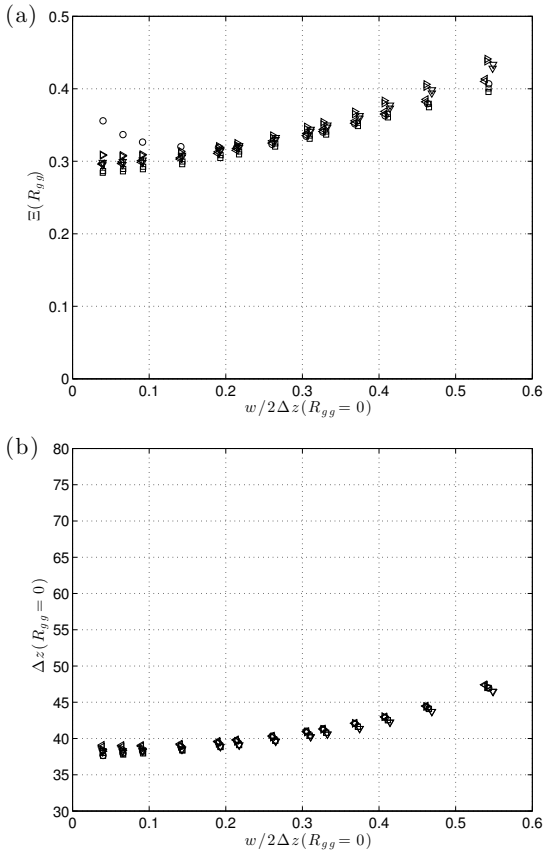

FIGURE 15. Streakiness (a) and streak widths (b) for different artificial particle width, w. Cases 1-5 with two concentrations, 0.1 and 0.2 particles per column, each are displayed $(\circ, \square, \triangleleft, \triangleright, \triangledown)$

shown to be independent of concentrations higher than ~ 0.05 particles per column. Furthermore, scaling the artificial particle width with the streak width made the streakiness independent of streak width. Therefore, and because of the need to smoothen the correlation, it is proposed to set the artificial particle width to 20% of the streak width, denoted $\Xi(R_{gg})_{0.2}$. This results in a resolution criteria of minimum five pixels per streak period.

Mr Joseph Fjellgren is acknowledged for the schematic drawing of the setup. This work was funded by the Knut and Alice Wallenberg Foundation, through

the Wallenberg Wood Science Center. Dr. Lundell and Dr. Prahl Wittberg has also been funded by the Swedish Research Council.

References

Carlsson, A., Håkansson, K., Kvick, M., Lundell, F. & Söderberg, L. D. 2011 Evaluation of steerable filter for detection of fibers in flowing suspensions. *Exp Fluids* **51**, 987–996.

Fessler, J. R., Kulick, J. D. & Eaton, J. K. 1994 Preferential concentration of heavy particles in a turbulent channel flow. *Phys Fluids* **6** (11), 3742–3749.

Fransson, J. H. M. & Alfredsson, P. H. 2003 On the disturbance growth in an asymptotic suction boundary layer. *J Fluid Mech* **482**, 51–90.

Isermann, R. & Münchhof, M. 2011 Correlation analysis with discrete time models. In *Identification of Dynamic Systems*, pp. 179–200. Springer Berlin Heidelberg.

Kaftori, D., Hetsroni, G. & Banerjee, S. 1995*a* Particle behavior in the turbulent boundary layer. I. motion, deposition, and entrainment. *Phys Fluids* **7** (5), 1095–1106.

Kaftori, D., Hetsroni, G. & Banerjee, S. 1995*b* Particle behavior in the turbulent boundary layer. II. velocity and distribution profiles. *Phys Fluids* **7** (5), 1107–1121.

Kulick, J. D., Fessler, J. R. & Eaton, J. K. 1994 Particle response and turbulence modification in fully developed channel flow. *J Fluid Mech* **277**, 109–134.

Kvick, M., Haakansson, K., Lundell, F., Söderberg, L. & Prahl Wittberg, L. 2012 Streak formation and fibre orientation in near wall turbulent fibre suspension flow. *ERCOFTAC Bull* **84**, 19–22.

Lagraa, B., Labraga, L. & Mazouz, A. 2004 Characterization of low-speed streaks in the near-wall region of a turbulent boundary layer. *Eur J Mech B-Fluids* **23** (4), 587–599.

Marchioli, C., Fantoni, M. & Soldati, A. 2010 Orientation, distribution, and deposition of elongated, inertial fibers in turbulent channel flow. *Phys Fluids* **22** (3), 033301.

Monchaux, R., Bourgoin, M. & Cartellier, A. 2010 Preferential concentration of heavy particles: A Voronoï analysis. *Phys Fluids* **22** (10), 103304.

Narayanan, C., Lakehal, D., Botto, L. & Soldati, A. 2003 Mechanisms of particle deposition in a fully developed turbulent open channel flow. *Phys Fluids* **15** (3), 763–775.

Ninõ, Y. & Garcia, M. H. 1996 Experiments on particle - turbulence interactions

in the near - wall region of an open channel flow: implications for sediment transport. *J Fluid Mech* **326**, 285–319.

Pedinotti, S., Mariotti, G. & Banerjee, S. 1992 Direct numerical simulation of particle behaviour in the wall region of turbulent flows in horizontal channels. *International Journal of Multiphase Flow* **18** (6), 927–941.

Rashidi, M., Hetsroni, G. & Banerjee, S. 1990 Particle-turbulence interaction in a boundary layer. *Int J Multiphas Flow* **16** (6), 935–949.

Rouson, D. W. I. & Eaton, J. K. 2001 On the preferential concentration of solid particles in turbulent channel flow. *J Fluid Mech* **428**, 149–169.

Tagawa, Y., Mercado, J. M., Prakash, V. N., Calzavarini, E., Sun, C. & Lohse, D. 2012 Three-dimensional Lagrangian Voronoi analysis for clustering of particles and bubbles in turbulence. *J Fluid Mech* **693**, 201–215.

Paper 3

3

Effect of fibrils on curvature- and rotation-induced hydrodynamic stability

By Mathias Kvick[1,2], Fredrik Lundell[1,2], Lisa Prahl Wittberg[1,2] & L. Daniel Söderberg[1]

[1] Wallenberg Wood Science Center, KTH Mechanics, Royal Institute of Technology, SE – 100 44, Stockholm, Sweden

[2] Linné Flow Centre, KTH Mechanics, Royal Institute of Technology, SE – 100 44, Stockholm, Sweden

With kind permission from Springer Science+Business Media.
Published in *Acta Mechanica* **224** (10) 2249-2261

Flow of a suspension of water and nano-fibrillated cellulose (NFC) in a curved and rotating channel is studied experimentally and theoretically. The aim is to investigate how NFC effects the stability of the flow. This flow is subject to a centrifugal instability creating counter-rotating vortices in the flow direction. These rolls can be both stabilised and destabilised by system rotation, depending on direction and velocity of the rotation. Flow visualisation images with pure water and an NFC/water suspension are categorised and stability maps are constructed. A linear stability analysis is performed, and the effect of fibrils are taken into account assuming straight fibrils and constant orientation distributions, *i.e.* without time dependent flow-orientation coupling. The results show that NFC has a less stabilising effect on the primary flow instability than indicated from the increase in viscosity measured by a rotary viscometer, but more than predicted from the linear stability analysis. Several unknown parameters (the most prominent being fibril aspect ratio and the interaction parameter in the rotary diffusion) appear in the analysis.

---

1. Introduction

The aim of this work is to gain knowledge of curvature and rotation-induced instabilities of nano-fibrillated cellulose (NFC) suspensions. Nano-fibrillated cellulose is a novel material made from wood, and is very interesting from a material point of view, see *e.g.* Eichhorn *et al.* (2010) and references therein for a current review of the research in the area of nano cellulose. NFC is made by disintegrating pulp, consisting of fibres with an approximate length of 2 mm and a diameter of 20 μm. After disintegration, the nano fibrils have a length of order $1-3$ μm and a diameter of $20-40$ nm. Today, when this material

starts to be integrated into established or new industrial processes, it becomes necessary to understand how this addition will effect the flow. Here, a flow case and setup previously studied (with pure water) by Matsson & Alfredsson (1990) will be investigated.

A curved channel with a large aspect ratio on a rotating table is used. The curvature of the channel gives rise to a difference in centrifugal force depending on the velocity of the fluid, resulting in a Dean instability, Dean (1928). This instability takes the form of counter rotating flow rolls in the streamwise direction (primary instability). If the flow velocity is further increased, wavy motions are observed on the rolls (secondary instability) and eventually, breakdown to turbulence occurs.

The rotation of the channel induces a Coriolis force, which magnitude depends on the fluid velocity as well as the angular velocity. The Coriolis force either stabilises or destabilises the curvature-induced instability, depending on the rotational direction. The flow is governed by the Reynolds number (Re) and the rotation number (Ro), defined as:

$$\mathrm{Re} = \frac{U_b d}{\nu}, \tag{1}$$

$$\mathrm{Ro} = \frac{\Omega d}{U_b}, \tag{2}$$

where U_b is the bulk velocity acquired from flow rate measurements, d is the width of the channel, ν is the kinematic viscosity of the suspending fluid and Ω is the angular velocity. Matsson & Alfredsson (1990) investigated the balancing effect of the Coriolis and centrifugal force and compared with results from linear stability theory. It was found that at certain rotational velocities the critical Reynolds number was substantially increased. Here, this rich stability problem will be used as a basis for NFC-suspension stability studies.

Research has previously been performed concerning the stability of fibril suspensions as well as polymer suspensions. Experimental results indicate that elongated particles stabilise certain instabilities, while at the same time destabilise others.

There are not many experimental investigations on hydrodynamic stability of fibre suspension flows. Vaseleski & Metzner (1974) measured pressure drops in pipes of different diameters in order to investigate drag reduction of suspensions with nylon fibres, varying volume fractions and aspect ratios. They found that the transition to turbulence was delayed to higher flow rates, *i.e.* the flow was stabilised. Pilipenko *et al.* (1981) on the other hand, found that the addition of plant fibres in a Taylor apparatus decreased the critical Taylor number and thereby destabilised the flow. This apparent contradiction is explained by the fact that Vaseleski & Metzner (1974) used the solvent viscosity for normalisation, whereas Pilipenko *et al.* (1981) used the viscosity of the suspension. From here on, solvent properties will be used unless the opposite is

stated. Pilipenko *et al.* (1981) also performed a theoretical investigation and concluded that the theoretical and experimental findings were in qualitative agreement.

A few additional theoretical studies will also be reviewed. Gupta *et al.* (2002) applied linear stability theory on a Taylor-Couette flow for a semi-dilute suspension containing non-Brownian fibres and found that the critical Reynolds number was increased compared to the case without fibres. The reason for the stabilisation was in this work suggested to be mainly due to fibre-fibre interactions. Nsom (1996) investigated the effect of fibrils and gap-width on the stability of the flow in a curved channel. The critical wavelength was found to be unaffected by the presence of fibres. Moreover, transition was delayed in both the dilute and semi-dilute regimes.

Azaiez (2000) studied the effects of fibres and polymers, separately, on a mixing layer, by means of linear stability. The stabilising effects of fibres were determined to be a consequence of the orientational diffusivity due to hydrodynamic interactions. Zhenjiang *et al.* (2004) reported similar findings from a linear stability analysis of a fibre suspension flow in a rectangular channel and found that the addition of fibres not only stabilised the flow, but also increased the critical wavenumber.

In this work, an experimental stability study based on flow visualisation images is complemented with a theoretical consideration. The experimental setup and the preparation of the suspension is explained in section 2. The paper continues with a derivation of the linear stability equations including the effect of the fibrils in section 3, where the effect of the fibrils is modelled with an orientation dependent stress tensor. In section 4 the results are presented followed by discussion and conclusions in sections 5 and 6, respectively.

2. Experimental methods

2.1. *Experimental setup*

The experimental apparatus was previously used by Matsson & Alfredsson (1990), who made experiments with water and compared with linear stability theory. The curved channel covers 180° and has a radius of curvature of $\Re = 400$ mm. The channel has a width of 9.25 mm and a height of 280 mm.

The experimental setup is mounted on a table that can be rotated with angular velocities up to a maximum of 10 rpm in both directions. A submersible centrifugal pump drives the flow through the channel, and the flow rate is set by adjusting a valve before the inlet. The flow rate is measured with a rotameter and varies between 0.07–0.45 l/s. The outlet pressure is set with a second valve located after the outlet. A stagnation chamber is located prior to the channel, where packed glass beads are used in order to create a homogenous flow and increase the pressure drop along the channel. Downstream of the stagnation chamber, two turbulence reducing screens are located. The screens, in addition

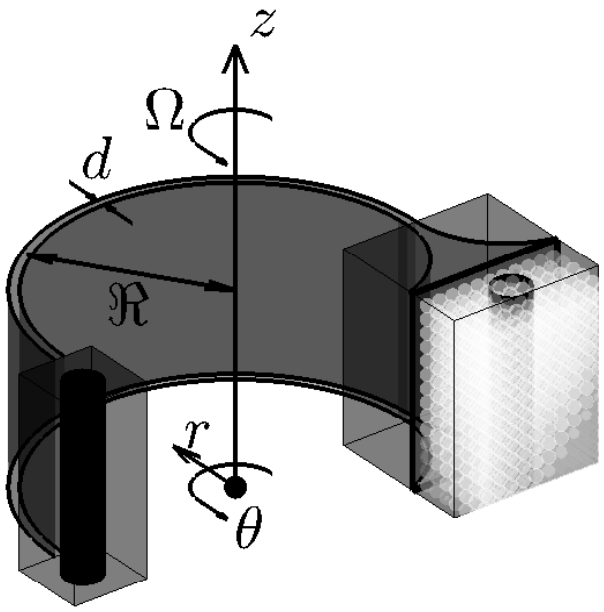

FIGURE 1. Schematic drawing of experimental apparatus. The inlet is located to the right in the figure, where packed glass spheres and a contraction are used to minimise the disturbances in the inflow

with the contraction, are used in order to minimise disturbances at the inlet of the channel.

At a position 65 channel widths, d, downstream of the inlet, a CCD camera is mounted, capturing images of the flow. Two 500W halogen lights are used for illumination of the region of interest. In order to visualise the flow, a small amount of Iriodin® (plate-like particles that visualise flow structures), ~ 1.5 g, is added to the fluid with a total volume of 40 litres, having no measurable impact on the properties of the fluid.

Experiments with pure water and the NFC-suspension described below were carried out and are compared with each other.

2.2. *The NFC suspension*

The NFC has been prepared by an enzymatic pretreatment followed by a high pressure homogenisation at a concentration of 1% by weight, according to the procedure described by Pääkkö *et al.* (2007). The high pressure homogenisation was carried out at Innventia AB[1]. The final concentration after homogenisation

[1]Innventia AB, Box 5604, SE 114 86 Stockholm, Sweden

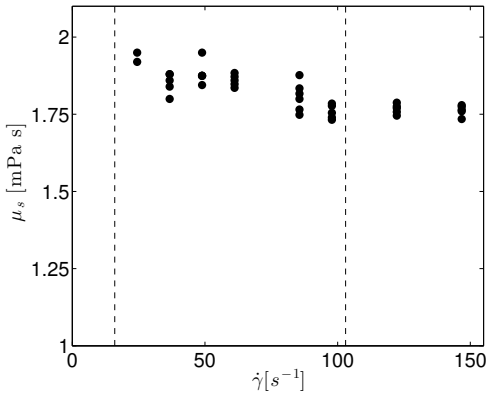

FIGURE 2. Shear viscosity data for the NFC suspension. The dashed lines indicate the minimum, $\dot{\gamma} = 16s^{-1}$, and maximum, $\dot{\gamma} = 103s^{-1}$, shear rates obtained at the wall in the experiments

was $c = 2\%$ by weight, at this concentration the NFC material is a gel. To dilute the NFC-suspension to a much lower concentration, as used in the experiments, $c = 400$ ppm by weight (corresponding to $nl^3 \approx 8$, where n is the number density per unit volume and l is the fibril length), a step wise process was adopted. In the process the concentration was halved and treated with an ultrasonic probe in order to break up flocs, until the desired concentration was reached. Since the NFC used in this study had passed through the high pressure homogenisator only once, a small amount of partial fibres that could not be broken with ultrasound were present in the final suspension.

The viscosity of the NFC suspension was measured using a rotational viscometer. In this study, no further effort was carried out in order to characterise the suspension. However, there are several ongoing efforts in this direction, *e.g.* Iotti *et al.* (2011), Puisto *et al.* (2012). The dynamic viscosity, μ, measured in the viscometer, versus the shear rate, $\dot{\gamma}$, is shown in Fig. 2, where several measurements were performed at the same shear rate. The scatter in the data is most likely due to differences in sedimentation and orientation of the fibrils. The effect of orientation and sedimentation on the measurement was attempted to be circumvented by mixing in-between each measurement. However, regardless of the scatter in the data, it is evident from Fig. 2 that the suspension is weakly shear thinning.

The dashed vertical lines in Fig. 2 show the approximate range of shear rates obtained at the wall in the present experiments. For the shear rates of the present study, the relative viscosity (μ_s/μ_f, where the indices s and f indicate suspension and fluid, respectively) is measured to be between 1.8 and 2 and the shear thinning is thus of the order of 10% or less.

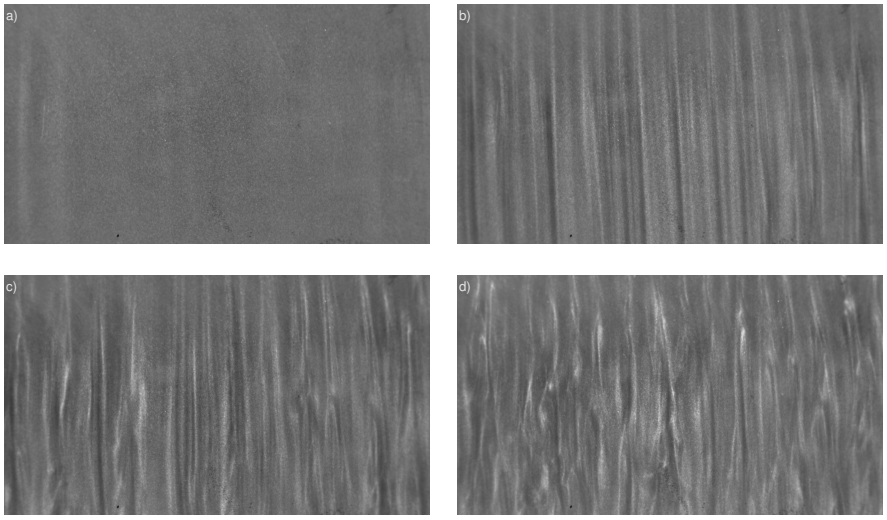

FIGURE 3. Example images for a) laminar, b) primary, c) weak secondary and d) strong secondary regimes, with Re= 595, Ro= $-0.024, 0.0058, 0.039, 0.076$

During the experiments with the NFC-suspension, a limited accumulation of NFC occurred at some positions in the flow loop, resulting in a reduced concentration in the channel. This effect could not be quantified but is expected to be limited since the results are consistent comparing the first and final results of an experimental sequence.

2.3. *Image analysis*

In total, 213 experiments with 50 images in each experiment are presented in this work. The images were categorised by manual inspection of each individual image, and classified into four flow regimes: *laminar*, *primary instability*, *secondary instability* and *turbulent*, as presented in Fig. 3. In order to make the analysis unbiased, the order in which the image sets were shown to the individual performing the categorisation was random, and the process was repeated several times to ensure consistency.

3. Theoretical consideration

3.1. *Single phase flow*

The flow in a curved rotating channel is described by the Navier-Stokes equation together with the continuity equation in cylindrical coordinates as:

$$\frac{Du_r^*}{Dt^*} - \frac{u_\theta^{*2}}{r^*} = -\frac{1}{\rho}\frac{\partial p*}{\partial r^*} + \nu\left[\nabla^2 u_r^* - \frac{u_r^*}{r^{*2}} - \frac{2}{r^{*2}}\frac{\partial u_\theta^*}{\partial \theta^*}\right] + 2u_\theta^*\Omega, \tag{3}$$

$$\frac{Du_\theta^*}{Dt^*} + \frac{u_r^* u_\theta^*}{r^*} = -\frac{1}{\rho r^*}\frac{\partial p^*}{\partial \theta^*} + \nu\left[\nabla^2 u_\theta^* - \frac{u_\theta^*}{r^{*2}} + \frac{2}{r^{*2}}\frac{\partial u_r^*}{\partial \theta^*}\right] - 2u_r^*\Omega, \tag{4}$$

$$\frac{Du_z^*}{Dt^*} = -\frac{1}{\rho}\frac{\partial p^*}{\partial z^*} + \nu\nabla^2 u_z^*, \tag{5}$$

$$\frac{\partial u_r^*}{\partial r^*} + \frac{u_r^*}{r^*} + \frac{1}{r^*}\frac{\partial u_\theta^*}{\partial \theta^*} + \frac{\partial u_z^*}{\partial z^*} = 0, \tag{6}$$

where ρ is the fluid density, and:

$$\frac{D}{Dt^*} = \frac{\partial}{\partial t^*} + u_r^*\frac{\partial}{\partial r^*} + \frac{u_\theta^*}{r^*}\frac{\partial}{\partial \theta^*} + u_z^*\frac{\partial}{\partial z^*}, \tag{7}$$

$$\nabla^2 = \frac{\partial^2}{\partial r^{*2}} + \frac{1}{r^*}\frac{\partial}{\partial r^*} + \frac{1}{r^{*2}}\frac{\partial^2}{\partial \theta^{*2}} + \frac{\partial^2}{\partial z^{*2}}, \tag{8}$$

and the velocity vector is given by:

$$\mathbf{u}^* = u_r^*\mathbf{e}_r + u_\theta^*\mathbf{e}_\theta + u_z^*\mathbf{e}_z. \tag{9}$$

The boundary conditions are:

$$u_r^*(r) = u_\theta^*(r) = u_z^*(r) = 0 \quad \text{at} \quad r^* = \Re \pm \frac{1}{2}d. \tag{10}$$

The flow is decomposed into a mean flow and disturbances, and the velocity field is given by:

$$\mathbf{U} = (u_r^{'*}, V^* + u_\theta^{'*}, u_z^{'*}). \tag{11}$$

Provided that $u_\theta^* = V^*(r^*)$, together with Eqn. (3) results in:

$$-\frac{V^{*2}}{r^*} = -\frac{1}{\rho}\frac{\partial p^*}{\partial r^*} + 2V^*\Omega. \tag{12}$$

The equations are made dimensionless by:

$$u_i = \frac{u_i^*}{U_b}, \tag{13}$$

$$p = \frac{p^*}{\rho U_b^2}, \tag{14}$$

$$t = \frac{t^*}{d/U_b}, \tag{15}$$

$$\theta = \frac{\theta^*}{\xi}, \tag{16}$$

$$z = \frac{z^*}{d}, \tag{17}$$

where $\xi = d/\Re$. In addition, r^* is transformed into the dimensionless coordinate η by $r^* = \Re(1 + \frac{\xi}{2}\eta)$, where $\eta = \pm 1$ on the walls.

The mean velocity is obtained from Eqn. (12) as a perturbation series in ξ, as done by Matsson & Alfredsson (1990),

$$V = \frac{3}{2}(1-\eta^2)(1-\frac{1}{2}\xi\eta) + \mathcal{O}(\xi^2). \tag{18}$$

The perturbations are assumed to be of the form:

$$u_r' = R(\eta)e^{i(\beta z + \alpha\theta - \omega t)}, \tag{19}$$

$$u_\theta' = \Theta(\eta)e^{i(\beta z + \alpha\theta - \omega t)}, \tag{20}$$

$$u_z' = Z(\eta)e^{i(\beta z + \alpha\theta - \omega t)}, \tag{21}$$

$$p' = P(\eta)e^{i(\beta z + \alpha\theta - \omega t)}, \tag{22}$$

where α and β are the streamwise and spanwise wavenumbers, respectively, and ω is the temporal growth rate. The linear stability equations are derived by introducing Eqns. (19) – (22) in Eqns. (3) – (6) and subtract the mean equations. Furthermore, using the narrow gap approximation, $\xi << 1$ and thus neglecting terms of order ξ^2 and higher, this results in the following system of equations;

$$\Big[4\Pi^2 D^2 + 2\xi\Pi D - \beta^2\Pi^2 - \alpha^2 - i\alpha \mathrm{Re} V\Pi\Big]R + \\ + \Big[2\xi \mathrm{Re} V\Pi + 2\mathrm{ReRo}\Pi^2 - 2i\xi\alpha\Big]\Theta - 2\mathrm{Re}\Pi^2 DP = \\ = -i\omega \mathrm{Re}\Pi^2 R + \mathcal{O}(\xi^2), \tag{23}$$

$$\Big[4\Pi^2 D^2 + 2\xi\Pi D - \beta^2\Pi^2 - \alpha^2 - i\alpha \mathrm{Re} V\Pi\Big]\Theta +$$
$$+\Big[-\xi \mathrm{Re} V\Pi - 2\mathrm{Re}V'\Pi^2 - 2\mathrm{ReRo}\Pi^2 + 2i\xi\alpha\Big]R - i\alpha\mathrm{Re}\Pi P =$$
$$= -i\omega\mathrm{Re}\Pi^2\Theta + \mathcal{O}(\xi^2), \quad (24)$$

$$\Big[4\Pi^2 D^2 + 2\xi\Pi D - \beta^2\Pi^2 - \alpha^2 - i\alpha \mathrm{Re} V\Pi\Big]Z - i\beta\mathrm{Re}\Pi^2 P =$$
$$= -i\omega\mathrm{Re}\Pi^2 Z + \mathcal{O}(\xi^2), \quad (25)$$

$$\Big[2\Pi D + \xi\Big]R + i\alpha\Theta + i\beta\Pi Z = 0, \quad (26)$$

where $\Pi = (1 + \frac{\xi}{2}\eta)$, $D = \partial/\partial\eta$, and V is the non-dimensional mean velocity. A detailed derivation (with a slightly different notation) is given by Matsson & Alfredsson (1990).

Eqns. (23) – (26) constitute an eigenvalue problem for the unknown temporal growth rate ω for a given quartet of Re, Ro, β and α. This eigenvalue problem is solved in MATLAB using a Chebyshev spectral collocation method as described by Weideman & Reddy (2000). For each combination of (Re, Ro, α), β can be varied such that the most unstable spanwise wavenumber is found. Repeating at another (Re, Ro, α) combination, the stability in the Re/Ro/α-space can be mapped out.

3.2. *Effect of fibrils*

When fibrils are added to the flow, this causes an addition to the stress tensor σ:

$$\sigma^{tot} = \sigma^{Newtonian} + \sigma^f. \quad (27)$$

This gives rise to an extra term $\nabla \cdot \sigma^f$ in the right hand side of the momentum equations, Eqns. (3) – (5).

Several studies have been carried out to derive an expression for the terms in σ^f, either using slender body theory Batchelor (1970), Shaqfeh & Fredrickson (1990) or via continuum mechanics Ericksen (1960), Lipscomb II *et al.* (1988). The final expression for all cases takes the form:

$$\sigma^f = \nu\Phi[A(\boldsymbol{\varepsilon} : \mathbf{a_4}) + B(\boldsymbol{\varepsilon} \cdot \mathbf{a_2} + \mathbf{a_2} \cdot \boldsymbol{\varepsilon}) + C\boldsymbol{\varepsilon} + E\mathbf{a_2}], \quad (28)$$

where A, B, C and E are rheological parameters, Φ is the volume fraction, $\boldsymbol{\varepsilon}$ is the strain rate tensor, " : " denotes the double dot product and $\mathbf{a_4} =< \mathbf{pppp} >$ and $\mathbf{a_2} =< \mathbf{pp} >$ are the fourth and second order orientation tensor for the fibrils ($\mathbf{p}$ is the orientation vector and $< ... >$ denotes the ensemble average).

In general, the elements in the orientation tensor are calculated using the orientation vector:

$$p_r = \sin\zeta \sin\varphi, \tag{29}$$

$$p_\theta = \sin\zeta \cos\varphi, \tag{30}$$

$$p_z = \cos\zeta, \tag{31}$$

where ϕ and ζ describe the fibril orientation as shown in Fig. 4. For a given orientation distribution, the elements of a_{ijkl} are readily calculated.

The rheological parameters A, B, C and E in Eqn. 28 (see *e.g.* Batchelor (1971), Phan-Thien & Graham (1991), Petrie (1999)) are of the order:

$$A \sim r_p^2 \tag{32}$$

$$B \sim r_p^{-2} \tag{33}$$

$$C = 2 \tag{34}$$

$$E \sim D_r r_p^2 \tag{35}$$

where D_r is the rotational diffusivity and r_p is the aspect ratio of the fibrils. In this study it is assumed that $D_r << 1$ and $r_p >> 1$, therefore eqn. (28) reduces to:

$$\sigma^f = \nu\Phi A(\boldsymbol{\varepsilon} \ : \mathbf{a_4}). \tag{36}$$

In a semi-dilute suspension of rigid fibres, $1/r_p^2 \ll \Phi \ll 1/r_p$, Batchelor (1971) derived the following expression for A:

$$A = \frac{r_p^2}{3\ln(\sqrt{2\pi/\Phi})}. \tag{37}$$

In order to calculate the fourth order orientation tensor, $\mathbf{a_4}$, an equation involving the sixth order orientation tensor $\mathbf{a_6}$ needs to be solved, and so on for higher moments (a description of the orientation tensor can be found in Advani & Tucker III (1987)). This problem is analogous to the closure problem of the Reynolds stresses in turbulence modelling. A closure approximation is needed in order to solve the problem. Petrie (1999) discusses several of the available possibilities. Here, however, the choice of closure approximation is avoided by assuming a stationary orientation distribution. Two different orientation distribution are considered, in case I it is assumed that all fibrils are performing orbits in the $r\theta$-plane, while in case II all fibrils are set to have an orientation parallel to the z-axis.

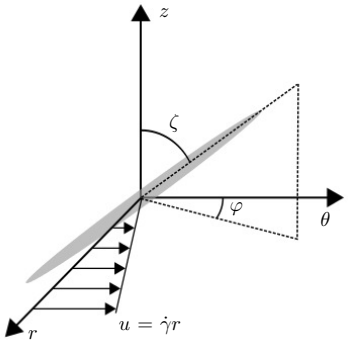

FIGURE 4. Schematic of a fibril in the present shear flow

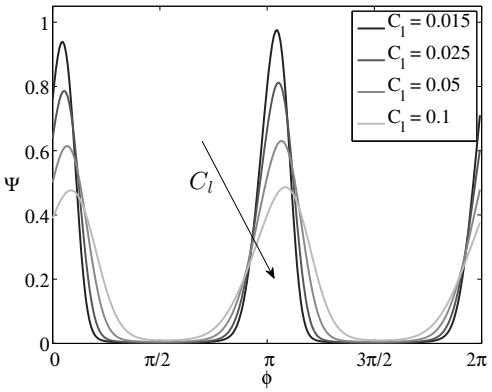

FIGURE 5. Orientation distributions, Ψ, for different values of the interaction coefficient C_l. Considering case I, where the fibrils are performing Jeffery orbits in the $r\theta$-plane

Through the assumption made in case I, the fibril orientation distribution is calculated by describing the angular velocity of the fibrils by:

$$\dot{\varphi} = -\frac{\dot{\gamma}}{r_p^2 + 1}(r_p^2 \sin^2 \varphi + \cos^2 \varphi), \tag{38}$$

where φ is the angle between the fibril and the flow direction, Jeffery (1922). The coordinate system for the fibril can be seen in Fig. 4.

The orientation distribution, Ψ, is found by solving the Smoluchowski equation, *e.g* Doi & Edwards (1986):

$$\frac{\partial}{\partial \varphi}(\dot{\varphi}\Psi - C_l|\dot{\gamma}|\frac{\partial \Psi}{\partial \varphi}) = 0, \tag{39}$$

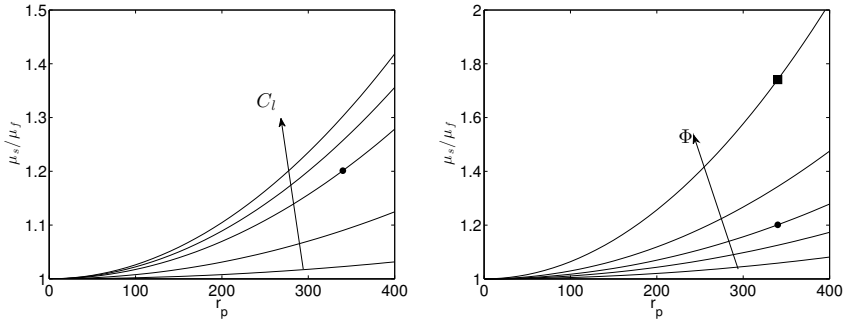

FIGURE 6. Effects of parameters in case I on the suspension viscosity on the fibril stress model used. In both a) and b) the effective viscosity, μ_s/μ_f, is shown versus the aspect ratio r_p. The values chosen in the results are marked by (•) and (■). In a) the volume fraction, $\Phi = 308$ ppm, is kept constant and the interaction coefficient is varied, with the values $C_l = 0, .0001, 0.01, 0.05, 0.1, 1$. In b) the interaction coefficient is kept constant at $C_l = 0.05$ and the volume fraction is varied with the values $\Phi = 10^{-4}, 2 \cdot 10^{-4}, 3.08 \cdot 10^{-4}, 5 \cdot 10^{-4}, 10^{-3}$

where C_l is an interaction coefficient modelling the interactions between the fibrils causing rotary diffusion, Folgar & Tucker (1984) reported values of C_l between 0.0032 – 0.0165 measured in experiments with different fibre aspect ratios and volume fractions. Also note that Ψ in this case is independent of $\dot{\gamma}$. Orientation distributions for several values of C_l are shown in Fig. 5. Based on the orientation distribution it is possible to directly calculate all the elements in the orientation tensor $\mathbf{a_4}$.

As previously mentioned, in case II another type of Jeffery orbits are assumed, where all fibrils have an orientation parallel to the z-axis, resulting in that all elements, except for $a_{zzzz} = 1$, are zero.

Fig. 6 shows the shear viscosity predicted by this model for case I, varying the parameters r_p, C_l and Φ. It is clear that the relative viscosity found in the viscometer (1.8–2, see Fig. 2) can be reached by different parameter combinations. Note that the interaction parameter C_l must be shear dependent in order for the model to become shear thinning. For case II, since all fibrils have an orientation parallel to the z-axis, the fibrils does not influence the shear viscosity, regardless of the choice of parameters.

Using equation (36) to account for the presence of fibrils, the final, non-dimensional, stability equations takes the following form:

$$\Big[4\Pi^2D^2+2\xi\Pi D-\beta^2\Pi^2-\alpha^2-i\alpha\mathrm{Re}V\Pi\Big]R+$$
$$+\Big[2\xi\mathrm{Re}V\Pi+2\mathrm{ReRo}\Pi^2-2i\xi\alpha\Big]\Theta-2\mathrm{Re}\Pi^2DP+$$
$$+A\Phi\Bigg(\Big[4a_{rrrr}\Pi^2D^2+2\xi a_{rrrr}\Pi D+4i\alpha a_{rrr\theta}\Pi D\Big]R+$$
$$+\Big[4a_{rrr\theta}\Pi^2D^2+4i\alpha a_{rr\theta\theta}\Pi D-i\xi\alpha a_{rr\theta\theta}-\alpha^2a_{r\theta\theta\theta}-2\xi a_{r\theta\theta\theta}\Pi D-i\xi\alpha a_{\theta\theta\theta\theta}\Big]\Theta\Bigg)=$$
$$=-i\omega\mathrm{Re}\Pi^2R+\mathcal{O}(\xi^2),\quad(40)$$

$$\Big[4\Pi^2D^2+2\xi\Pi D-\beta^2\Pi^2-\alpha^2-i\alpha\mathrm{Re}V\Pi\Big]\Theta+$$
$$+\Big[-\xi\mathrm{Re}V\Pi-2\mathrm{Re}V'\Pi^2-2\mathrm{ReRo}\Pi^2+2i\xi\alpha\Big]R-i\alpha\mathrm{Re}\Pi P+$$
$$+A\Phi\Bigg(\Big[4a_{rr\theta\theta}\Pi^2D^2+2\xi a_{rr\theta\theta}\Pi D+4i\alpha a_{r\theta\theta\theta}\Pi D-\alpha^2a_{\theta\theta\theta\theta}\Big]\Theta+$$
$$+\Big[4a_{rrr\theta}\Pi^2D^2+4\xi a_{rrr\theta}\Pi D+4i\alpha a_{rr\theta\theta}\Pi D+i\xi\alpha a_{rr\theta\theta}+2\xi a_{r\theta\theta\theta}\Pi D+i\xi\alpha a_{\theta\theta\theta\theta}\Big]R\Bigg)=$$
$$=-i\omega\mathrm{Re}\Pi^2\Theta+\mathcal{O}(\xi^2),\quad(41)$$

$$\Big[4\Pi^2D^2+2\xi\Pi D-\beta^2\Pi^2-\alpha^2-i\alpha\mathrm{Re}V\Pi\Big]Z-i\beta\mathrm{Re}\Pi^2P+A\Phi\Big(-\beta^2a_{zzzz}\Pi^2\Big)Z=$$
$$=-i\omega\mathrm{Re}\Pi^2Z+\mathcal{O}(\xi^2),\quad(42)$$

$$\Big[2\Pi D+\xi\Big]R+i\alpha\Theta+i\beta\Pi Z=0,\quad(43)$$

where a_{ijkl} are the (possible) non-zero elements in the fourth order orientation tensor. The four equations above constitute an eigenvalue problem that is solved as previously described for the single phase problem.

4. Results

4.1. *Experimental results*

Images of the flow are analysed by visual inspection, assigning each experimental case to one of four regimes. In Fig. 3, example images from different regimes at a constant Reynolds number (Re= 595) are shown for different rotational numbers (Ro= $-0.024, 0.0058, 0.039, 0.076$), the flow is from top to bottom in the images. As evident from the images, the difference between Figs. 3a and

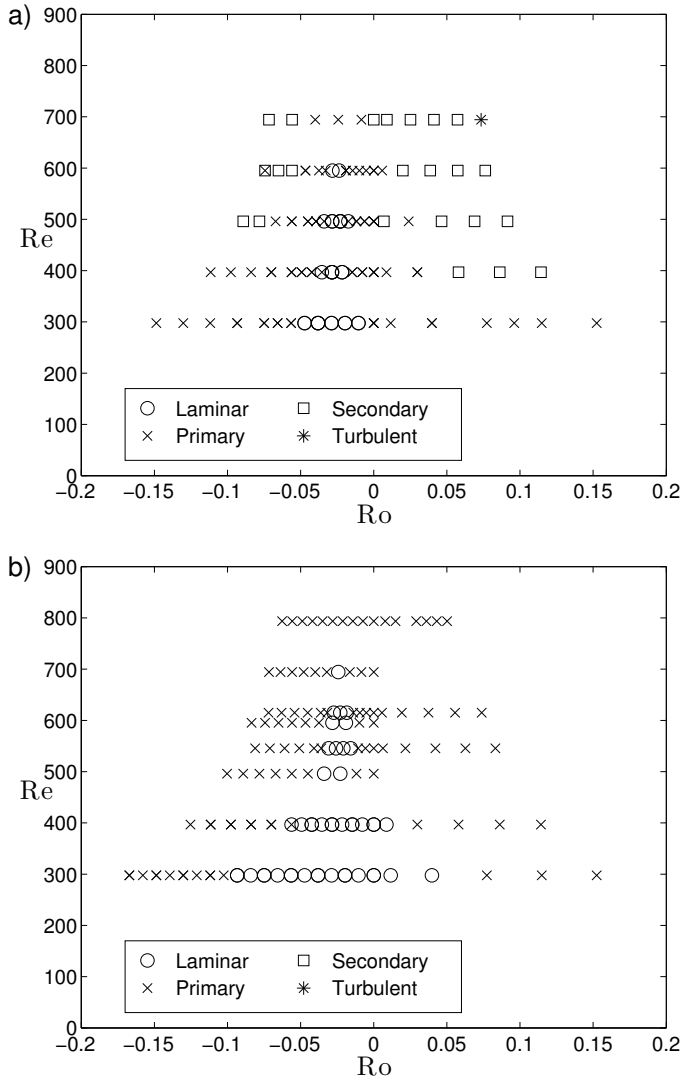

FIGURE 7. State diagrams for a) pure water and b) NFC suspension. The Reynolds number is in both Fig. based on the viscosity of water

3b is very distinct. Thus, the transition from laminar flow to the primary instability is well defined. The following transitions (from primary to secondary) is less clear.

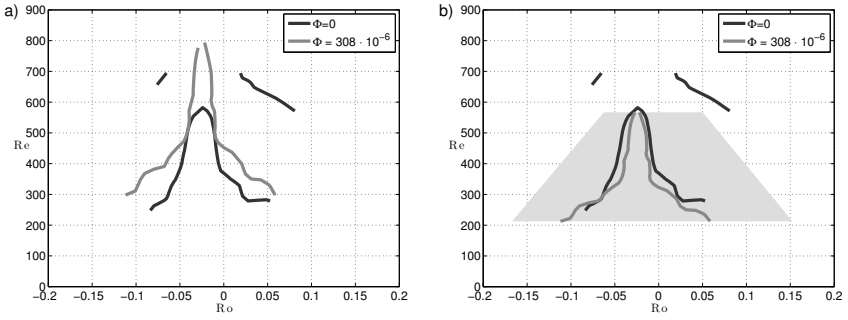

FIGURE 8. Contours showing the transition from laminar to primary and primary to secondary in Fig. 7: a) Reynolds number is based on the viscosity of water and b) the Reynolds number has been scaled by a factor of 1.4 for the NFC suspension, the shaded area indicates the location of the experiments for the NFC-suspension

In Fig. 7, the results from the visual inspection has been summarised in two plots showing the regime that each case belongs to for (7a) pure water and (7b) NFC suspension. The Reynolds number is in both figures based on the viscosity of water. The laminar region (∘) extends up to the highest Re at Ro ≈ -0.03. At this rotation rate, the centrifugal (from curvature) and Coriolis (from rotation) forces balance each other. If Ro is changed from this values, the balance is disturbed, and the flow becomes unstable at lower Re.

Comparing Figs. 7a and 7b, the NFC clearly stabilises the flow, the laminar region is greater and there are no secondary instabilities observed in the studied parameter space. Fig. 8a depicts the contours of the first (from laminar to primary instability) and second transition (from primary to secondary instability) for the case of the pure water as well as the NFC-suspension. In Fig. 8b, the Reynolds number for the NFC suspension has been scaled with a factor of 1.4, which results in a collapse of the peaks. This is considerably smaller than the measured relative viscosity, 1.8 – 2, see Fig. 2.

Also note that the shaded region in Fig. 8b indicate the parameter space spanned with the NFC-suspension. This area only touches the secondary transition and thus, the only conclusions regarding the onset of the secondary instability with NFC that can be made is that the secondary instability does not seem to be enhanced.

4.2. *Linear stability results*

In Fig. 9 results from the linear stability analysis are shown as the neutral stability curve in the Re-Ro-plane for different volume fractions of fibrils, $\Phi =$

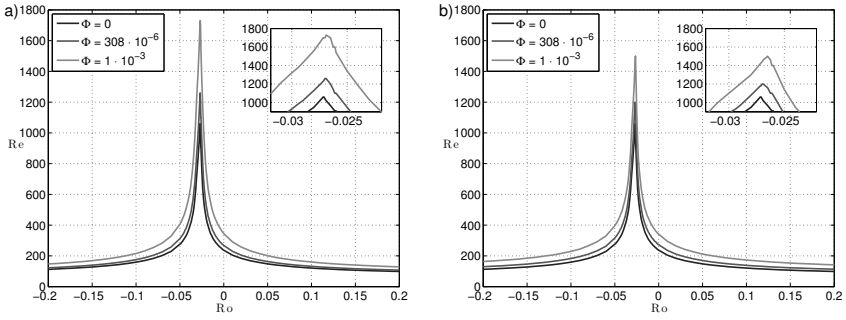

FIGURE 9. Contours showing primary instability obtained by linear stability analysis for different volume fractions, Φ, of fibrils considering a) Case I, where the fibrils performing Jeffery orbits in the shear plane and b) Case II, all fibrils have an orientation parallel to the z-axis. Here an aspect ratio of $r_p = 340$ and an interaction coefficient $C_l = 0.05$ are used

308 ppm correspond to the amount used in the experiments. The aspect ratio ($r_p = 340$) and interaction coefficient ($C_l = 0.05$) has been chosen such that the calculated effective viscosity is equal to $\mu_s/\mu_f = 1.2$ at the concentration of the experiments (see Fig. 6). This corresponds well to what the scaling observed in Fig. 8b. In Fig. 9a, the neutral stability curve obtained for case I by linear theory is shown, where the fibrils are assumed to perform Jeffery orbits in the shear plane. In Fig. 9b, case II is considered, where all the fibrils have an orientation parallel to the z-axis.

The effects of the fibrils are stronger in Fig. 9a than in Fig. 9b. It is thus clear that fibres in the flow direction have a larger effect on the stability than fibres normal to the flow direction. We will therefore concentrate on the former. These results will be discussed in terms of the critical Reynolds number Re_c, defined as the highest Re at which the flow can be stable. In Fig. 9a the effect on Re_c is less than 20% when comparing pure water ($\Phi = 0$, the black curve) with the experimental $\Phi = 308$ ppm (see the inset). At $\Phi = 0.001$ (where the relative viscosity is around 2.5, see Fig. 6b), the effect on the critical Re is approximately 60%. In the experiments, with a concentration of $\Phi = 308$ ppm, the difference was 40%, since the scaling factor in Fig. 8b is 1.4. Moreover, the spanwise wavenumber was in the linear stability analysis found to be modified slightly by the addition of fibres. However, this modification was very small ($\mathcal{O}(3\%)$) and will not be discussed here.

5. Discussion

The discussion will focus on a comparison between the experimental observations and the theoretical results from case I, which is the more realistic case,

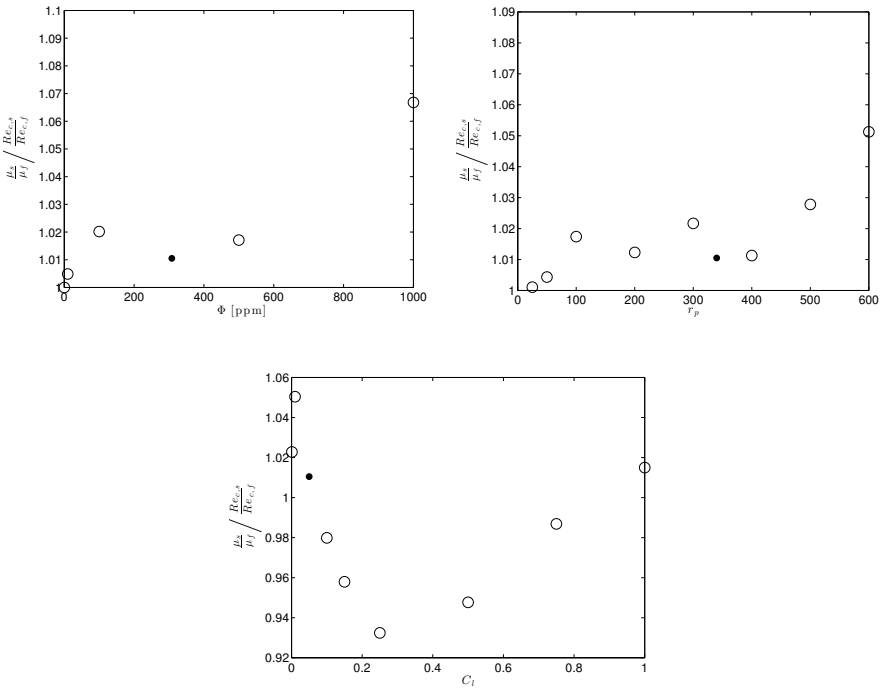

FIGURE 10. The ratio between relative viscosity and increase in critical Re, $(\mu_s/\mu_f)/(Re_{c,s}/Re_{c,f})$, for different values of Φ, r_p and C_l. The variation is performed around the solid points, which are the same as the solid circles in Fig. 6 ($\Phi = 308$ ppm, $r_p = 340$, $C_l = 0.05$

even if idealised, due to initial alignment of the fibrils as they enter the channel. The experimental results show that the critical curves in the Re/Ro-plane for pure water and the NFC suspension collapsed when the Re (i.e. viscosity) of the NFC suspension was scaled with a factor 1.4. This factor is considerable smaller than the relative viscosity measured by the viscometer measurements, which is in the range 1.8–2. The same trend is seen in the theoretical consideration: the relative effect on viscosity is larger than the effect on stability measured by $\mathrm{Re}_{c,s}/\mathrm{Re}_{c,f}$.

The predicted viscosity varies with the parameters Φ, r_p and C_l. These three parameters differs in the sense that the first two correspond to fairly straightforward physical quantities, whereas the third is the averaged result of hard-to-model physical processes. For reasonable values of these parameters, the rheological model used in this work underestimates the relative viscosity.

The relative effect of fibrils on bulk viscosity vs. relative effect on critical Reynolds number is measured by $(\mu_s/\mu_f)/(Re_{c,s}/Re_{c,f})$. The experimental values of this property is 1.3–1.4. Theoretically calculated values are plotted in Fig. 10 for different Φ, r_p and C_l. The variation is performed around the values marked with a solid circle in Fig. 6. The effects of Φ, r_p and C_l are around 10%. For the (physically reasonable) values used, the value is around 1, i.e. considerably lower than observed in experiments.

Here, a constant orientation distribution was used. However, as the flow rolls are formed, the actual orientation distribution will change. To what extent this feature will explain the difference between observed and predicted behaviour is left for future works. Unfortunately, such an effort will rely on a closure model and therefore, one additional factor enters the analysis. An alternative approach would be to perform simulations that rely on first principles to a larger extent.

When it comes to the viscometer, the orientation distribution is more random in the viscometer as compared to what can be expected in the flow channel, assuming alignment in the contraction. It is clear that if quantitative comparisons between rheology measurements, experiments and theoretical considerations are to be made, the orientation distributions have to be determined to an extent that may be unfeasible. The present flow system provides a stability mapping in the Re/Ro-plane. Thus, effects of different parameters (Φ, C_l, r_p) is obtained as a curve rather than a point. Consequently, effects, causes and predictability are explored with increased precision, in spite of the elusive orientation distribution.

6. Conclusions

Stability of an NFC-suspension flowing in a curved and rotating channel has been studied. The main conclusions are;

- The primary instability is stabilised as NFC is added.
- The increase of the critical Reynolds number is less than what could be expected from the effective viscosity measured by a viscometer.
- A theoretical consideration has been performed. For reasonable parameter values, the rheological model underpredicts the effective viscosity as well as the effect on stability.
- The effect on bulk viscosity is larger than the effect on stability in the experiments but similar in the theoretical consideration.

The conclusions highlight the difficulties inherent in modelling and predicting unsteady behaviour of NFC-suspension flow. This is consistent with previous observations of polymer and fibre suspension flows. However, the present experiment provides a complete stability map and thus, quantitative comparisons of relative effects could be made.

This work has benefitted from discussions held during and between events organised by COST action FP1005: "Fibre Suspension Flow Modelling".

Furthermore, Yu Nishio, Tohoku University, Japan, is greatly acknowledged for restoring the experimental setup.

This work was funded by the Wallenberg Wood Science Center.

References

Advani, S. G. & Tucker III, C. L. 1987 The use of tensors to describe and predict fiber orientation in short fiber composites. *J Rheol* **31** (8), 751–784.

Azaiez, J. 2000 Linear stability of free shear flows of fibre suspensions. *J Fluid Mech* **404**, 179–209.

Batchelor, G. K. 1970 The stress system in a suspension of force-free particles. *J Fluid Mech* **41** (03), 545–570.

Batchelor, G. K. 1971 The stress generated in a non-dilute suspension of elongated particles by pure straining motion. *J Fluid Mech* **46** (04), 813–829.

Dean, W. R. 1928 Fluid motion in a curved channel. *Proc Roy Soc London A* **121** (787), 402–420.

Doi, M. & Edwards, S. F. 1986 *The Theory of Polymer Dynamics*. Oxford University Press.

Eichhorn, S., Dufresne, A., Aranguren, M., Marcovich, N., Capadona, J., Rowan, S., Weder, C., Thielemans, W., Roman, M., Renneckar, S., Gindl, W., Veigel, S., Keckes, J., Yano, H., Abe, K., Nogi, M., Nakagaito, A., Mangalam, A., Simonsen, J., Benight, A., Bismarck, A., Berglund, L. & Peijs, T. 2010 Review: current international research into cellulose nanofibres and nanocomposites. *J Mater Sci* **45**, 1–33.

Ericksen, J. 1960 Transversely isotropic fluids. *Colloid Polym Sci* **173**, 117–122.

Folgar, F. & Tucker, C. L. 1984 Orientation behavior of fibers in concentrated suspensions. *J Reinf Plast Comp* **3** (2), 98–119.

Gupta, V. K., Sureshkumar, R., Khomami, B. & Azaiez, J. 2002 Centrifugal instability of semidilute non-brownian fiber suspensions. *Phys Fluids* **14** (6), 1958–1971.

Iotti, M., Gregersen, O. y., Moe, S. r. & Lenes, M. 2011 Rheological studies of microfibrillar cellulose water dispersions. *J Polym Environ* **19**, 137–145.

Jeffery, G. B. 1922 The motion of ellipsoidal particles immersed in a viscous fluid. *P Roy Soc Lond A Mat* **102** (715), 161–179.

Lipscomb II, G., Denn, M., Hur, D. & Boger, D. 1988 The flow of fiber suspensions in complex geometries. *J Non-Newton Fluid* **26** (3), 297–325.

Matsson, O. J. E. & Alfredsson, P. H. 1990 Curvature- and rotation-induced instabilities in channel flow. *J Fluid Mech* **210**, 537–563.

Nsom, B. 1996 Stability of fiber suspension flow in curved channel. *J Phys II* **6** (10), 1483–1492.

Pääkkö, M., Ankerfors, M., Kosonen, H., Nykänen, A., Ahola, S., Österberg, M., Ruokolainen, J., Laine, J., Larsson, P. T., Ikkala, O. & Lindström, T. 2007 Enzymatic hydrolysis combined with mechanical shearing and high-pressure homogenization for nanoscale cellulose fibrils and strong gels. *Biomacromolecules* **8** (6), 1934–1941.

Petrie, C. J. 1999 The rheology of fibre suspensions. *J Non-Newton Fluid* **87** (2–3), 369–402.

Phan-Thien, N. & Graham, A. L. 1991 A new constitutive model for fibre suspensions: flow past a sphere. *Rheol Acta* **30**, 44–57.

Pilipenko, V. N., Kalinichenko, N. M. & Lemak, A. S. 1981 Stability of the flow of a fiber suspension in the gap between coaxial cylinders. *Soviet Physics Doklady* **26**, 646.

Puisto, A., Illa, X., Mohtaschemi, M. & Alava, M. J. 2012 Modeling the viscosity and aggregation of suspensions of highly anisotropic nanoparticles. *Eur Phys J E* **35** (1), 6.

Shaqfeh, E. S. G. & Fredrickson, G. H. 1990 The hydrodynamic stress in a suspension of rods. *Phys Fluids A-Fluid* **2** (1), 7–24.

Vaseleski, R. C. & Metzner, A. B. 1974 Drag reduction in the turbulent flow of fiber suspensions. *AIChE J* **20** (2), 301–306.

Weideman, J. A. & Reddy, S. C. 2000 A matlab differentiation matrix suite. *ACM Trans Math Softw* **26** (4), 465–519.

Zhenjiang, Y., Jianzhong, L. & Zhaosheng, Y. 2004 Hydrodynamic instability of fiber suspensions in channel flows. *Fluid Dyn Res* **34** (4), 251–271.

Paper 4

4

Effect of fibres on hydrodynamic stability in a curved rotating channel

By Mathias Kvick[1,2], Fredrik Lundell[1,2], Lisa Prahl Wittberg[1,2] & L. Daniel Söderberg[1]

[1] Wallenberg Wood Science Center, KTH Mechanics, Royal Institute of Technology, SE – 100 44, Stockholm, Sweden
[2] Linné Flow Centre, KTH Mechanics, Royal Institute of Technology, SE – 100 44, Stockholm, Sweden

Published in proceedings of *International Conference of Multiphase Flows* Jeju 2013

Experiments and a linear stability analysis are performed for a range of flow velocities and rotation rates in a curved and rotating, high aspect ratio, rectangular, channel. The study is carried out in order to investigate the effect of Nano-Fibrillated Cellulose (NFC) on the hydrodynamic stability. In the experiments, the structures in the flow are visualised and images are acquired at a downstream position. In the linear stability analysis, the presence of fibres is modelled as an orientation dependent stress tensor, where the orientation is calculated based on Jefferys equations. A clear stabilisation is found when NFC is present, both in the experiments and in the theoretical work. However, this stabilisation is less than predicted by the effective viscosity. Moreover, the transient growth is found to a greater extent to be affected by the presence of fibres compared to the stabilisation, while the spanwise wavenumber is more or less unaffected.

---

1. Introduction

This work aims to investigate the effect of Nano-Fibrillated Cellulose (NFC) on hydrodynamic stability. NFC is a novel material made from wood, produced by fibrillation of paper pulp to fibrils with lengths $l = 1 - 3\mu m$ and diameters $d = 20 - 40nm$, see Pääkkö *et al.* (2007) for details on the manufacturing method, and Eichhorn *et al.* (2010) for examples of current research areas involving NFC. Due to the many possible applications, the impact of NFC when it is introduced into industrial processes needs to be investigated. With that in mind, the influence of NFC on hydrodynamic stability will be investigated. The hydrodynamic stability of the selected flow case has previously been investigated for single phase by Matsson & Alfredsson (1990). The flow in this curved and rotating channel is governed by the Reynolds number (Re) and rotation number (Ro), defined as:

$$\mathrm{Re} = \frac{U_b d}{\nu} \tag{1}$$

$$\mathrm{Ro} = \frac{\Omega d}{U_b}, \tag{2}$$

where U_b is the bulk velocity, d is the width of the channel, ν is the kinematic viscosity of the suspending fluid and Ω is the angular velocity.

The curvature of the channel gives rise to a centrifugal force acting on the fluid, which magnitude depends on the velocity of the fluid, and therefore also on the radial position. Due to the radial dependence of this force, the flow in the channel is destabilised, resulting in what is known as the Dean instability (Dean 1928) at a sufficiently large Reynolds number. This primary instability takes the form of streamwise vortices. Increasing the Reynolds number further causes the vortices to oscillate, *i.e.* the secondary instability, and at a large enough Reynolds number breakdown to turbulence occurs. The rotation of the channel causes a Coriolis force to appear. The Coriolis force depends on the fluid velocity as well as the rotational velocity, and will either counteract or enhance the curvature-induced instability depending on the rotational direction. The presence of these two, competing or collaborating, destabilising effects, provides a possibility to investigate the transition from laminar flow to the primary instability in the Re-Ro plane.

The effect of fibres on hydrodynamic stability is far from well understood, and only a few experimental investigations have been performed in this area. Vaseleski & Metzner (1974) found that the addition of nylon fibres in pipe flow delayed the transition to turbulence. In contradiction to this, Pilipenko *et al.* (1981), performed experiments in a Taylor apparatus using plant fibres and found that the critical Taylor number decreased. However, the apparent contradiction between these two experimental studies can easily be explained by the definition of the viscosity. Vaseleski & Metzner (1974) used the viscosity of the suspending fluid while Pilipenko *et al.* (1981) used the fibre suspension viscosity. In this paper, all fluid properties refer to the suspending fluid. The theoretical works available in literature are more extensive and consistent compared to the experimental studies mentioned earlier, however only a few will be mentioned here. Azaiez (2000) carried out a linear stability analysis on a fibre suspension in a mixing layer. In this study, the stabilising effect of the fibres was found to be caused by hydrodynamic interaction among the fibres. Zhenjiang *et al.* (2004) studied the linear stability of a fibre suspension in a rectangular channel. As well as observing the stabilising effect of fibres, the addition of fibres was in this case found to cause an increase in the critical wavenumber.

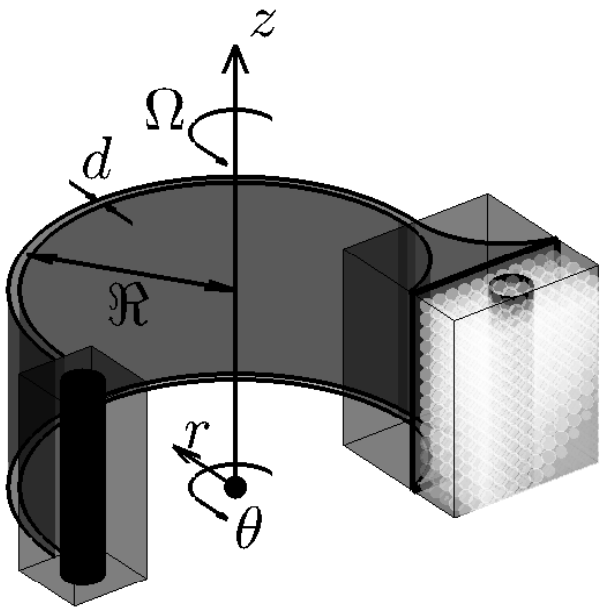

FIGURE 1. Experimental setup. The inlet is located to the right in the image.

In the present study, the stabilising effect of NFC is investigated by the means of experiments and theoretical considerations. In addition, an effort is made to investigate the effect of NFC on the transient growth and critical wavenumbers, from results obtained with linear stability theory.

2. Experimental Facility

The experimental setup, shown in figure 1, consists of a curved rectangular channel with a contraction at the inlet. At a position more than 60 channel heights downstream of the inlet, a CCD camera is placed in order to acquire images of the structures in the flow. For the flow-structures to be visible, a small amount of Iriodin (EMD Chemicals) is added to the fluid. Two selected images of the structures in the flow are shown in figure 2. The distinction between the laminar flow in figure 2 a) and the onset of the primary instability in figure 2 b) is clearly visible. In order to detect the transition line between the laminar region and the primary instability, the images are manually inspected, and each experiment is assigned to one of the two regimes.

3. Theoretical Consideration

The flow is governed by the Navier-Stokes equations in cylindrical coordinates, with an additional stress tensor due to the presence of fibres. Assuming weak

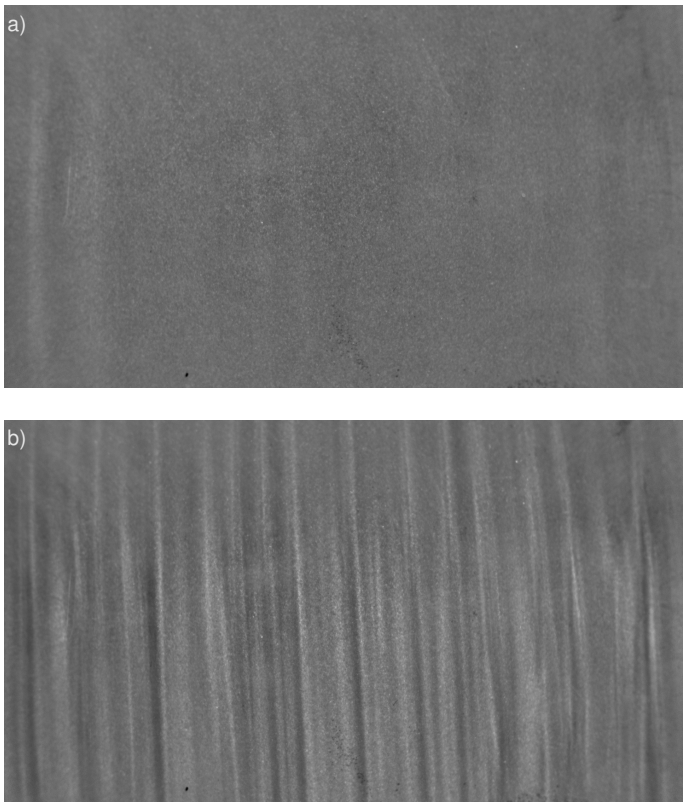

FIGURE 2. Examples of images acquired during an experiment at Re= 595 and a) Ro = −0.24 and b) Ro = 0.58.

Brownian motion and large fibre aspect ratio, the additional stress tensor takes the following form:

$$\sigma^f = \nu\Phi A(\varepsilon : a_4), \tag{3}$$

where Φ is the volume fraction of fibres, A is a rheological parameter (see Batchelor (1971)), ε is the strain rate and $a_4 =< pppp >$ is the fourth order orientation tensor, $< >$ denotes the ensemble average over all fibres and p is the orientation vector along the fibres. The orientations of the fibres are modelled by assuming that the fibres are performing orbits according to Jeffery (1922) in the shear-plane. This provides the possibility to calculate the angular velocities of the fibres by the Jeffery equations. The obtained angular velocities are thereafter used to calculate the orientation distribution from the Smoluchowski equation:

$$\frac{\partial}{\partial\phi}\left(\dot{\phi}\Psi - C_l|\dot{\gamma}|\frac{\partial\Psi}{\partial\phi}\right) = 0, \tag{4}$$

where ϕ is the orientation angle, Ψ is the orientation distribution, C_l is an interaction parameter and $\dot{\gamma}$ is the shear rate. Once the orientation distribution is known, the orientation vector is easily obtained and the orientation tensor, a_4, is readily calculated.

To investigate the hydrodynamic stability, the flow field is decomposed into a mean flow and small disturbances as;

$$\bar{U} = (u_r', V + u_\theta', u_z'), \tag{5}$$

where $V = V(y)$ is the mean velocity profile. The disturbances are assumed to be of the form;

$$\begin{aligned} u_r' &= R_i(\eta)e^{i(\beta z+\alpha\theta-\omega t)} \\ u_\theta' &= \Theta_i(\eta)e^{i(\beta z+\alpha\theta-\omega t)} \\ u_z' &= Z_i(\eta)e^{i(\beta z+\alpha\theta-\omega t)} \\ p' &= P_i(\eta)e^{i(\beta z+\alpha\theta-\omega t)}, \end{aligned} \tag{6}$$

where β and α are the spanwise and streamwise wavenumbers, respectively, ω is the temporal growth rate and η is the non-dimensional, wall normal, coordinate. By introducing equation 7 into the Navier-Stokes equations, the linear stability equations are obtained when subtracting the mean flow and linearising the equations. Using the narrow gap approximation, $\xi = d/Ra << 1$, and therefore neglecting terms of order ξ^2 or higher, the final stability equations are obtained as;

$$\begin{aligned} &\Big[4\Pi^2D^2 + 2\xi\Pi D - \beta^2\Pi - \alpha^2 - i\alpha\mathrm{Re}V\Pi\Big]R + \\ &+\Big[2\xi\mathrm{Re}V\Pi + 2\mathrm{ReRo}\Pi^2 - 2i\xi\alpha\Big]\Theta - 2\mathrm{Re}\Pi^2DP + \\ &+A\Phi\Bigg(\Big[4a_{rrrr}\Pi^2D^2 + 2\xi a_{rrrr}\Pi D + 4i\alpha a_{rrr\theta}\Pi D\Big]R + \\ &+\Big[4a_{rrr\theta}\Pi^2D^2 + 4i\alpha a_{rr\theta\theta}\Pi D - i\xi\alpha a_{rr\theta\theta} - \alpha^2 a_{r\theta\theta\theta}\Pi D - i\xi\alpha a_{\theta\theta\theta\theta}\Big]\Theta\Bigg) = \\ &\qquad = -i\omega\mathrm{Re}\Pi^2R + \mathcal{O}(\xi^2) \end{aligned} \tag{7}$$

$$\Big[4\Pi^2 D^2 + 2\xi\Pi D - \beta^2\Pi - \alpha^2 - i\alpha \mathrm{Re} V\Pi\Big]\Theta +$$
$$+\Big[-\xi \mathrm{Re} V\Pi - 2\mathrm{Re}V'\Pi^2 - 2\mathrm{ReRo}\Pi^2 + 2i\xi\alpha\Big]R - i\alpha\mathrm{Re}\Pi P +$$
$$+A\Phi\Bigg(\Big[4a_{rr\theta\theta}\Pi^2 D^2 + 2\xi a_{rr\theta\theta}\Pi D + 4i\alpha a_{r\theta\theta\theta}\Pi D - \alpha^2 a_{\theta\theta\theta\theta}\Big]\Theta +$$
$$+\Big[4a_{rrr\theta}\Pi^2 D^2 + 4\xi a_{rrr\theta}\Pi D + 4i\alpha a_{rr\theta\theta}\Pi D + i\xi\alpha a_{rr\theta\theta} + 2\xi a_{r\theta\theta\theta}\Pi D + i\xi\alpha a_{\theta\theta\theta\theta}\Big]R\Bigg) =$$
$$= -i\omega\mathrm{Re}\Pi^2\Theta + \mathcal{O}(\xi^2) \tag{8}$$

$$\Big[4\Pi^2 D^2 + 2\xi\Pi D - \beta^2\Pi - \alpha^2 - i\alpha\mathrm{Re}V\Pi\Big]Z +$$
$$-i\beta\mathrm{Re}\Pi^2 P + A\Phi\Big(-\beta^2 a_{zzzz}\Pi^2\Big)Z =$$
$$= -i\omega\mathrm{Re}\Pi^2 Z + \mathcal{O}(\xi^2) \tag{9}$$

$$\Big[2\Pi D + \xi\Big]R + i\alpha\Theta + i\beta\Pi Z = 0, \tag{10}$$

where:

$$\Pi = \Big(1 + \xi/2\eta\Big) \tag{11}$$
$$D = \partial/\partial\eta. \tag{12}$$

These equations can be written as an eigenvalue problem for the growth rate ω for a given set of Re, Ro, β and α.

The aspect ratio of the fibres, $r_p = 340$, and the value of the interaction coefficient, $C_l = 0.05$, have been selected in order for the effective shear viscosity to be 1.4 times greater as compared to the case without fibres. This value was chosen to match the degree of stabilisation in the experiments. In order to investigate how the addition of fibres affect the stability of the flow in more detail, the transient growth and the critical spanwise wavenumber obtained by the linear stability analysis are investigated. The transient growth is defined by;

$$G(t) = \max_{\mathbf{u}_0 \neq 0}\left(\frac{||\mathbf{u}(t)||_E^2}{||\mathbf{u}_0||_E^2}\right), \tag{13}$$

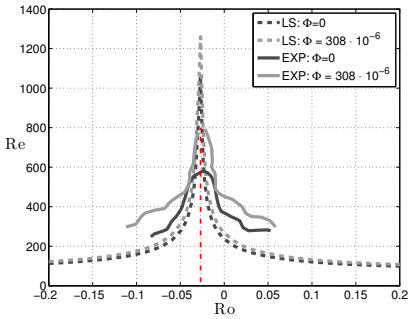

FIGURE 3. Contours of transition from laminar flow to the primary instability in the experiments (EXP) and neutral stability curve obtained by linear stability analysis (LS), for two different volume fractions of fibres. The red line indicates the location of the data used in figure 5.

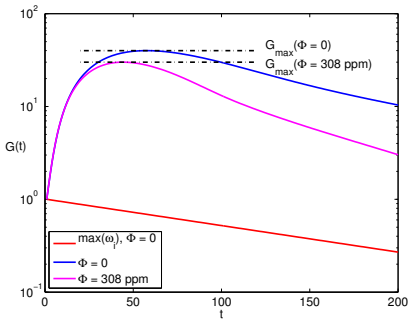

FIGURE 4. The transient growth for the case when maximum growth occurs for the two fibre volume fractions $\phi = 0$ with $\beta = 4.1$ and $\phi = 308$ ppm with $\beta = 4.3$, as well as for the most unstable mode $max(\omega_i)$, with $\phi = 0$ and $\beta = 0$, at Ro $= -0.027$ and Re $= 600$.

where u_0 is the initial condition and $u(t)$ is the disturbances at time t, obtained as a sum of eigenmodes. Due to the non-normality of the eigenmodes, $G(t)$ can grow even if all modes decay. For a more complete description of the method used to calculate the transient growth in this study, see *e.g.* Åkervik *et al.* (2008) and references therein.

4. Results and Discussion

In figure 3 the neutral stability curve obtained by linear stability analysis is shown together with the contours of the transition from laminar flow to the primary instability given by the experiments. As is evident from both the

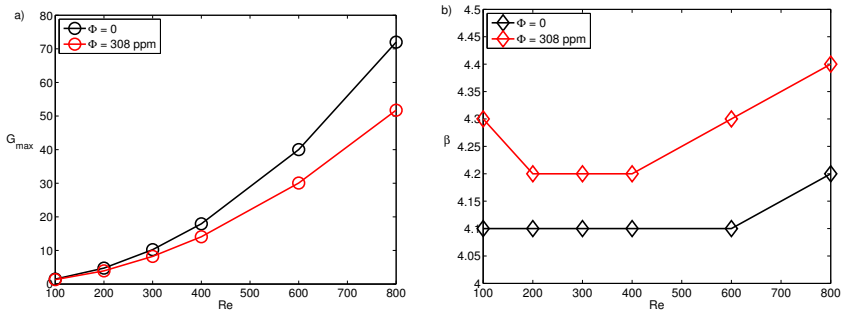

FIGURE 5. a) Maximum transient growth, G_{max}, and b) the corresponding spanwise wavenumber, β, for Ro= -0.027, along the red line given in figure 3.

experiments and the theoretical work, the presence of NFC clearly delays the transition. This delay is however not equal to the change in viscosity, which in the experiment was measured (with a rotational viscometer) to be 1.8 times larger for the NFC suspension compared to water. In relation to this, the stabilisation factor was in the experiment found to be 1.4, and in the linear stability analysis the corresponding factor is 1.2 or smaller.

The transient growth, $G(t)$, is shown in figure 4 for a few selected cases at Re = 600 and Ro= -0.027, note that the vertical axis is in log-scale. These parameters are inside the stable flow region; therefore all disturbances will decay given enough time. The straight line in the figure shows the transient growth of the eigenmodes at the most unstable eigenvalue ($\max(\omega_i)$), in this case all disturbances will decay exponentially. The other two curves are the transient growth for the two volume fractions for which the maximum transient growth occurs. In these two cases, an initial growth of the disturbances occurs due to the non-normality of the modes, followed by an exponential decay. As is clear, the maximum value of the transient growth does not take place for the same parameters as the most unstable eigenvalue.

In figure 5 the maximum transient growth and the spanwise wavenumber at which this growth occurs, are shown for several Reynolds number along a line with Ro = -0.027, corresponding to the location of the peak in the neutral stability curves in figure 3. The addition of fibres has a clear decreasing effect on the value of the maximum transient growth, as seen in figure 5 a). On the other hand, the spanwise wavenumbers at which these maximum growths occur, see figure 5 b), are almost unaffected, possibly causing complications to detect this small alteration of the wavelength in experiments. Examining figure 5 a) closer, it can be seen that the relative difference between the two cases has a value close to unity at Re = 100, indicating that at low velocities the fibres has no effect on the transient growth. As Re is increased, the relative difference between

the two curves increases, and at Re = 800 the ratio has almost reached a value of 1.4, which as mentioned earlier, is the value of effective shear viscosity of the model. This indicates that the viscosity has a larger effect on the transient growth compared to the onset of exponential growth.

In figure 6 b) - f) the maximum transient growth and its corresponding spanwise wavenumber are shown versus the rotational number for several Reynolds numbers, indicated by the lines in figure 6 a). For all Reynolds numbers, a consistent trend can be observed; when fibres are added the maximum transient growth decreases whereas the spanwise wavenumber displays a small but consistent, increase.

5. Conclusion

The addition of NFC was found to stabilise the flow both in the experiments and in the linear stability analysis. The stabilisation was in both cases found to be lower than the effective viscosity. Moreover, the results indicate that the fibres have a greater impact on the transient growth as compared to the effect of the onset of instability. In addition, a small but consistent increase was found for the spanwise wavenumber at the maximum transient growth.

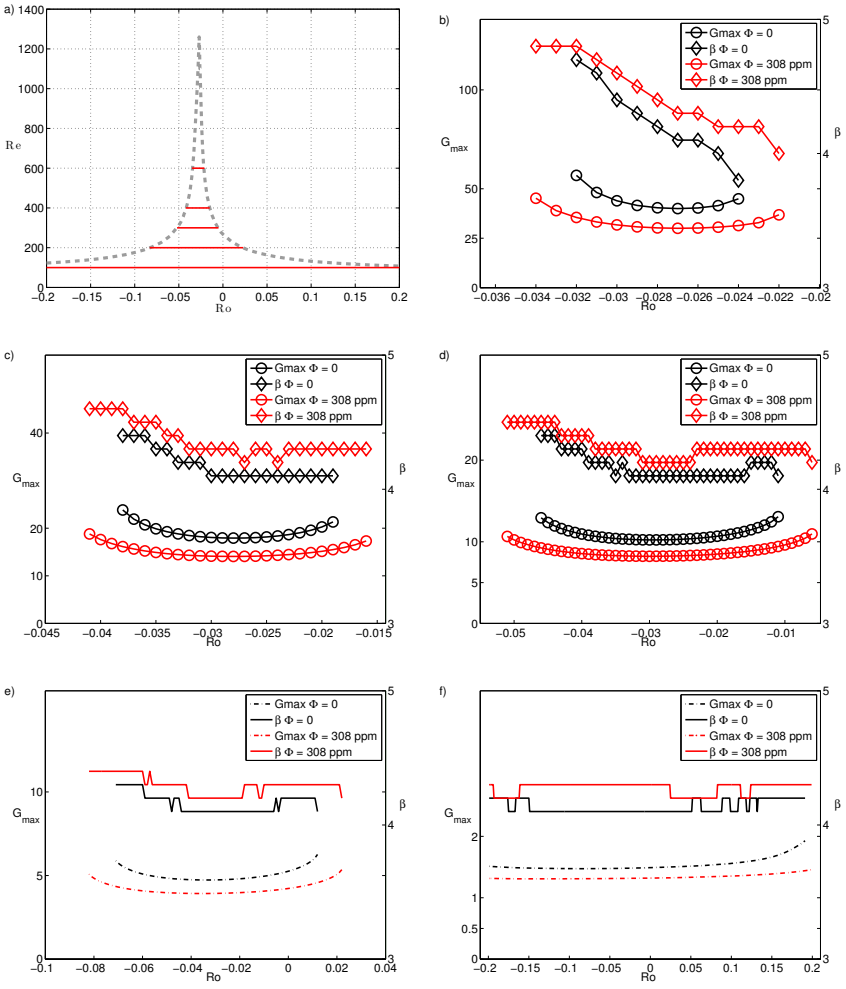

FIGURE 6. a) Location of data used in b) f) where the maximum transient growth, G_{max}, and the corresponding critical spanwise wavenumber, β, are shown for b) Re = 600, c) Re = 400, d) Re = 300, e) Re = 200 and f) Re = 100.

References

Åkervik, E., Ehrenstein, U., Gallaire, F. & Henningson, D. S. 2008 Global two-dimensional stability measures of the flat plate boundary-layer flow. *Eur J Mech B-Fluid* **27** (5), 501–513.

Azaiez, J. 2000 Linear stability of free shear flows of fibre suspensions. *J Fluid Mech* **404**, 179–209.

Batchelor, G. K. 1971 The stress generated in a non-dilute suspension of elongated particles by pure straining motion. *J Fluid Mech* **46** (04), 813–829.

Dean, W. R. 1928 Fluid motion in a curved channel. *Proc Roy Soc London A* **121** (787), 402–420.

Eichhorn, S., Dufresne, A., Aranguren, M., Marcovich, N., Capadona, J., Rowan, S., Weder, C., Thielemans, W., Roman, M., Renneckar, S., Gindl, W., Veigel, S., Keckes, J., Yano, H., Abe, K., Nogi, M., Nakagaito, A., Mangalam, A., Simonsen, J., Benight, A., Bismarck, A., Berglund, L. & Peijs, T. 2010 Review: current international research into cellulose nanofibres and nanocomposites. *J Mater Sci* **45**, 1–33.

Jeffery, G. B. 1922 The motion of ellipsoidal particles immersed in a viscous fluid. *P Roy Soc Lond A Mat* **102** (715), 161–179.

Matsson, O. J. E. & Alfredsson, P. H. 1990 Curvature- and rotation-induced instabilities in channel flow. *J Fluid Mech* **210**, 537–563.

Pääkkö, M., Ankerfors, M., Kosonen, H., Nykänen, A., Ahola, S., Österberg, M., Ruokolainen, J., Laine, J., Larsson, P. T., Ikkala, O. & Lindström, T. 2007 Enzymatic hydrolysis combined with mechanical shearing and high-pressure homogenization for nanoscale cellulose fibrils and strong gels. *Biomacromolecules* **8** (6), 1934–1941.

Pilipenko, V. N., Kalinichenko, N. M. & Lemak, A. S. 1981 Stability of the flow of a fiber suspension in the gap between coaxial cylinders. *Soviet Physics Doklady* **26**, 646.

Vaseleski, R. C. & Metzner, A. B. 1974 Drag reduction in the turbulent flow of fiber suspensions. *AIChE J* **20** (2), 301–306.

Zhenjiang, Y., Jianzhong, L. & Zhaosheng, Y. 2004 Hydrodynamic instability of fiber suspensions in channel flows. *Fluid Dyn Res* **34** (4), 251–271.

Paper 5

5

Fibre suspension flow in a plane channel: transition delay by cellulose nanofibrils

By Mathias Kvick[1,2], Kenta Watanabe[3], Makato Miyazaki[3], Masaharu Matsubara[3], Fredrik Lundell[1,2] & Daniel Söderberg[1]

[1] Wallenberg Wood Science Center, KTH Mechanics, Royal Institute of Technology, SE – 100 44, Stockholm, Sweden
[2] Linné Flow Centre, KTH Mechanics, Royal Institute of Technology, SE – 100 44, Stockholm, Sweden
[3] Department of Mechanical Systems Engineering, Shinshu University, 4-17-1, Wakasato, Nagano, 380-8553, Japan

Manuscript

The effects on the laminar-turbulent transition in a two-dimensional channel by the addition of cellulose nanofibrils (CNF) are investigated in a combined experimental and theoretical study. Pressure drop measurements, flow visualisations, linear stability- and transient growth analyses are performed for different concentrations of CNF. With the addition of CNF to the flow, the transition from laminar to turbulent flow is delayed. However, an increased concentration of CNF is in both the experiments and the theoretical analyses found to influence the critical Reynolds number more than the effective viscosity, *i.e.* the increase in critical Reynolds number is larger than predicted by the effective viscosity. In the experiments, ageing of the fibre suspensions is found to have a large impact on the measured pressure drop, with a decrease in pressure drop if the suspension was allowed to age. The transient growth analyses results in an empirical scaling of the Reynolds number for equal growth, based on the concentration of CNF. Moreover, the streamwise wavenumber for which the maximum transient growth of disturbances occurs is found to increase with increasing concentration.

1. Introduction

Cellulose nanofibrils (CNF) are the result of disintegration of paper pulp into cellulose fibrils with diameters on nano-scale and lengths of a few micrometers (Turbak *et al.* 1983). Recent advancements have lowered the cost of producing CNF, consequently, research regarding new bio-materials where CNF are one of the main constituents is a current focus (Eichhorn *et al.* 2010). Whether the goal of the material is high performance (Håkansson *et al.* 2014) or increased

functionality (Hamedi *et al.* 2014), understanding the flow behaviour of suspensions containing CNF are of great interest for processing and synthesising purposes.

Since the middle of the last century, when drag reducing effects of polymers were first explicitly published (Toms 1948) there has been an interest in flows of suspensions of elongated particles (Virk 1975; Hershey & Zakin 1967). Many studies have been performed on the reduction in pressure drop when adding polymers to a flow (White & Mungal 2008) while the prediction of the transition point has been of secondary importance (Güzel *et al.* 2009).

It is, at this point, important to distinguish between turbulent drag reduction and the drag reduction that may occur due to extension of the laminar region (Hershey & Zakin 1967), *i.e.* as a result of a delayed laminar-turbulent transition. Polymers have been found to have a stabilising effect on the transition to turbulence in pipe flow (Draad *et al.* 1998; Escudier *et al.* 1998), and coiling of the polymers was found to decrease this effect. The drag reducing ability of polymers has been explained to be due to the elasticity, while for fibres, elasticity was found to decrease the amount of drag reduction (Paschkewitz *et al.* 2004). Instead the reduction in drag was hypothesized to be due to the generation of stresses when the fibre align in an extensional region, indicating that an elasticity would only delay the time until the fibre has fully aligned with the extensional field. This also suggests that the important parameter in drag reduction is the extensional viscosity.

Experimental research in drag reduction, and the influence on transition, where fibres have been used as the additive, has raised less interest compared to polymers. The lower interest is related to the fact that to achieve the same drag reduction, a larger concentration of fibres is needed (when compared to polymers). However, the advantage of using fibres as a drag reducing additive is the comparatively low mechanical and chemical degradation (Reddy & Singh 1985). Studies using different types of macroscopic rigid fibres with different concentrations have been performed showing the importance of fibre size on drag reduction (Vaseleski & Metzner 1974) and extension of the transition region (Radin *et al.* 1975).

Regarding the effect of smaller fibres, with sizes closer to polymers, a few recent publications can be found in the literature (Krochak *et al.* 2011; Kvick *et al.* 2013*b*,*a*; Ko *et al.* 2007; Ogata *et al.* 2011). Using micro-fibrillated cellulose, Krochak *et al.* (2011) measured the pressure drop in a fully developed turbulent pipe flow. The drag reduction in the turbulent regime was found to increase with concentration and flow rate, and a maximum drag reduction of 9% was observed at an optimal concentration. Bacterial cellulose has also been tested as a drag reducing agent by Ogata *et al.* (2011), where a decrease in friction in the turbulent region was found, while in the transitional region the friction increased. Only the largest concentration (400 ppm), resulted in a

delay in transition. In fact, for concentrations less than 200 ppm, the critical Reynolds number was reduced by the addition of bacterial cellulose. Using fibres of similar scale, pressure drop measurements of the flow of a carbon nanotubes (CNT) suspension in a horizontal tube has been performed (Ko *et al.* 2007). The method used to disperse the CNT was found to have a large impact on the pressure drop, where one method resulted in the same friction factor as the control fluid and the other in an increased friction factor at laminar flow conditions and an extended laminar region, in the turbulent region no differences could be observed between the different suspensions and pure water. Kvick *et al.* (2013*b*) investigated the effect of nano-cellulose on the transition in a curved, rotating, channel. The delay in transition was compared to the measured viscosity, and it was concluded that the added fibres caused an increase in the viscosity larger than the increase in critical Reynolds number.

By linear stability analyses, the effect of fibres on transition has been modelled in several studies (Nsom 1996; Azaiez 2000; Gupta *et al.* 2002; Zhenjiang *et al.* 2004; Bark & Tinoco 1978), in all studies the addition of fibres was found to stabilise the flow. Stability analyses performed on the flow in a curved channel found the critical wavenumber to be unaffected by the fibres (and by the gap width) (Nsom 1996) while in a straight channel an increase of the streamwise wavenumber was observed (Zhenjiang *et al.* 2004). Moreover, the stabilising effect of the fibres has been suggested to be connected to the orientational diffusivity that arises from hydrodynamic interactions (Azaiez 2000; Zhenjiang *et al.* 2004). The increase in critical Reynolds number for channel flow, was by Bark & Tinoco (1978) reported to scale with the product of the volume fraction and the square of the aspect ratio of the fibres.

The effect of fibres on other growth mechanics, such as transient growth (Schmid & Henningson 2001), have to the authors knowledge never been reported. The literature on the effect of particles on transient growth is scarce, Klinkenberg *et al.* (2011) studied the influence of inertial spheres on the non-modal growth of disturbances in a channel flow. Surprisingly, an increase was found in the transient energy growth of the particle suspension when compared to the clean fluid. Furthermore, the growth was found to scale with a parameter based on the added mass fraction.

In the current study, pressure drop measurements, flow visualisations and linear transient growth analyses are performed for a channel-flow of CNF suspensions, varying flow rate and CNF-concentration. Effects on transition, drag reduction in the transitional region and the influence of ageing are investigated. In section 2 the experimental setup is explained and details regarding the fibre suspension is given. In section 3, the equations governing linear stability of the system are derived. In section 4 the results are presented, followed by discussions and conclusions in section 5.

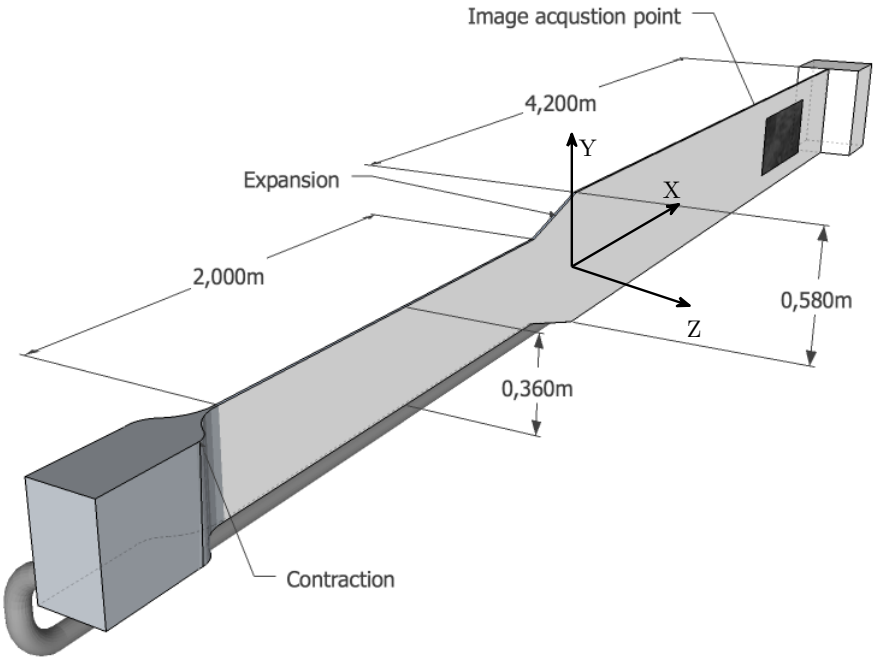

FIGURE 1. Schematic drawing of the experimental setup.

2. Method

2.1. *Experimental setup*

A schematic of the experimental apparatus is shown in Fig. 1. A pump is used to pressurise the suspension in a stagnation chamber, which, through a contraction, is connected to the channel. The main constituents of the channel are two approximately 6 m long glass plates, separated by the channel width $d = 7.1$ mm. After the contraction, a tripping wire is placed inside the channel, ensuring that the flow is fully turbulent after the 2 m long entrance section. After the entrance section the channel is expanded in the spanwise direction, the expanding section is 0.4 m long and has a divergence angle of 15° with an increase in spanwise width from 0.36 m to 0.58 m, resulting in a 62% decrease in mean velocity. Thereafter follows the 4.2 m long test section, ending in a downstream reservoir from which the fluid is pumped back to the inlet. The flow rate is measured by an orifice flow meter installed in the pipe connected to the pump, from the measured flow rate the mean velocity in the test section, $\bar{U}$, is calculated. The Reynolds number for the flow in the channel is given by:

$$\mathrm{Re} = \frac{\bar{U}d}{\nu_w}, \tag{1}$$

where ν_w is the kinematic viscosity of water. Unless otherwise stated, all Reynolds numbers given throughout the article are based on the viscosity of the suspending liquid.

At the end of the test section flow visualisations are performed. The fluid is mixed with a small amount of disc shaped pearl particles (Iriodin), and a camera is used to capture images of the structures in the flow. Images from a few selected Reynolds numbers are shown for pure water and $c_m = 400$ ppm in Fig. 2.

2.2. *Fibre Suspension*

The cellulose nanofibril (CNF) suspension is produced by disintegration of the fibres in paper pulp, in the present study this is made possible by an enzymatic pre-treatment followed by a high pressure homogenisation, as described in Pääkkö *et al.* (2007). After the disintegration, the resulting fibrils have a length of around $l \approx 2$ μm and a diameter of around 30 nm resulting in aspect ratio of $r_p \approx 70$. In the suspension used here, some large particles are still present. The manufacturing of the CNF was carried out at Innventia AB (Box 5604, SE 11486 Stockholm, Sweden), and was delivered at a mass concentration $c_m = 2\%$. The concentration was reduced stepwise using an ultrasonic homogeniser (Bandelin HD3200 with a TT13 probe), in each step the concentration was halved, down to a mass fraction of $c_m = 0.1\%$. In each homogenisation step, energy of approximately 300 MJ/(kg water) was used. After having reached $c_m = 0.1\%$ the suspension was further diluted by adding water and mixing. The concentrations can also be written as the more relevant parameter $nl^3 = 0.3 - 2.7$, where n is the number density per unit volume. The suspension is thus in the semidilute regime, where fibres collide with each other but do not form networks Kerekes (2006).

Measurements of the viscosity of the CNF suspensions were carried out at the Department of Food Technology, Nagano Prefectural Industrial Technology Center. The dynamic viscosity μ as a function of shear rate, $\dot{\gamma}$, is in Fig. 3 shown for two of the suspensions used in the experiments, the viscosity was measured using both a parallel plate geometry (PP) and concentric cylinders (CC).

Measuring viscosity of a CNF suspension is not trivial. Saarinen *et al.* (2014) measured the concentration- and velocity distributions of a microfibrillated cellulose suspension using optical coherence tomography during viscosity measurements in a rotational viscometer. Wall depletion was found play an important roll in the measured viscosity and the shear thinning behaviour was closely related to the structural changes of the fibril flocs. It is at the moment

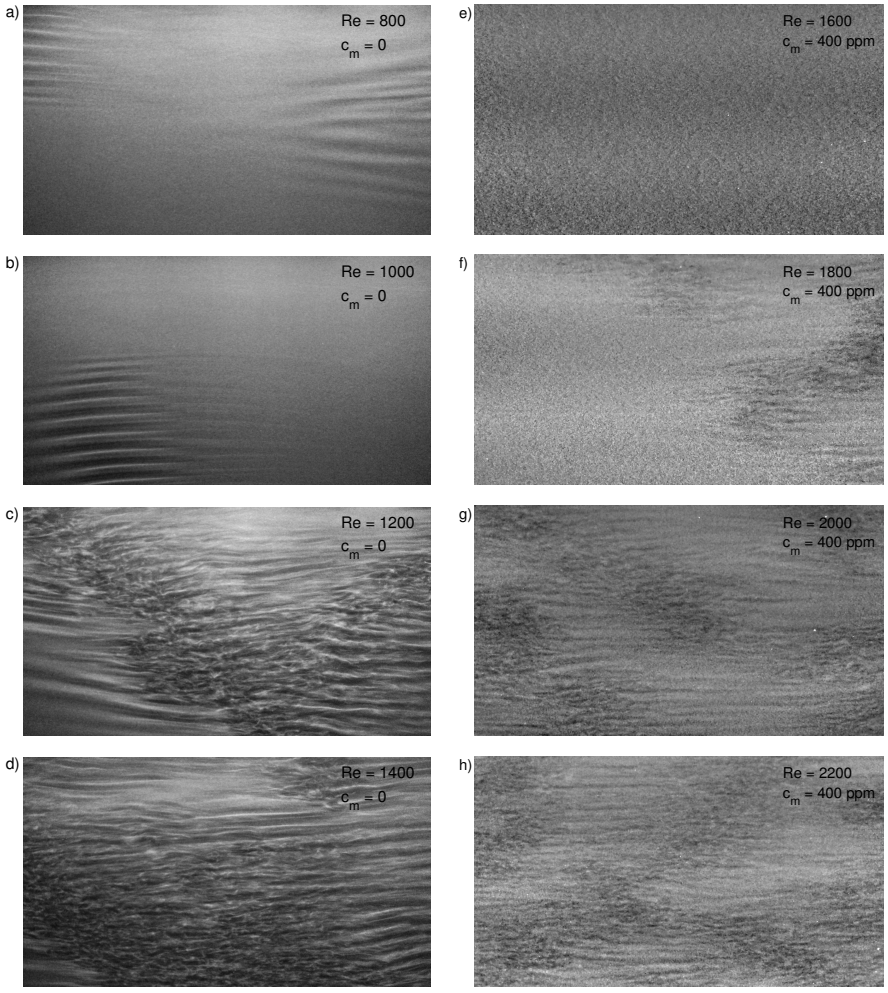

FIGURE 2. Flow visualisation for a)-d) water at Re= 800, b) Re= 1000, c) Re= 1200, d) Re= 1400 and e)-h) $c_m = 400$ ppm CNF at Re= 1600, b) Re= 1800, c) Re= 2000, d) Re= 2200.

debatable, to what extent traditional viscosity measurements of fibre suspensions can be used as a basis to predict flow dynamics.

2.3. *Pressure drop*

In order to measure the static pressure in the channel, a 90 mm long pipe, with diameter 2.1 mm was used. Four 0.5 mm pressure holes on the pipe are located 32 mm downstream of the tip in an axis symmetric configuration.

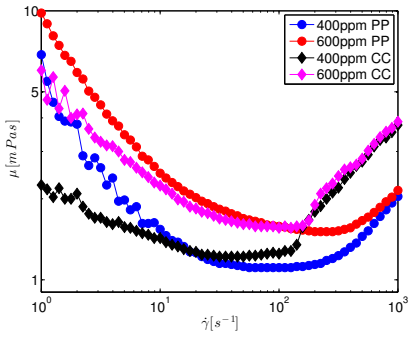

FIGURE 3. Viscosity as a function of shear rate for two of the concentrations using parallel plate geometry (PP) and concentric cylinders (CC).

The static tube was connected to a pressure transducer through a 2.5 m long aluminium tube with diameter 7.1 mm. In Fig. 4a, a schematic of the pressure measurement system and the locations of the measurement points are shown. As depicted in Fig. 4a, the pressure tube was inserted through the downstream reservoir in order to limit the blockage. The pressure was measured at locations separated by a distance $\Delta x = 0.3$ m, starting at $x = 3.0$ m. From the pressure drop measurements, the wall shear stress is calculated from:

$$\tau_w = \frac{d}{2}\frac{\partial p}{\partial x}, \tag{2}$$

resulting in the non-dimensional friction coefficient:

$$C_f = \frac{\tau_w}{\frac{1}{2}\rho_w \bar{U}^2}, \tag{3}$$

where ρ_w is the water density. Due to the small amount of CNF added the density of the suspension will deviate only slightly from the water density, and will not have any noticeable influence on the friction coefficient.

The linearity of the pressure drop is illustrated in Fig. 4b, where the relative pressure is shown for four different concentrations at three Reynolds numbers as a function of the streamwise location. By fitting a line to the measured data, using the least squares method, the pressure gradient is obtained.

3. Linear stability theory

In order to investigate if a simple model is enough to predict the effect of the addition of fibres on transition, a linear stability analysis if performed where the effect of the fibres are modelled by an orientation dependent stress tensor.

The incompressible flow of pure water in the channel is governed by the mass- and momentum-conservation equations:

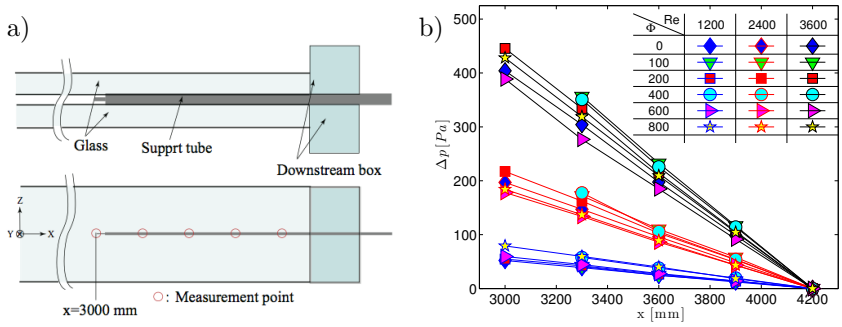

FIGURE 4. a) Streamwise positioning of the static pressure tube and b) streamwise pressure difference for selected concentrations and Reynolds numbers.

$$\frac{\partial u_i^*}{\partial t^*} + u_j^* \frac{\partial u_i^*}{\partial x_j^*} = -\frac{1}{\rho}\frac{\partial p^*}{\partial x_i^*} + \nu \frac{\partial^2 u_i^*}{\partial x_j^* \partial x_j^*} \tag{4}$$

$$\frac{\partial u_i^*}{\partial x_i^*} = 0, \tag{5}$$

where ρ is the fluid density and star (*) indicate dimensional values, the velocity vector is given by:

$$\mathbf{u}^* = u^* \mathbf{e_x} + v^* \mathbf{e_y} + w^* \mathbf{e_z}. \tag{6}$$

A decomposition of the flow is made into its mean parts (U and $\mathcal{P}$) and small disturbances denoted by "$'$":

$$\mathbf{U} = (U + u'^*, v'^*, w'^*) \tag{7}$$

$$p = \mathcal{P} + p'^*. \tag{8}$$

The dimensionless form of the equations are obtained by using the following scalings:

$$u_i = \frac{u_i^*}{U} \tag{9}$$

$$p = \frac{p^*}{\rho U^2} \tag{10}$$

$$t = \frac{t^*}{d/U} \tag{11}$$

$$x_i = \frac{x_i^*}{d}. \tag{12}$$

If disturbances are assumed to be of the form:

$$(u', v', w', p') = (X(y), Y(y), Z(y), P(y))e^{i(\alpha x + \beta z - \omega t)}, \tag{13}$$

where α and β are the streamwise and spanwise wavenumbers and ω is the temporal growth rate, the linear stability equation can be obtained. By introducing Eq. (13) into (5), subtracting the mean flow, linearising the equations and making them non-dimensional, the following set of equations describing the stability of the system when subjected to small disturbances are obtained (see *e.g.* Reddy *et al.* (1993)):

$$\left[i\alpha U - \frac{1}{Re}\left(D^2 - \alpha^2 - \beta^2\right)\right]X + U'Y + i\alpha P = i\omega X \tag{14}$$

$$\left[i\alpha U - \frac{1}{Re}\left(D^2 - \alpha^2 - \beta^2\right)\right]Y + DP = i\omega Y \tag{15}$$

$$\left[i\alpha U - \frac{1}{Re}\left(D^2 - \alpha^2 - \beta^2\right)\right]Z + i\beta P = i\omega Z \tag{16}$$

$$i\alpha X + DY + i\beta Z = 0, \tag{17}$$

where $D = \partial/\partial y$. Solving this eigenvalue problem for a given set of (Re, α, β) results in a complex ω together with eigenfunction X, Y and Z, where a positive imaginary part of ω means growth of the corresponding small disturbance. The real part of ω provides the frequency of the disturbance.

3.1. *Modelling of fibres*

The addition of fibres is modelled as an additional stress tensor (Batchelor 1970; Shaqfeh & Fredrickson 1990; Ericksen 1960; Lipscomb II *et al.* 1988):

$$\frac{\partial u_i^*}{\partial t^*} + u_j^*\frac{\partial u_i^*}{\partial x_j^*} = -\frac{1}{\rho}\frac{\partial p^*}{\partial x_i^*} + \nu\frac{\partial^2 u_i^*}{\partial x_j^* \partial x_j^*} + \frac{\partial \sigma_{ij}^f}{\partial x_j^*} \tag{18}$$

$$\frac{\partial u_i^*}{\partial x_i^*} = 0, \tag{19}$$

where the fibre induced stress is given by (Batchelor 1970; Leal & Hinch 1973):

$$\sigma^f = \nu\Phi[Q(\boldsymbol{\varepsilon} : \mathbf{a_4}) + R(\boldsymbol{\varepsilon} \cdot \mathbf{a_2} + \mathbf{a_2} \cdot \boldsymbol{\varepsilon}) + S\boldsymbol{\varepsilon} + \mathbf{T}\mathbf{a_2}], \tag{20}$$

where Q, R, S and $\mathbf{T}$ are rheological parameters, $\Phi = c_m\rho_f$ is the volume fraction with $\rho_f = \rho_w/\rho_{CNF}$ being the relative density, $\boldsymbol{\varepsilon}$ is the strain rate tensor, " : " denotes the double dot product and $\mathbf{a_4} =< \mathbf{pppp} >$ and $\mathbf{a_2} =< \mathbf{pp} >$ are the fourth and second order orientation tensor for the fibrils ($\mathbf{p}$ is the orientation vector and $< ... >$ denotes the ensemble average (Advani & Tucker III 1987)).

The rheological parameters are of the order (Batchelor 1971; Phan-Thien & Graham 1991; Petrie 1999):

$$Q \sim r_p^2 \tag{21}$$

$$R \sim r_p^{-2} \tag{22}$$

$$S = 2 \tag{23}$$

$$\mathbf{T} \sim D_r r_p^2, \tag{24}$$

where D_r is the rotational diffusivity and r_p is the aspect ratio of the fibres. Due to the large aspect ratio of the fibres and the small rotational diffusion (Håkansson *et al.* 2014), a simplification of the fibre induced stress is possible by neglecting R, S and $\mathbf{T}$. Finally, the extra stress is given by:

$$\sigma^f = \nu\Phi Q(\boldsymbol{\varepsilon} : \mathbf{a_4}). \tag{25}$$

Only the deviatoric part of the stress is of interest and the extra stress takes the following form:

$$\begin{aligned}\sigma_{ij}^f =& \nu Q\Phi(a_{ijkl} - \frac{1}{3}\delta_{ij}a_{kl})\varepsilon_{kl} = \\ =& \nu Q\phi[\varepsilon_{xx}(a_{xxij} - \frac{1}{3}\delta_{ij}a_{xx}) + 2\varepsilon_{xy}(a_{xyij} - \frac{1}{3}\delta_{ij}a_{xy}) + \varepsilon_{yy}(a_{yyij} - \frac{1}{3}\delta_{ij}a_{yy}) + \\ &+ 2\varepsilon_{xz}(a_{xzij} - \frac{1}{3}\delta_{ij}a_{xz}) + 2\varepsilon_{yz}(a_{yzij} - \frac{1}{3}\delta_{ij}a_{yz}) + \varepsilon_{zz}(a_{zzij} - \frac{1}{3}\delta_{ij}a_{zz})].\end{aligned} \tag{26}$$

The expression for the rheological parameter Q is for a semi-dilute suspension given by (Batchelor 1971):

$$Q = \frac{r_p^2}{3\ln(\sqrt{2\pi/\Phi})}. \tag{27}$$

The final equations describing the linear stability of the channel flow of a fibre suspension are:

$$\left[i\alpha U - \frac{1}{Re}(D^2-\beta^2-\alpha^2)\right]X + U'Y + i\alpha P - \frac{1}{Re}Q\Phi\left\{A_xX + A_yY + A_zZ\right\} = i\omega X \tag{28}$$

$$\left[i\alpha U - \frac{1}{Re}(D^2-\beta^2-\alpha^2)\right]Y + DP - \frac{1}{Re}Q\Phi\left\{B_xX + B_yY + B_zZ\right\} = i\omega Y \tag{29}$$

$$\left[i\alpha U - \frac{1}{Re}(D^2-\beta^2-\alpha^2)\right]Z + i\beta P - \frac{1}{Re}Q\Phi\left\{C_xX + C_yY + C_zZ\right\} = i\omega Z \tag{30}$$

$$i\alpha X + DY + i\beta Z = 0, \tag{31}$$

where:

$$\begin{aligned}
A_{x_i} =& -\alpha^2(a_{xxxx_i} - \frac{1}{3}a_{xx_i}) + i\alpha D(a_{xxyx_i} - \frac{1}{3}a_{y_i}) - \alpha\beta(a_{xxzx_i} - \frac{1}{3}a_{zx_i}) + \\
& i\alpha D a_{xxyx_i} + D^2 a_{xyyx_i} + i\beta D a_{xyzx_i} - \alpha\beta a_{xxzx_i} + i\beta D a_{xyzx_i} - \beta^2 a_{xzzx_i} \\
B_{x_i} =& -\alpha^2 a_{xxyx_i} + i\alpha D a_{xyyx_i} - \alpha\beta a_{xyzx_i} + i\alpha D(a_{xyyx_i} - \frac{1}{3}a_{xx_i}) + \\
& D^2(a_{yyyx_i} - \frac{1}{3}a_{yx_i}) + i\beta D(a_{yyzx_i} - \frac{1}{3}a_{zx_i}) - \alpha\beta a_{xyzx_i} + \\
& i\beta D a_{yyzx_i} - \beta^2 a_{yzzx_i} \\
C_{x_i} =& -\alpha^2 a_{xxzx_i} + i\alpha D a_{xyzx_i} - \alpha\beta a_{xzzx_i} + i\alpha D a_{xyzx_i} + D^2 a_{yyzx_i} + \\
& i\beta D a_{yzzx_i} - \alpha\beta(a_{xzzx_i} - \frac{1}{3}a_{xx_i}) + i\beta D(a_{yzzx_i} - \frac{1}{3}a_{yx_i}) - \\
& \beta^2(a_{zzzx_i} - \frac{1}{3}a_{zx_i}).
\end{aligned}$$

This eigenvalue problem is descretized on a Chebyshev-collocated grid with $N = 192$ grid points Weideman & Reddy (2000), resulting in changes of the eigenvalues of less than 10^-4. The code is validated for single phase against results given by Orszag (1971) and Schmid & Henningson (2001).

When calculating the orientation tensor a closure problem arises: to calculate the fourth order tensor, $\mathbf{a_4}$, the sixth order tensor, $\mathbf{a_6}$, is required, and so on for higher orders. There exist several different closure approximations, the quadratic, linear and hybrid approximations have been summarised by Petrie (1999). In the current study the closure problem is avoided by assuming a constant fibre orientation distribution. The orientation of a fibre in the suspension is described by the orientation-vector with components:

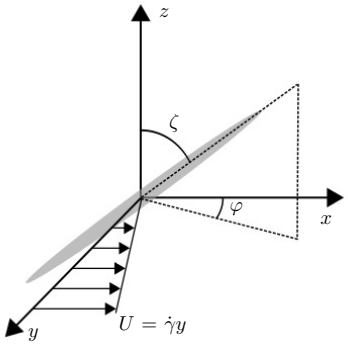

FIGURE 5. Fibre in coordinate system.

$$p_x = \sin\zeta \sin\varphi \tag{32}$$

$$p_y = \sin\zeta \cos\varphi \tag{33}$$

$$p_z = \cos\zeta, \tag{34}$$

where ζ and φ describe the fibre orientation as described in Fig. 5.

In the calculation of the fibre orientation distribution, it is assumed that all fibres are in the flow-gradient plane ($\zeta = \pi/2$) and perform orbits as described by Jeffery (1922), resulting in $p_z = 0$ and $\sin\zeta = 1$. The angular velocity of the fibres in the plane is given by:

$$\dot{\varphi} = -\frac{\dot{\gamma}}{r_p^2 + 1}(r_p^2 \sin^2\varphi + \cos^2\varphi), \tag{35}$$

Once the angular velocity is known, the fibre orientation distribution can be found by solving the Smoluchowski equation(Doi & Edwards 1986):

$$\frac{\partial}{\partial\varphi}(\dot{\varphi}\Psi - C_l|\dot{\gamma}|\frac{\partial\Psi}{\partial\varphi}) = 0, \tag{36}$$

where C_l is a coefficient modelling the interaction between the fibres. Note that in order for the modelled suspension to be shear thinning, C_l would need to depend on $\dot{\gamma}$, which is not assumed here.

The interaction coefficient and the aspect ratio are chosen as $C_l = 0.05$ and $r_p = 340$ based on previous work (Kvick *et al.* 2013*b*,*a*).

Furthermore, the constant, theoretical, effective viscosity of the suspension (μ_{LS}) can be calculated as:

$$\mu_{LS} = 1 + Q\Phi a_{xxyy}. \tag{37}$$

The viscosity will later be used in comparison of the scaling of the critical Reynolds number.

3.2. *Transient Growth*

The solution of the eigenvalue problem presented in the previous section results, above a certain critical Reynolds number, in an exponential growth. It is however well known that the transition to turbulence of the flow in a channel is subcritical and occurs well below the critical Reynolds number obtained by the linear stability analysis. Due to non-orthogonality of the eigenmodes, an initial amplification of disturbances is possible even when the disturbances decay exponentially by themselves. This amplification may then lead to self-sustained turbulence.

From the solution of the linearised, discretised eigenvalue problem, the obtained eigenfunctions are used to calculate the amplification in time (Åkervik *et al.* 2008) as:

$$G(t) = \max\left(\frac{||\mathbf{u}(t)||_E^2}{||\mathbf{u}_0(t)||_E^2}\right), \tag{38}$$

where $\mathbf{u}_0(t)$ is the initial condition and $\mathbf{u}(t)$ is the disturbances at time t, obtained as a sum of eigenmodes:

$$\mathbf{u}(t) = \sum_{l=1}^{N} \kappa_l(t)\tilde{\mathbf{u}}_l, \tag{39}$$

where $\tilde{\mathbf{u}}_l$ is the velocity field associated with each eigenmode and κ are components in the vector $\mathbf{k}$ given by:

$$\frac{d\mathbf{k}}{dt} = \mathbf{\Lambda}\mathbf{k}, \qquad \mathbf{k}(0) = \mathbf{k}_0, \tag{40}$$

where $\mathbf{\Lambda}$ is a diagonal matrix containing all the eigenvalues. More practically, the largest growth at a certain time is given by the largest singular value of the term $Fe^{\Lambda t}F^{-}1$, where F is the Cholesky factorization of the energy matrix $M = K^T\Delta K$ where K is a matrix containing all the eigenfunctions and Δ is the distance between the Chebyshev nodes. Furthermore, the maximum transient growth will be used to investigate the effect of the fibres:

$$G_{max} = \max_t G(t). \tag{41}$$

The maximum transient growth, G_{max}, will be used to define a Reynolds number of equal growth for different fibre concentrations.

4. Results

4.1. *Pressure drop*

The friction coefficient obtained from the pressure drop measurements are shown in Fig. 6 for all concentrations. The solid lines in the figure are given by (Patel & Head 1969):

$$\text{Low Re:} \qquad C_f = \frac{12}{Re}, \tag{42}$$

$$\text{High Re:} \qquad C_f = 0.0376 Re^{-1/6}. \tag{43}$$

As is evident, an increase in concentration causes the curve to be shifted to larger Reynolds number in the laminar regime, maintaining its slope. This shift can be used as a measure of the effective laminar viscosity of the suspension in the experiment itself (μ_{exp}). This definition of the viscosity will be used throughout the remainder of the study. After the linear laminar region follows a transitional region, starting at the point where the friction coefficient has a minimum, and finally the turbulent regime is reached. For the three lowest concentrations (Fig. 6a) the viscosity increases and the minimum value of the friction coefficient (C_f^{min}) decreases in an expected manner. For the two largest concentrations (Fig. 6b) the results are more difficult to interpret. The viscosity of the $c_m = 600$ ppm suspension is of the same order as the one for $c_m = 400$ ppm, in terms of C_f^{min} there appears to be an optimal concentration at $c_m = 600$ ppm.

Since cellulose is a biological material, it will experience degradation when exposed to oxygen, sunlight and heat. In order to get a glimpse on the effect this degradation has on the flow, experiments with two different batches (S1 & S2) were performed at time periods separated by a few weeks, the results are presented in Fig. 7. Curiously the effect of ageing is different depending on if it takes place before or after the dilution process described in section 2.2. Ageing the suspension before the dilution seems to increase the viscosity and the friction coefficient, while ageing in the diluted state causes a decrease in C_f while maintaining the viscosity.

4.2. *Transient Growth*

Since Squire's theorem (Schmid & Henningson 2001), stating that 2D disturbances are always more unstable than 3D disturbances, has never been proven for fibre suspensions a few tests are performed in order to test the validity of running 2D calculations where one of the wavenumber are set to zero. In Fig. 8a the growth ω_i is shown as a function of the spanwise wavenumber β with $c_m = 800$ ppm and $\alpha = 1$ for three different Reynolds numbers. As can be seen in Fig. 8a, the largest growth is reached when the spanwise wavenumber is set to zero. How the streamwise wavenumber affect the transient growth

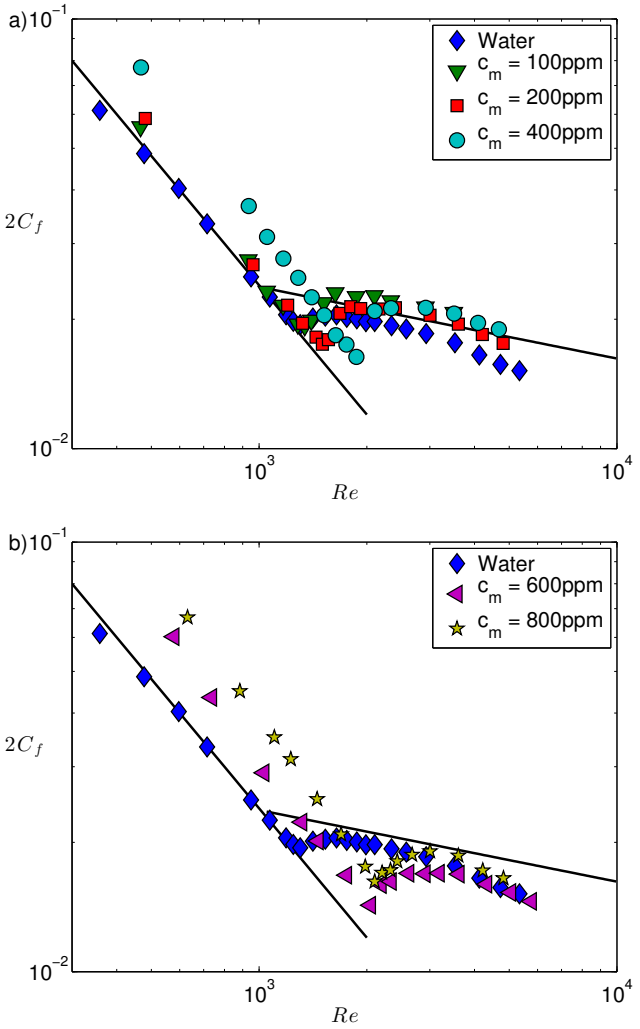

FIGURE 6. Friction coefficients of all concentrations of CNF versus Reynolds number.

is shown in Fig 8b, where the variation of the amplification (G_{max} defined in Eq. 41) for $c_m = 800$ ppm and $\beta = 2.3$ is shown. It is clear that Squire's theorem is not longer valid in this case, since larger amplification occurs for non-zero streamwise wavenumbers. All calculations considering the transient growth is therefore performed varying both α and β.

For completeness, the neutral stability curves for the investigated cases are shown in Fig. 9a. However, it is well known that transition to turbulence

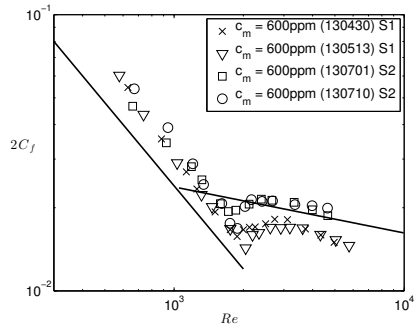

FIGURE 7. Friction coefficients for $c_m = 600$ ppm CNF, the different measurements are performed with two different batches, and time has passed between the measurements for each batch.

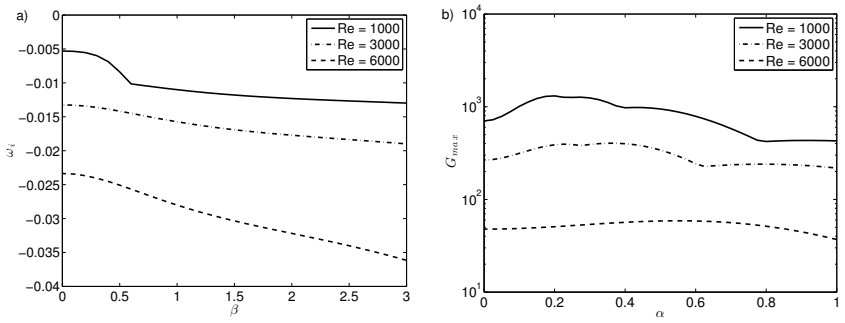

FIGURE 8. a) Growth rate as a function of the spanwise wavenumber with $c_m = 800$ ppm and $\alpha = 1$ and b) maximum amplification as a function the the streamwise wavenumber with $c_m = 800$ ppm and $\beta = 2.3$.

occurs at much lower Reynolds numbers than predicted by the linear stability analysis. Instead, the initial amplification of disturbances is of interest and is believed to be the reason for the transition (Trefethen *et al.* 1993). The transient growth and decay, for a selected parameter set, is shown in Fig. 9b.

The maximum amplification of an initial condition, obtained from the linear stability analysis, is given in Fig. 10a as a function of Reynolds number. As expected, the amplification is attenuated by the presence of the fibres, with a larger reduction for larger Reynolds numbers.

In order to investigate how the amplification scales with concentration the Reynolds number has in Fig. 10b been scaled by $m\mathrm{Re}^k$, where m and k are given by:

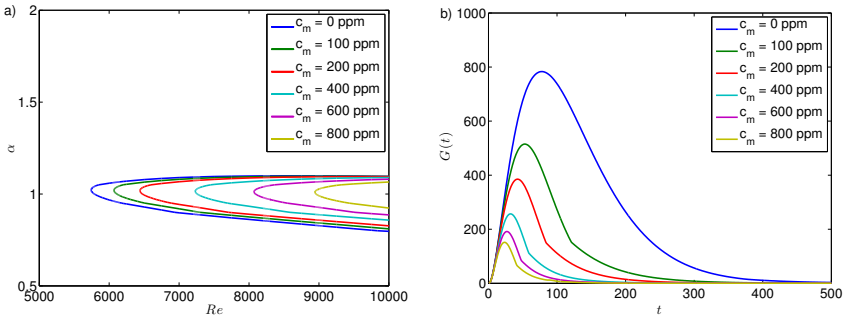

FIGURE 9. a) Neutral stability curves for the investigated concentrations. b) Transient growth for Re= 1000, $\alpha = 0$, $\beta = 2$ with varying concentration.

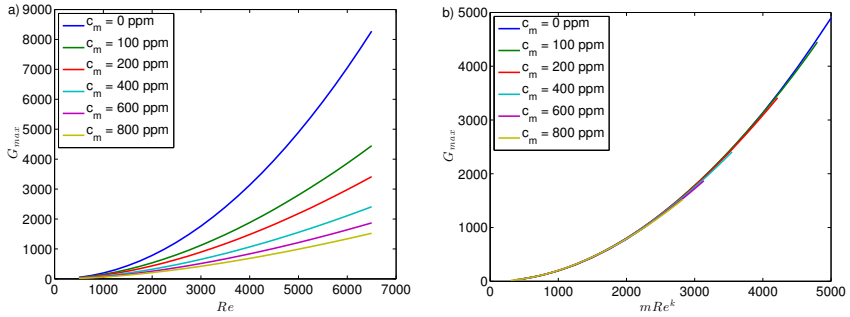

FIGURE 10. a) Maximum transient growth from the linear stability analysis for different concentrations, in b) the Reynolds number has been scaled with $m\mathrm{Re}^k$.

$$m = b_{m1}\left(\frac{r_p^2}{Q}\right)^2 + b_{m2}\left(\frac{r_p^2}{Q}\right) + b_{m3} \tag{44}$$

$$k = b_{k1}\left(\frac{r_p^2}{Q}\right)^2 + b_{k2}\left(\frac{r_p^2}{Q}\right) + b_{k3}, \tag{45}$$

with:

$$(b_{m1}, b_{m2}, b_{m3}) = (0.002289, -0.05606, 1.205) \tag{46}$$

$$(b_{k1}, b_{k2}, b_{k3}) = (-0.06506, 2.068, -14.77), \tag{47}$$

resulting in a collapse of the curves.

In Fig. 11 the spanwise (β_{max}) and streamwise (α_{max}) wavenumbers where the maximum amplification is reached is shown for each Reynolds number.

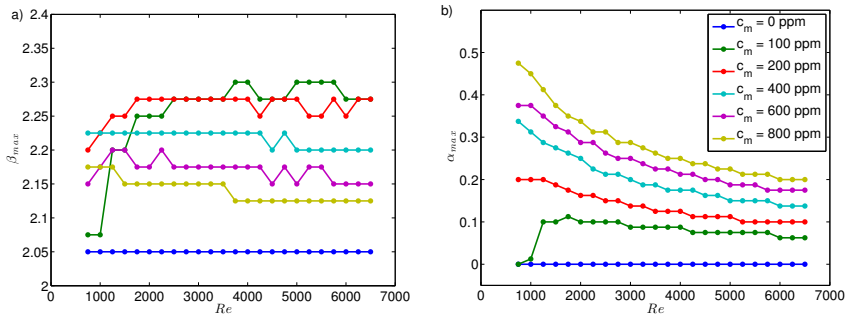

FIGURE 11. a) Spanwise and b) streamwise wavenumbers for which the maximum amplification occurs. The legend for both figures are given in b).

Without fibres the wavenumbers are constant independent of the Reynolds number while with fibres variations can be seen. The fibres have a more clear effect on the streamwise wavenumber, where an increase in α_{max} is seen with increasing concentration. In addition, with increased fibre concentration, an increased variation is seen in Reynolds number, appearing to approach a constant value at higher Re.

4.3. *Critical Re comparison*

The results from the experiment and the linear stability analysis is summarised in table 4. The theoretical effective viscosity (μ_{LS}) is calculated using Eq. 37 and the experimental relative viscosity (μ_{EXP}) is obtained by fitting the pressure drop data in the laminar regime to the Newtonian curve. The critical Reynolds numbers are in the linear stability (Re_{cr}^{LS}) given by the minimum value at which exponential growth takes place, in the transient growth (Re_{300}^{TG}) the Reynolds number where a maximum growth of $G_{max} = 300$ occurs, and in the experiments (Re_{cr}^{EXP}) the Reynolds number where the pressure drop deviates from the laminar curve is used. The minimum friction coefficient (C_f^{min}) and the maximum drag reduction (DR_{max}) are both results from the pressure drop data.

At a glance, the maximum drag reduction given in the table looks quite impressive with a peak value of 30%. However, this drag reduction only occurs in a narrow range in Reynolds numbers in the transitional regime.

Scaling the critical Reynolds numbers with the effective viscosity could, if the effects of fibres are isotropic result in a constant critical Reynolds number independent of concentration. As evident from Fig. 12, where the critical Reynolds numbers have been scaled with the effective viscosity, this is not the

ϕ[ppm]	nl^3	μ_{LS}	Re_{cr}^{LS}	Re_{300}^{TG}	μ_{EXP}	Re_{cr}^{EXP}	C_f^{min}	$DR_{max}[\%]$
0	0	1	5745	1250	1	1303	0.0097	0
100	0.3	1.04	6070	1450	1.05	1341	0.0097	1
200	0.7	1.09	6500	1600	1.09	1502	0.0088	12
400	1.3	1.20	7235	2000	1.30	1871	0.0082	18
600	2.0	1.31	8200	2200	1.23	2046	0.0072	30
800	2.7	1.43	8950	2400	1.48	2105	0.0081	18

TABLE 4. Summary of the results from the experiments (EXP), linear stability analysis (LS) and transient growth analysis (TG). The variables are explained in detail in the text.

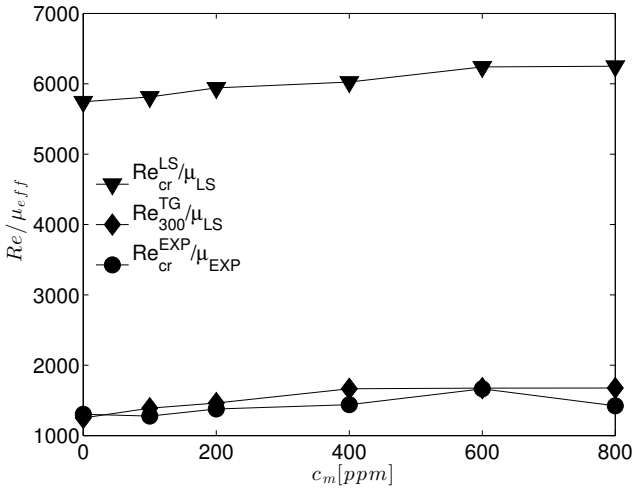

FIGURE 12. Critical Reynolds numbers scaled with the effective viscosity. Re_{cr}^{LS} is the minimum value at which exponential growth is found, Re_{300}^{TG} is the Reynolds number where a maximum amplification of $G_{max} = 300$ occurs and Re_{cr}^{EXP} is the Reynolds number at which the pressure drop curves deviate from the laminar line.

case. All scaled critical Reynolds numbers increase with concentration, indicating that delay in transition is larger than the effect on the viscosity.

5. Discussion & Conclusion

Channel flow experiments and linear transient growth analyses of cellulose nanofibril suspensions have been performed. Pressure drop measurements, flow

visualisations and predicted disturbance growth are presented. In order to provide a well-defined flow case, the flow channel consists of a first, high Re section followed by an expansion, where Re is decreased, before the straight test section. This design makes it possible to study transitional flow without hysteresis.

The main conclusions in this study are:

- Transition is delayed by addition of CNF.
- Critical Reynolds number is increased more than expected from the increase in viscosity.
- An increase in critical wavenumber was found in the transient growth analysis.
- Ageing can have a large impact on the pressure drop.
- A scaling for the maximum transient growth is obtained.

Onset of laminar/turbulent transition, defined as the departure from the laminar pressure drop curve, was delayed by the addition of CNF. The delay grew with increased CNF concentration. It is also indicated that the transition was delayed even further, without a corresponding increase in viscosity, if the suspension was left to age without stirring for a time on the order of weeks.

The increase in critical Re was always larger than the increase in laminar viscosity, as could be determined from the pressure loss in the laminar region. This is in agreement with the transient growth analysis, where the growth was found to scale by $m\mathrm{Re}^k$, where m and k are functions of r_p^2/Q. This scaling is in no way definitive, further variations of parameters need to be included in order to find out if a physically relevant scaling exists. Moreover, the streamwise wavenumber is increased with concentration.

A consequence of the transition delay is a distinct (more than 30%) drag reduction for transitional flow. The mechanisms determining the extent of the region (in terms of Reynolds number) are (i) the laminar viscosity increase (ii) the attenuated disturbance growth and (iii) the modified dynamics in the turbulent flow. The latter phenomenon has not been pursued in this work. The competition between the first two mechanisms implies that there is an optimal concentration for a given Reynolds number. In this context, ageing effects complicates optimisation.

There are two ways in which these results can be approached. The first is to view CNF as a possible flow additive that can be used to obtain improved processing or transporting properties of fluids, in particular reduced pumping power or increased flow rate at constant power. It should be stressed, however, that CNF is also a highly interesting building block for future biomaterials (Eichhorn *et al.* 2010) and in this context, it is clear that fluid physics of CNF suspensions is a crucial factor in the design of innovative processes for nanostructured high-performance or functional biomaterials (Hamedi *et al.* 2014; Håkansson *et al.* 2014).

References

Advani, S. G. & Tucker III, C. L. 1987 The use of tensors to describe and predict fiber orientation in short fiber composites. *J. Rheol.* **31** (8), 751–784.

Åkervik, E., Ehrenstein, U., Gallaire, F. & Henningson, D. S. 2008 Global two-dimensional stability measures of the flat plate boundary-layer flow. *Eur. J. Mech. B-Fluids* **27** (5), 501–513.

Azaiez, J. 2000 Linear stability of free shear flows of fibre suspensions. *J. Fluid Mech.* **404**, 179–209.

Bark, F. H. & Tinoco, H. 1978 Stability of plane Poiseuille flow of a dilute suspension of slender fibres. *J. Fluid Mech.* **87**, 321–333.

Batchelor, G. K. 1970 The stress system in a suspension of force-free particles. *J. Fluid Mech.* **41** (03), 545–570.

Batchelor, G. K. 1971 The stress generated in a non-dilute suspension of elongated particles by pure straining motion. *J. Fluid Mech.* **46** (04), 813–829.

Doi, M. & Edwards, S. F. 1986 *The Theory of Polymer Dynamics*. Oxford University Press.

Draad, A. A., Kuiken, G. D. C. & M., N. T. 1998 Laminar-turbulent transition in pipe flow for Newtonian and non-Newtonian fluids. *J. Fluid Mech.* **377**, 267–312.

Eichhorn, S., Dufresne, A., Aranguren, M., Marcovich, N., Capadona, J., Rowan, S., Weder, C., Thielemans, W., Roman, M., Renneckar, S., Gindl, W., Veigel, S., Keckes, J., Yano, H., Abe, K., Nogi, M., Nakagaito, A., Mangalam, A., Simonsen, J., Benight, A., Bismarck, A., Berglund, L. & Peijs, T. 2010 Review: current international research into cellulose nanofibres and nanocomposites. *J. Mater. Sci.* **45**, 1–33.

Ericksen, J. 1960 Transversely isotropic fluids. *Colloid Polym. Sci.* **173**, 117–122.

Escudier, M., Presti, F. & Smith, S. 1998 Drag reduction in the turbulent pipe flow of polymers. *J. Non-Newton Fluid* **81** (3), 197–213.

Gupta, V. K., Sureshkumar, R., Khomami, B. & Azaiez, J. 2002 Centrifugal instability of semidilute non-Brownian fiber suspensions. *Phys. Fluids* **14** (6), 1958–1971.

Güzel, B., Frigaard, I. & Martinez, D. M. 2009 Predicting laminar-turbulent transition in Poiseuille pipe flow for non-Newtonian fluids. *Chem. Eng. Sci.* **64** (2), 254–264.

Håkansson, K. M. O., Fall, A. B., Lundell, F., Yu, S., Krywka, C., V., R. S., Santoro, G., Kvick, M., Prahl Wittberg, L., Wågberg, L. & Söderberg, L. D. 2014 Hydrodynamic alignment and assembly of nanofibrils resulting in strong cellulose filaments. *Nat. Commun.* **5**, 4018.

Hamedi, M. M., Hajian, A., Fall, A. B., Håkansson, K., Salajkova, M., Lundell, F., Wågberg, L. & Berglund, L. A. 2014 Highly conducting, strong nanocomposites based on nanocellulose-assisted aqueous dispersions of single-wall carbon nanotubes. *ACS Nano* **8** (3), 2467–2476.

Hershey, H. C. & Zakin, J. L. 1967 Existence of two types of drag reduction in pipe flow of dilute polymer solutions. *Ind. Eng. Chem. Fund.* **6** (3), 381–387.

Jeffery, G. B. 1922 The motion of ellipsoidal particles immersed in a viscous fluid. *P. Roy. Soc. A* **102** (715), 161–179.

Kerekes, R. J. 2006 Rheology of fibre suspensions in papermaking: An overview of recent research. *Nordic Pulp Paper Res. J.* **21**, 598–612.

Klinkenberg, J., de Lange, H. C. & Brandt, L. 2011 Modal and non-modal stability of particle-laden channel flow. *Phys. Fluids* **23** (6).

Ko, G. H., Heo, K., Lee, K., Kim, D. S., Kim, C., Sohn, Y. & Choi, M. 2007 An experimental study on the pressure drop of nanofluids containing carbon nanotubes in a horizontal tube. *Int. J. Heat. Mass. Tran.* **50** (23–24), 4749–4753.

Krochak, P., Holm, R. & Söderberg, D. 2011 Drag reduction characteristics of micro-fibrillated cellulose suspensions. In *Paper Conference and Trade Show 2011, PaperCon 2011*, , vol. 1, pp. 347–356.

Kvick, M., Lundell, F., Prahl Wittberg, L. & Söderberg, L. D. 2013*a* Effect of fibres on hydrodynamic stability in a curved rotating channel. In *8th Int. Conf. on Multiphase Flow*, *ICMF2013* 674. Jeju, Korea.

Kvick, M., Lundell, F., Prahl Wittberg, L. & Söderberg, L. D. 2013*b* Effect of fibrils on curvature- and rotation-induced hydrodynamic stability. *Acta Mech.* **224** (10), 2249–2261.

Leal, L. & Hinch, E. 1973 Theoretical studies of a suspension of rigid particles affected by brownian couples. *Rheologica Acta* **12** (2), 127–132.

Lipscomb II, G., Denn, M., Hur, D. & Boger, D. 1988 The flow of fiber suspensions in complex geometries. *J. Non-Newton Fluid Mech.* **26** (3), 297–325.

Nsom, B. 1996 Stability of fiber suspension flow in curved channel. *J. Phys. II* **6** (10), 1483–1492.

Ogata, S., Numakawa, T. & Kubo, T. 2011 Drag reduction of bacterial cellulose suspensions. *Adv. Mech. Eng.* **2011**.

Orszag, S. A. 1971 Accurate solution of the Orr-Sommerfeld stability equation. *J. Fluid Mech.* **50**, 689–703.

Pääkkö, M., Ankerfors, M., Kosonen, H., Nykänen, A., Ahola, S., Österberg, M., Ruokolainen, J., Laine, J., Larsson, P. T., Ikkala, O. & Lindström, T. 2007 Enzymatic hydrolysis combined with mechanical shearing and high-pressure homogenization for nanoscale cellulose fibrils and strong gels. *Biomacromolecules* **8** (6), 1934–1941.

Paschkewitz, J. S., Dubief, Y., Dimitropoulos, C. D., Shaqfeh, E. S. G. &

Moin, P. 2004 Numerical simulation of turbulent drag reduction using rigid fibres. *J. Fluid Mech.* **518**, 281–317.

Patel, V. C. & Head, M. R. 1969 Some observations on skin friction and velocity profiles in fully developed pipe and channel flows. *J. Fluid Mech.* **38**, 181–201.

Petrie, C. J. 1999 The rheology of fibre suspensions. *J. Non-Newton Fluid* **87** (2–3), 369–402.

Phan-Thien, N. & Graham, A. L. 1991 A new constitutive model for fibre suspensions: flow past a sphere. *Rheol. Acta* **30**, 44–57.

Radin, I., Zakin, J. L. & Patterson, G. K. 1975 Drag reduction in solid-fluid systems. *AIChE J.* **21** (2), 358–371.

Reddy, G. & Singh, R. 1985 Drag reduction effectiveness and shear stability of polymer-polymer and polymer-fibre mixtures in recirculatory turbulent flow of water. *Rheol. Acta* **24** (3), 296–311.

Reddy, S., Schmid, P. & Henningson, D. 1993 Pseudospectra of the orr-sommerfeld operator. *SIAM J. Appl. Math.* **53** (1), 15–47.

Saarinen, T., Haavisto, S., Sorvari, A., Salmela, J. & Seppälä, J. 2014 The effect of wall depletion on the rheology of microfibrillated cellulose water suspensions by optical coherence tomography. *Cellulose* **21** (3), 1261–1275.

Schmid, P. J. & Henningson, D. S. 2001 *Stability and Transition in Shear Flows*. Springer, New York.

Shaqfeh, E. S. G. & Fredrickson, G. H. 1990 The hydrodynamic stress in a suspension of rods. *Phys. Fluids A* **2** (1), 7–24.

Toms, B. A. 1948 Some observations on the flow of linear polymer solutions through straight tubes at large Reynolds numbers. In *Proceedings of the First International Congress on Rheology*, , vol. 2, pp. 135–141. North Holland Publication Company.

Trefethen, L. N., Trefethen, A. E., Reddy, S. C. & Driscoll, T. A. 1993 Hydrodynamic stability without eigenvalues. *Science* **261** (5121), 578–584.

Turbak, A., Snyder, F. & Sandberg, K. 1983 Microfibrillated cellulose, a new cellulose product: properties, uses, and commercial potential. In *J. Appl. Polym. Sci., Applied Polymer Symposium 37*.

Vaseleski, R. C. & Metzner, A. B. 1974 Drag reduction in the turbulent flow of fiber suspensions. *AIChE J.* **20** (2), 301–306.

Virk, P. S. 1975 Drag reduction fundamentals. *AIChE J.* **21** (4), 625–656.

Weideman, J. A. & Reddy, S. C. 2000 A MATLAB differentiation matrix suite. *ACM Trans Math Softw* **26** (4), 465–519.

White, C. M. & Mungal, M. G. 2008 Mechanics and prediction of turbulent drag reduction with polymer additives. *Annu. Rev. Fluid Mech.* **40** (1), 235–256.

Zhenjiang, Y., Jianzhong, L. & Zhaosheng, Y. 2004 Hydrodynamic instability of fiber suspensions in channel flows. *Fluid. Dyn. Res.* **34** (4), 251–271.

Paper 6

6

The stability of the flow in a flow-focusing device

By Mathias Kvick[1,2], Fredrik Lundell[1,2], Lisa Prahl Wittberg[1,2] & L. Daniel Söderberg[1]

[1] Wallenberg Wood Science Center, KTH Mechanics, Royal Institute of Technology, SE – 100 44, Stockholm, Sweden
[2] Linné Flow Centre, KTH Mechanics, Royal Institute of Technology, SE – 100 44, Stockholm, Sweden

Manuscript

The flow stability in a flow focusing device, *i.e.* an intersection of four orthogonal channels (three inlets and one outlet), is investigated experimentally. The stability of the flow is defined by the variation of the position of the interface between the core and sheet flows. It is found that the main parameter controlling the flow stability is the Reynolds number for the sheet flow, with only minor influence from the core flow Reynolds number, in agreement with the numerical results by Lashgari et al. (JFM:753, 2014). When varying the fluid in the core (two different viscosities and one non-Newtonian cellulose nanofibril dispersion), no changes in stability limits are observed., indicating the possibility to use any fluid when investigating similar flow situations. In order to stabilise the flow by delaying the creation of a recirculation bubble hypothesised to be responsible for the onset of oscillations of the core flow, two corners are rounded. However, this hypothesis is rejected as the core flow becomes oscillatory at lower sheet Reynolds numbers in the channel with rounded corners.

1. Introduction

Due to recent advancement in the use of a flow focusing device to align and assemble cellulose chains into a strong thread, see Håkansson *et al.* (2014), the stability in such a device is investigated. The flow focusing takes place at the junction of four channels, three inlets and one outlet. The convergence of the three flows causes an acceleration of the core flow, which can be controlled by the relative flow rates in the inlets.

Similar processes have been used in the production of droplets (Joanicot & Ajdari 2005), assembly of filaments (Brennich *et al.* 2011) and DNA (Pfohl *et al.* 2007) as well as mixing (Knight *et al.* 1998). The stability of these flow situations have been focused on mapping out regimes for the formation

of droplets (Gupta *et al.* 2009; Cramer *et al.* 2004; Utada *et al.* 2007; Guillot *et al.* 2007), which occur at much lower flow rates compared to the current study. Of more relevance to the current work is the study by Oliveira *et al.* (2012), who numerically studied the flow in a flow-focusing device using a finite volume method, comparing the results with experiment in a micro channel. The authors observed that, for creeping flow, above a critical ratio of the inlet velocities a stagnation point was generated causing central vortices to appear. Inertia was found to decrease this critical velocity ratio in the Reynolds numbers range $0 - 210$ based on outlet channel quantities. However, at low velocity ratios (< 40) no vortices could be detected at any of the Reynolds numbers investigated, the velocity ratios are however much larger than in the current study.

These works has typically been carried out in channels of the order of 10 to 100 μm. However, lately when used as a production unit for the assembly of polymers, as in the cases of Håkansson *et al.* (2014) where a thread was formed out of cellulose fibrils or as in Kinahan *et al.* (2011) where silk fibres were assembled from silk protein fibroins, the height of the channel has been chosen to be between 400 μm and 1 mm.

The global linear stability, and the control thereof, in an x-junction was studied numerically by Lashgari *et al.* (2014). At a sufficiently high Reynolds number ($Re_s \approx 250$), based on the properties of the flow in the side channels, the core flow assumes a two-dimensional, steady, asymmetric mode appears, followed by a symmetric three-dimensional mode as the outer Reynolds number was further increased. Only minor effects could be observed from the variation of the velocity in the core flow. The two modes were found to appear when the recirculation zone at the beginning of the outlet channel reached a certain critical length. By applying suction/blowing at the walls, a delay of the first bifurcation to an asymmetric mode was achieved.

In the present study, the flow stability in a flow focusing device with large aspect ratio ($= 10$) is studied experimentally. The effect of the viscosity of the core fluid is investigated, two different viscosities are used as well as a non-Newtonian cellulose nanofibril dispersion. In order to control the stability of the flow, the effect of a modification of the corners in the device is investigated.

2. Experimental setup & methods

The experimental setup, depicted in Fig. 1, is made up by a 100×100 mm^2 centrepiece covered by side walls. In the $d = 10$ mm thick stainless steel centrepiece, channels with height $h = 1$ mm was cut out using wire cutting. On both sides of the centre piece, PMMA and aluminium parts provide optical access and rigidity. The flow in two different channels are investigated where the difference between the channels are the downstream corners at the junction where the three channels meet, the corners where the modification is done are

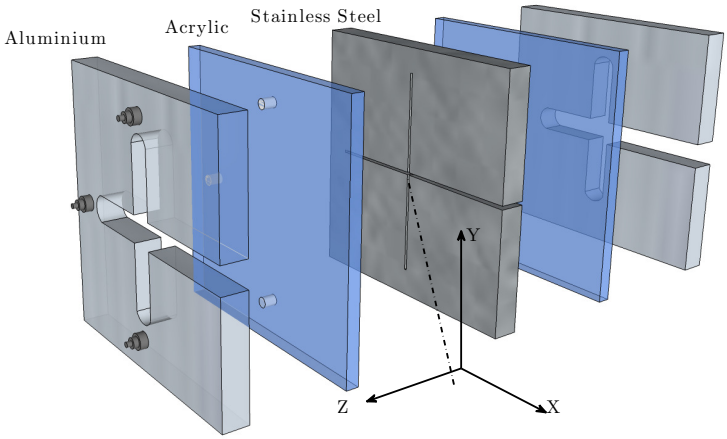

FIGURE 1. Sketch of the flow focusing device. The 10 mm thick stainless steel plate where the channels have been cut out, is covered by acrylic and aluminium sides.

in Fig. 2 marked by red circles, where the coordinate system and the flow rates are also defined.

In the reference channel (as in Håkansson *et al.* (2014) and Lashgari *et al.* (2014)) the corners have a 90 degree angle (down to machine precision $<$ 10 μm), while in the second channel the downstream corners have been manufactured with a radius of $Ra = 0.1$ mm.

The flow in the core is driven by syringe pumps (WPI Aladdin AL4000) while a constant pressure drop and a valve control the sheet flow. The flow rate is obtained by a load cell (HBM PW6DC3) measuring the total output from the channel over a period of time.

To visualise the core flow, and more importantly the interface between the core and the sheath flow, ink is mixed into the core liquid. Images of the flow are captured by a CCD-camera (Basler 32gm) connected to a microscope (Nikon SMZ1500) with applied backlight from a cold light source (Zeiss LCD K1500). The camera has a resolution of 1920×1080 pixels, providing a spatial resolution of approximately 100 pixels/mm corresponding to the minimum resolved scale 10 μm.

All channels have an inlet length of $50h$ before the junction, *i.e.* the location at which the channels converge. The non-dimensional numbers used to describe the flow in the channels are the Reynolds numbers for the core and sheath flow and the velocity ratio defined as:

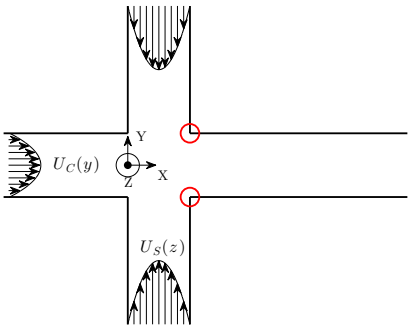

FIGURE 2. Definition of flow rates and coordinate system, the outlet is to the right. The two red circles mark the corners that will be modified in order to control the stability of the flow.

$$\mathrm{Re}_s = \frac{U_{s,max}\frac{h}{2}}{\nu_s} \tag{1}$$

$$\mathrm{Re}_c = \frac{U_{c,max}\frac{h}{2}}{\nu_s} \tag{2}$$

$$VR = \frac{U_{s,max}}{U_{c,max}}, \tag{3}$$

where ν_s is the viscosity of the fluid in the sheet, $U_{s,max}$ and $U_{c,max}$ are the maximum velocity in the core and side channels respectively (see Fig 2), calculated from the measured mean flow rate assuming parabolic velocity profiles, as:

$$U_{s,max} = \frac{3}{2}\frac{Q_s}{hd} \tag{4}$$

$$U_{c,max} = \frac{3}{2}\frac{Q_c}{hd}, \tag{5}$$

where Q_c is the flow rate of the syringe pump feeding the core flow and $Q_s = (Q_{tot} - Q_c)/2$ is the flow rate in each side channel obtained from the measured total flow rate Q_{tot}.

The interface between the flows was detected by thresholding the intensity in the images and tracing the boundary. Since ink was used in the core flow the two flows were easily distinguished. Several methods were tested in the analysis (spatial rms, temporal rms and mean divergence of core flow) and compared to what visually could be seen in the images. The temporal *rms* of the interface position was chosen as the most suitable method for quantification. The mean *rms* of the variation of the interface between images in a set is given by:

Case	Channel	Core fluid	Core fluid viscosity
A	α	Water-Glycerol	40 mPas
B	α	Water-Glycerol	20 mPas
C	α	CNF	see Fig 3
D	β	Water-Glycerol	40 mPas

TABLE 1. Summary of the different setups. In channel α all corners are right while in channel β the downstream corners have a radius of $Ra = 0.1$ mm.

$$y^*_{rms} = \frac{1}{N}\frac{1}{px}\sum_{n=1}^{N}\sum_{i=1}^{px}\sqrt{(y_i(n) - \bar{y}_i)^2}, \tag{6}$$

where N is the total number of images, px are all locations on the interface, $y_i(n)$ is the current y-position and $\bar{y}_i$ is the mean position at that location. y^*_{rms} is made non-dimensional by $y_{rms} = y^*_{rms}/h$. A high value indicates large fluctuations and zero means that the interface is steady.

The four different setups investigated are summarised in table 1, in all cases the fluid in the outer flow is water. The reference case (case A), around which variations are performed consists of a channel (α) where all corners are sharp and the fluid in the core flow had a constant viscosity of $\mu_c = 40$ mPas. In order to investigate the effect of viscosity, experiments were carried out with a reduced viscosity of the core fluid, $\mu_c = 20$ mPas. To investigate, whether control of the flow stability could be achieved with a modified channel (β), where the two downstream corners had a radius of $Ra = 0.1$ mm. In the fourth setup, the reference channel (α) was used and the fluid in the core was exchanged to a cellulose nanofibril suspension with a mass fraction of $c_m = 0.33\%$. Data from viscosity measurements of this suspension using concentric cylinders (Brookfield DV-II+Pro) are shown in Fig. 3.

In the design phase of the channel with rounded corners, 2-dimensional simulations were performed in COMSOL Multiphysics 4.4 for different radii of the corners. The boundary conditions were set to laminar inflow at the three inlets and zero pressure at the outlet, no slip was set on all boundaries.

3. Results

In Fig. 44 example images from the flow in the channel are shown. The top edge of the images is located at the entry of the core inlet. In the figure, the core and sheet Reynolds numbers are varied independently starting from a laminar reference case. By increasing the sheet Reynolds number (Re_s) as done in the bottom row, the core flow will start to oscillate. The frequency and

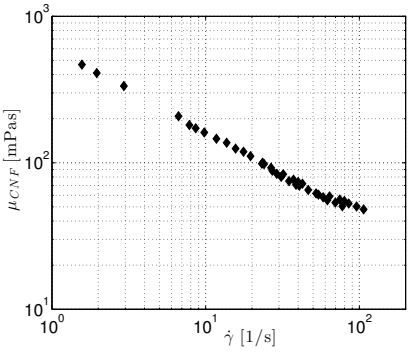

FIGURE 3. Viscosity of CNF suspension with the concentration $c_m = 0.33\%$.

wavelength at which the flow oscillates could not be captured by the current measurement method but image investigations indicated that the wavelength is greater than the image area. Further increasing the sheet Reynolds number lead to a breakup of the core flow and mixing of the two fluids. In the top row of Fig. ,4, the core Reynolds number (Re_c) is increased, and only small deviations of the interface from its stationary position could be observed at all core Reynolds numbers investigated (as long as Re_s was kept low enough).

However, when increasing Re_c, and keeping Re_s constant, the width of the core flow will increase. This is shown in Fig. 5, where the minimum width of the core flow, normalised with the height of the channel, is shown as a function of the velocity ratio. In the same figure the function λ, derived solely by mass continuity, is given by:

$$\lambda = \frac{1}{1 + 2\,VR}. \tag{7}$$

This function is similar to the one derived and experimentally confirmed by Cubaud & Mason (2008) if one disregards the difference in viscosity of the two fluids.

The time dependent position of the interface provides a good indication on whether or not the flow is stable. In Fig. 6, y_{rms} is shown for the reference channel with a constant viscosity liquid. The data is shown in the parameter plane spanned up by the two Reynolds numbers and the velocity ratio, following Lashgari *et al.* (2014). In Fig. 6a and Fig. 6b the core (Re_c) and sheet (Re_s) Reynolds numbers are varied, respectively. The data has in Fig. 6 (and in the following Fig. 8) been interpolated from the unstructured grid constructed by the measurement points onto a structured grid with 22 grid points in each direction. The interpolation was performed using a linear Delaunay triangulation. In Fig. 6b it can clearly be seen that there is a sharp increase in the *rms*

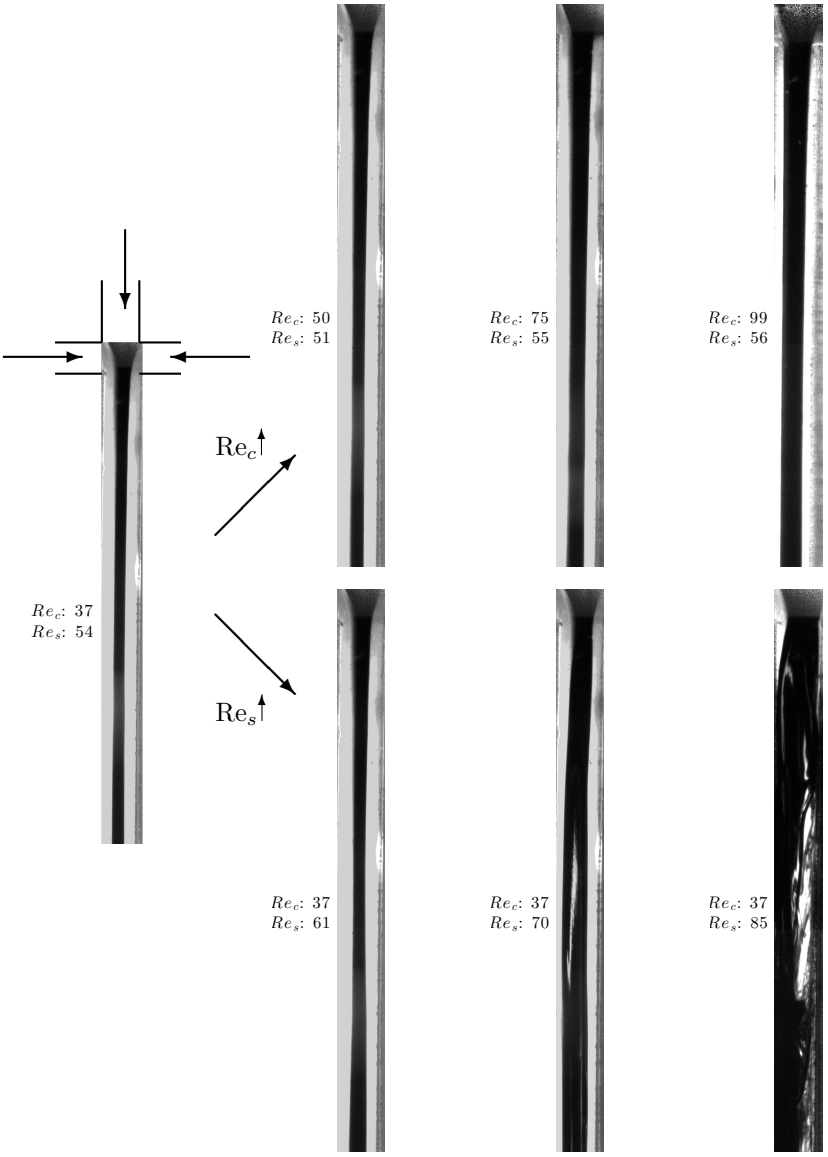

FIGURE 4. Examples of images captured of the flow. In the top and bottom rows, the core (Re_c) and sheet (Re_s) Reynolds numbers, are increased independently form the reference case to the left, where the location of the inlet is indicated.

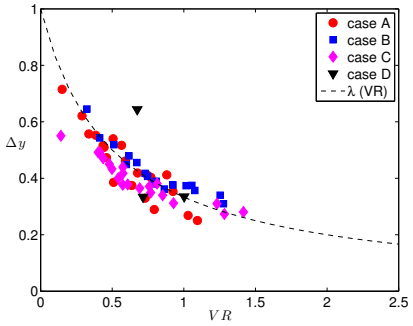

FIGURE 5. Normalised minimum width of the core flow as a function of the velocity ratio for flows with $y_{rms} < 0.01$.

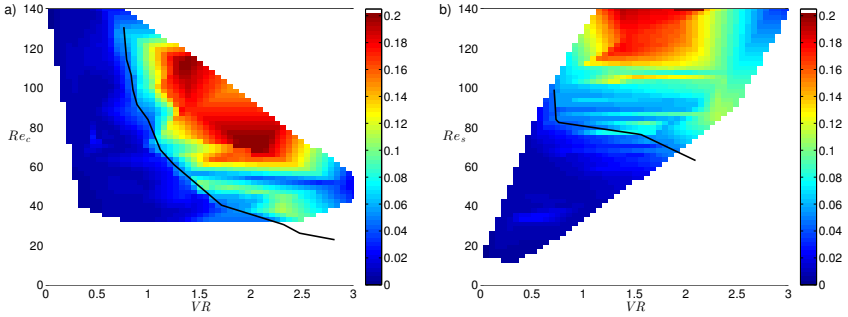

FIGURE 6. Temporal *rms* of the interface between the flows for the reference case A in the a) $\mathrm{Re}_c - VR$ plane and $\mathrm{Re}_s - VR$ plane. The solid lines are contours of $y_{rms} = 0.05$.

at $\mathrm{Re}_s \approx 70$ while the flow is only slightly affected by the increasing velocity ratio. In the two figures, the solid black line shows the contour of $y_{rms} = 0.05$.

In Fig. 8 y_{rms} in the $\mathrm{Re}_s - VR$plane are shown for the experiments with a lower viscosity fluid in the core flow (Fig. 8a) and the experiments with rounded downstream corners (Fig. 8b). The results from the simulations are displayed in Fig. 7a, where the length of the bubble, Δx is shown versus Re_s. In Fig. 7b streamlines from simulations of two different corner radii, $Ra = 0$ and $Ra = 0.1$ mm, are shown for a sheath Reynolds number $\mathrm{Re}_s = 90$. The creation of the recirculation bubble for a channel with sharp corners at $\mathrm{Re}_s \sim 50$ (as seen in Fig. 7a) compares fairly well with the onset of oscillations in the experiments. Assuming that the flow becomes unstable at a critical length of the recirculation bubble.

Based on the simulations, a radius of $Ra = 0.1$ mm should delay the formation of the recirculation bubble to $\mathrm{Re}_s \sim 125$. Therefore, a major difference in

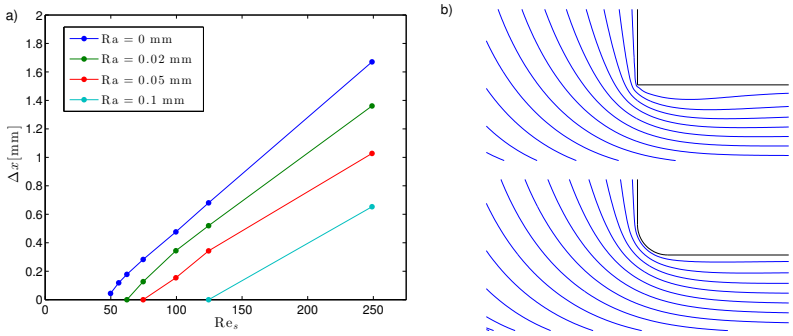

FIGURE 7. Results obtained from flow simulations in COMSOL Multiphysics. a) Length of recirculation bubble for different radii of the downstream corners versus sheath Reynolds number. b) Streamlines for equal flow conditions with $\mathrm{Re}_s = 90$ for channels with corner radius $Ra = 0$ and $Ra = 0.1$ mm.

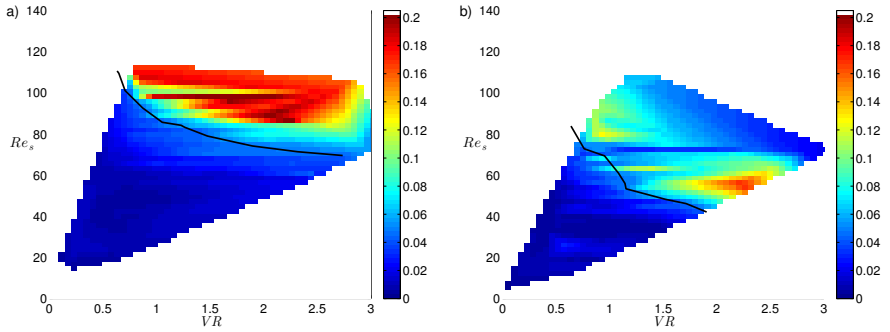

FIGURE 8. Temporal *rms* of the interface between the flows for a) case B with a core fluid viscosity of $\mu_c = 20$ mPas and b) case D where the downstream corners were manufactured with a radius of $Ra = 0.1$ mm.

the stability of the flow as compared to the reference case is expected. However, this is not found in the experiments, instead of increasing the stable region, the channel with rounded corners resulted in a destabilisation of the flow with increased y_{rms} at lower Re_s. However, even though the oscillations of the core flow starts at a lower Re_s, the maximum value is lower than in the other cases.

For case B, where the viscosity of the core fluid has been lowered, no effects on the flow dynamics can be observed.

In order to get a more detailed look on the differences between the cases, y_{rms} at a constant core flow Reynolds number ($\mathrm{Re}_c = 44$) is displayed in Fig. 9 versus the sheet Reynolds number. At around $\mathrm{Re}_s = 55$ a change in y_{rms} can be seen, indicating increasing levels of oscillations of the interface. It is also notable that the increase occurs earlier for the channel with rounded corners (case D in Fig. 9b) while for the case when CNF is used a slight delay is visible (case C in Fig. 9a).

4. Discussion & conclusions

The stability of the flow in a flow focusing device is studied experimentally. The parameter controlling the stability is found to be the sheet Reynolds number, qualitatively verifying the results of Lashgari *et al.* (2014). However, the Reynolds number at which the flow deviates from its laminar state differs by a factor of 5. The control of the stability was attempted by constructing a channel with rounded corners in order to delay the appearance of the recirculation bubble at the beginning of the outlet. Surprisingly the flow was not stabilised by this, if anything a destabilisation was seen. However, the oscillations observed at larger sheet Reynolds number are smaller than the reference case. Indicating that the modification to the channel resulted in a reduced growth of the recirculation bubble, thereby acting stabilising in that region. Furthermore, the change of fluid in the core, one with lower viscosity and one shear thinning, did not influence the flow stability.

To ensure that the stability of the flow is governed by the formation of a recirculation bubble, as suggested by Lashgari *et al.* (2014), more detailed measurements capturing the flow field in the channel are needed, *e.g.* through μPIV or other methods that are capable of capturing the dynamics of the flow. Simulations of 3-dimensional channels, investigating the effect of the side walls could also provide important insights into the flow stability in this and similar devices.

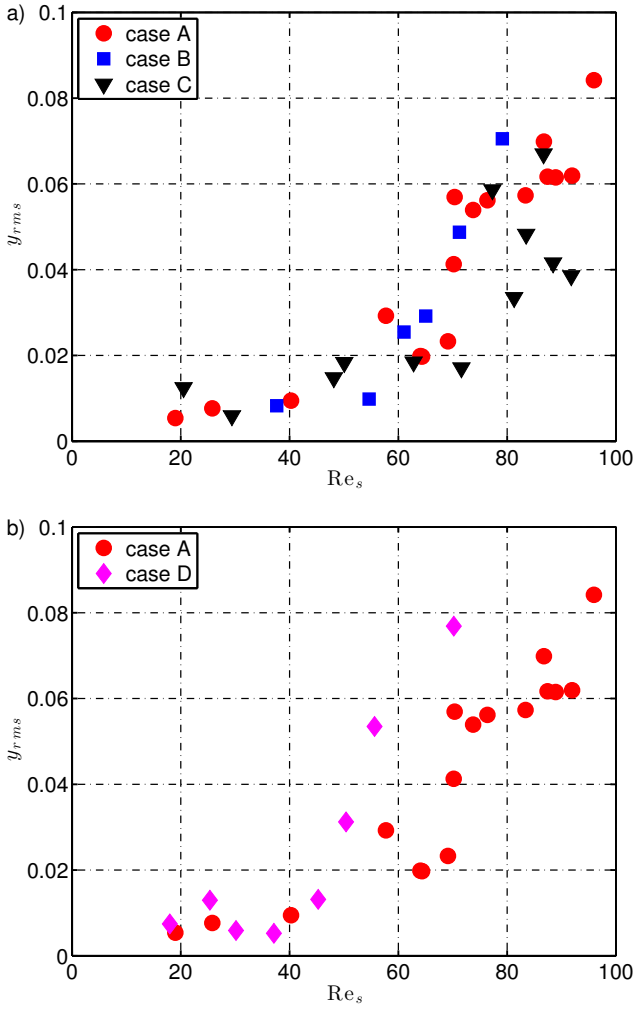

FIGURE 9. Temporal *rms* of the interface between the flows for with a constant core flow rate at $Q_1 = 35$ ml/min, corresponding to $\mathrm{Re}_c = 44$. In a) the reference case A, case B with a core fluid viscosity of $\mu_c = 20$ mPas and case C where CNF was used as the core liquid. In b) the reference case A and case D are shown, in case D the downstream corners where manufactured with a radius of $Ra = 0.1$ mm. All cases shown have a constant core flow rate at $Q_1 = 35$ ml/min, corresponding to $\mathrm{Re}_c = 44$.

References

Brennich, M. E., Nolting, J.-F., Dammann, C., Noding, B., Bauch, S., Hermann, H., Pfohl, T. & Koster, S. 2011 Dynamics of intermediate filament assembly followed in micro-flow by small angle X-ray scattering. *Lab Chip* **11**, 708–716.

Cramer, C., Fischer, P. & Windhab, E. J. 2004 Drop formation in a co-flowing ambient fluid. *Chem. Eng. Sci.* **59** (15), 3045–3058.

Cubaud, T. & Mason, T. G. 2008 Formation of miscible fluid microstructures by hydrodynamic focusing in plane geometries. *Phys. Rev. E* **78**, 056308.

Guillot, P., Colin, A., Utada, A. S. & Ajdari, A. 2007 Stability of a jet in confined pressure-driven biphasic flows at low reynolds numbers. *Phys. Rev. Lett.* **99**, 104502.

Gupta, A., Murshed, S. M. S. & Kumar, R. 2009 Droplet formation and stability of flows in a microfluidic t-junction. *Appl. Phys. Lett.* **94** (16).

Håkansson, K. M. O., Fall, A. B., Lundell, F., Yu, S., Krywka, C., V., R. S., Santoro, G., Kvick, M., Prahl Wittberg, L., Wågberg, L. & Söderberg, L. D. 2014 Hydrodynamic alignment and assembly of nanofibrils resulting in strong cellulose filaments. *Nat. Commun.* **5**, 4018.

Joanicot, M. & Ajdari, A. 2005 Droplet control for microfluidics. *Science* **309** (5736), 887–888.

Kinahan, M. E., Filippidi, E., Koster, S., Hu, X., Evans, H. M., Pfohl, T., Kaplan, D. L. & Wong, J. 2011 Tunable silk: Using microfluidics to fabricate silk fibers with controllable properties. *Biomacromolecules* **12** (5), 1504–1511.

Knight, J. B., Vishwanath, A., Brody, J. P. & Austin, R. H. 1998 Hydrodynamic focusing on a silicon chip: Mixing nanoliters in microseconds. *Phys. Rev. Lett* **80**, 3863–3866.

Lashgari, I., Tammisola, O., Citro, V., Juniper, M. P. & Brandt, L. 2014 The planar X-junction flow: stability analysis and control. *J. Fluid Mech.* **753**, 1–28.

Oliveira, M. S. N., Pinho, F. T. & Alves, M. A. 2012 Divergent streamlines and free vortices in Newtonian fluid flows in microfluidic flow-focusing devices. *J. Fluid Mech.* **711**, 171–191.

Pfohl, T., Otten, A., Köster, S., Dootz, R., Struth, B. & Evans, H. M. 2007

Highly packed and oriented DNA mesophases identified using in situ microfluidic X-ray microdiffraction. *Biomacromolecules* **8** (7), 2167–2172.

Utada, A. S., Fernandez-Nieves, A., Stone, H. A. & Weitz, D. A. 2007 Dripping to jetting transitions in coflowing liquid streams. *Phys. Rev. Lett.* **99**, 094502.

Paper 7

7

Producing film from cellulose nanofibrils using a flow focusing device

By Mathias Kvick[1,2], Fredrik Lundell[1,2] & Daniel Söderberg[1]

[1] Wallenberg Wood Science Center, KTH Mechanics, Royal Institute of Technology, SE – 100 44, Stockholm, Sweden
[2] Linné Flow Centre, KTH Mechanics, Royal Institute of Technology, SE – 100 44, Stockholm, Sweden

Manuscript

The possibility to use a flow focusing device in order to produce transparent films from cellulose nanofibrils is demonstrated. The flow focusing device consists of two serial intersections of three inlet and one outlet channel each. Due to the acceleration at the intersections the fibres align in the flow direction, ions are thereafter allowed to diffuse into the CNF sheet and the structure is locked. The resulting film is transparent with an estimated thickness of 1 μm. The observed variation in thickness is believed to be to the low control of the film during the drying phase.

1. Introduction

It has earlier been shown by Håkansson *et al.* (2014) that it is possible to use flow focusing in order to produce strong threads out of cellulose nanofibrils (CNF). In such a device the flow can be used in order to control the orientation of the fibrils. In the current paper, the same process as described in Håkansson *et al.* (2014) is used used in a channel where the spanwise width of the channel is larger than the height, resulting in a sheet rather than the thread obtained in the case of square channels.

Similar units have been used previously to control elongated particles. Thangawng *et al.* (2009) used flow focusing to create fibres from polymethylmethacrylate with different cross sections, with flat fibres being thinner than one micrometer. In order to produce the different cross sections, different configurations of inlet channels where used to create an azimuthal flow around the PMMA solution, leading to edge effects on the fibres. Köster *et al.* (2008) used flow focusing to control the assembly of collagen fibrils, using a low pH-solution to cause a gellation of the collagen.

Films produced from CNF, pure or as part of a composite, have the possibility to (partly) replace various products that are currently being manufactured

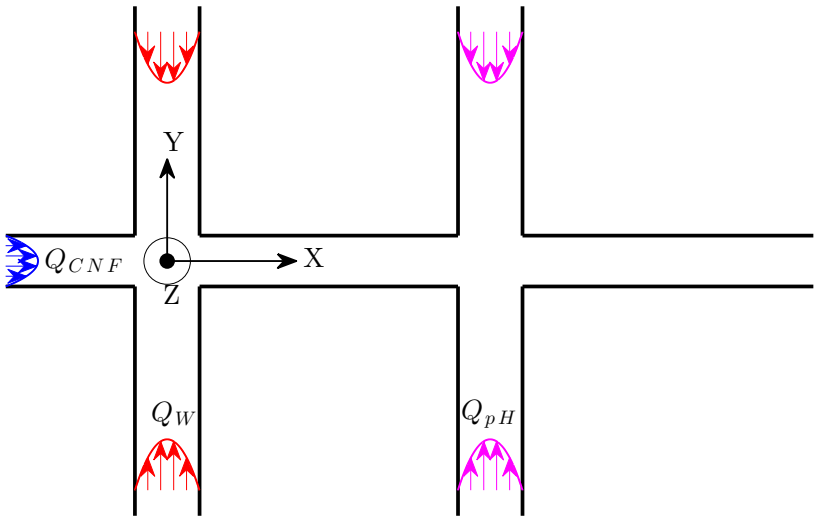

FIGURE 1. Schematic drawing of the flow focusing device.

from oil-based materials. Current research focuses on films where transparency (Nogi *et al.* 2009; Siró *et al.* 2011), strength (Syverud & Stenius 2009), water- and oxygen-barrier properties (Aulin *et al.* 2010; Galland *et al.* 2014) are investigated. The most common method when creating films from CNF is solvent casting, where the solution is left on a surface until the solvent has evaporated. In order to speed up the process, hot pressing has been used (Österberg *et al.* 2013).

In the current paper the method previously presented in Håkansson *et al.* (2014) is further developed in order to produce films with a controlled orientation in a continuos manner.

2. Method

The flow focusing device used in this case consists of two serial intersections with four perpendicular channels, where three channels in each intersection provides incoming flow and the fourth is the outlet as depicted in Fig. 2. At the intersections the core flow will be accelerated due to mass conservation. Since it is being accelerated by the outer flows and not by a change in geometry, the shear acting on the core fluid will be minimised. In the core channel a CNF dispersion with a concentration of $c = 3$ g/l is used. The CNF was prepared by liberating fibrils from bleached softwood pulp (Domsjö dissolving, Domsjö AB, Sweden). Before the liberation, the fibrils were carboxylmethylated, inducing a surface charge on the fibrils, this surface charge prevents the liberated fibrils from agglomerating (Wågberg *et al.* 1987). The liberation process follows the

protocol described by Fall *et al.* (2011), followed by a centrifugation of the dispersion at 4750 r.c.f, resulting in a dispersion with concentration 1 g/l which was increased by evaporation up to the 3 g/l.

The flows in the channels are driven by three syringe pumps (WPI, Al-4000). In the first intersection the CNF is covered by a sheath flow of water for lubrication purposes ($Q_{CNF} = 56$ mm^3/s and $Q_W = 28$ mm^3/s). In the second intersection a hydrochloric acid solution with $pH = 2$ is introduced from the side channels ($Q_{pH} = 222$ mm^3/s). The acceleration of the core flow will cause the fibrils in the CNF dispersion to align in the flow direction and keeping this alignment in the finished structure is of great interest for control of material properties.

The ions in the low pH solution will diffuse into the CNF dispersion, screening the individual fibrils surface charge, allowing them to come close together and bind to each other by Van der Waals forces (Fall *et al.* 2011). This results in a gel sheet that is advected into a bath with $pH = 2$ at the exit of the channel. The gel film is placed in a metal frame (a washer with inner diameter $d_f = 3$mm) to prevent shrinking during the drying stage. The film is then allowed to dry in air.

3. Results

After drying, the resulting film keeps its transparency, as shown in the upper image in Fig. 3. In the lower image in the same figure, the film is placed under monochromatic light with a wavelength $\lambda = 589$ nm. The diameter of the film are in both images $d_f = 3$ mm.

As explained in Håkansson *et al.* (2014), it is necessary to control the timescales associated with; (i) fibril alignment (t_{align}), (ii) ion diffusion into the film (t_{ion}), (iii) rotational Brownian diffusion of the fibrils from the aligned state (t_{rot}) and (iv) the convection to the exit of the device (t_{conv}). The timescales are in the following work estimated to be:

$$t_{align} \sim \frac{2h^2 d}{Q_{CNF}} = 0.4 \text{ s} \tag{1}$$

$$t_{ion} \sim \frac{\hat{t}_{ion} h^2}{D_{ion}} = 0.8 \text{ s} \tag{2}$$

$$t_{rot} \sim \frac{\Delta\phi^2}{D_{rot}} = 3.9 \text{ s} \tag{3}$$

$$t_{conv} \sim \frac{Lhd}{Q_{CNF} + 2Q_W + 2Q_{pH}} = 0.9 \text{ s}, \tag{4}$$

where $D_{ion} = 9.3 \times 10^{-9}$ m^2/s is the diffusivity of hydrogen in water, $\Delta\phi = 22.5^\circ$ is the maximum acceptable dealignment, $D_{rot} = 0.04$ rad^2/s is the rotational diffusivity (Håkansson *et al.* 2014), $L = 50$ mm is the length of the

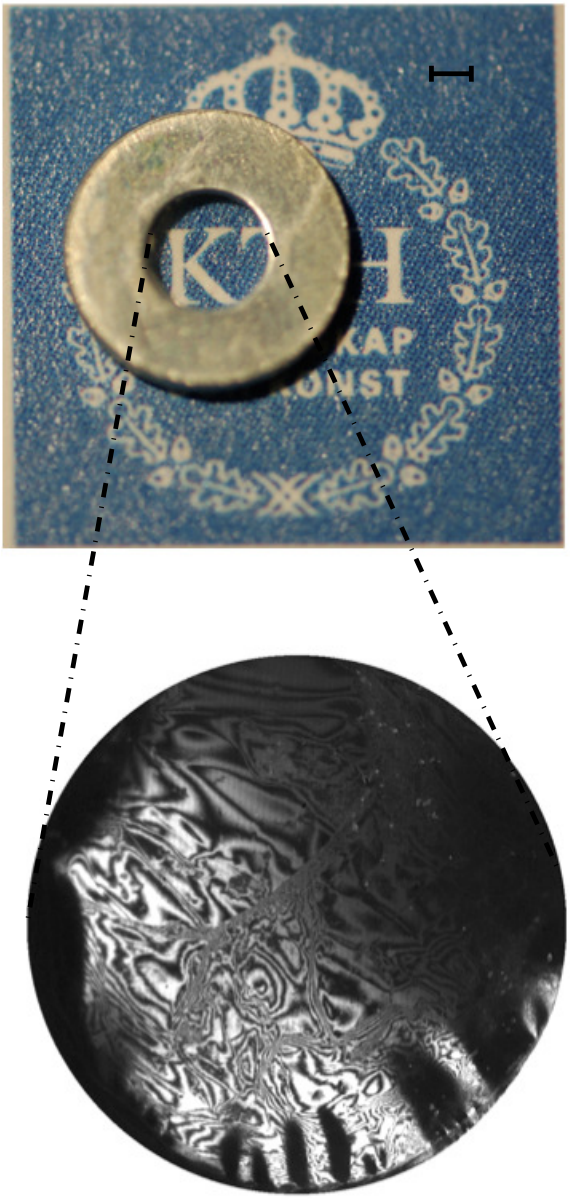

FIGURE 2. Picture of the resulting dried film placed over the hole in the washer, under white- (top) and monochromatic light (bottom). The scale bar in the top image is 1 mm.

outlet channel and $\hat{t}_{ion} = 0.00735$ is the non-dimensional time for the ion concentration to reach 10 mM in the centre of the film, estimated by solving the diffusion equation:

$$\frac{\partial \tilde{c}}{\partial \tilde{t}} = \frac{\partial^2 \tilde{c}}{\partial \tilde{y}^2}, \tag{5}$$

where the equation has been made non-dimensional with h, D_{ion} and the initial outer concentration. The partial differential equation was solved in MATLAB in the domain $0 \leq \tilde{y} \leq 0.5$ with symmetry and no flux boundary conditions, assuming a film thickness of $\tilde{y} = 0.2$ and that the film will gel at the non-dimensional concentration $\tilde{c} = 0.1$. From the timescales presented in Eqns. 1-4, it is clear that the conditions stated in Håkansson *et al.* (2014) as necessary in order to assemble the fibrils are met, *i.e.* $t_{align} < t_{ion} < t_{rot}$ and $t_{ion} < t_{conv}$.

In order to estimate the thickness of the film, an approximate calculation of the amount of material used and the contraction of the film during drying will be made. The volumetric flow rates previously given results in a mean velocity $U_m \approx 0.05$ m/s. The length of the film being $d_f = 3$ mm, the time it takes to produce this amount of film is $\Delta t = U_m/d_f = 0.05$ s, resulting in an amount of CNF dispersion used $V_{CNF} = Q_1 \Delta t = 3$ μl. With an area of the film as $A_f = 9$ mm^2, the height of the wet film is approximately $h_{wet} = 0.3$ mm. When drying the concentration goes from the initial $c = 0.3\%$ to consisting solely of CNF, giving a decrease of the height of approximately 300 times, since the film is not allowed to shrink in the plane. This provides an estimate of the thickness of the dried film of $h = 1$ μm. It is clear from the interference pattern in Fig. 3, that the thickness is not constant. However,

4. Discussion & Conclusions

A CNF film has been produced using flow focusing. Thus, the method earlier developed to manufacture filaments by Håkansson *et al.* (2014) is also applicable to 2-dimensional sheets. The film is estimated to have a thickness around 1 μm, where the variation seen in the interference pattern is believed to occur as a consequence of inhomogeneous drying.

Since this is a first attempt, no parameter studies are performed. Also the orientation of the fibrils in the film needs to be measured. It should be possible, when the correct parameter combinations have been found, to produce a continuous film from CNF with controlled orientation and thickness and thereby also a predefined strength or heat conductivity.

Acknowledgements

Tekn. Lic. Karl Håkansson at Wallenberg Wood Science Center, KTH Mechanics, is acknowledged for his comments and suggestions..

References

Aulin, C., Gällstedt, M. & Lindström, T. 2010 Oxygen and oil barrier properties of microfibrillated cellulose films and coatings. *Cellulose* **17** (3), 559–574.

Fall, A. B., Lindström, S. B., Sundman, O., Ödberg, L. & Wågberg, L. 2011 Colloidal stability of aqueous nanofibrillated cellulose dispersions. *Langmuir* **27** (18), 11332–11338.

Galland, S., Leterrier, Y., Nardi, T., Plummer, C. J. G., Månson, J. A. E. & Berglund, L. A. 2014 UV-cured cellulose nanofiber composites with moisture durable oxygen barrier properties. *J. Appl. Polym. Sci.* **131** (16).

Håkansson, K. M. O., Fall, A. B., Lundell, F., Yu, S., Krywka, C., V., R. S., Santoro, G., Kvick, M., Prahl Wittberg, L., Wågberg, L. & Söderberg, L. D. 2014 Hydrodynamic alignment and assembly of nano-fibrils resulting in strong cellulose filaments. *Nat. Commun.* **5**, 4018.

Köster, S., Evans, H. M., Wong, J. Y. & Pfohl, T. 2008 An in situ study of collagen self-assembly processes. *Biomacromolecules* **9** (1), 199–207.

Nogi, M., Iwamoto, S., Nakagaito, A. N. & Yano, H. 2009 Optically transparent nanofiber paper. *Adv. Mater.* **21** (16), 1595–1598.

Österberg, M., Vartiainen, J., Lucenius, J., Hippi, U., Seppälä, J., Serimaa, R. & Laine, J. 2013 A fast method to produce strong nfc films as a platform for barrier and functional materials. *ACS Appl. Mater. Interfaces* **5** (11), 4640–4647.

Siró, I., Plackett, D., Hedenqvist, M., Ankerfors, M. & Lindström, T. 2011 Highly transparent films from carboxymethylated microfibrillated cellulose: The effect of multiple homogenization steps on key properties. *J. Appl. Polym. Sci.* **119** (5), 2652–2660.

Syverud, K. & Stenius, P. 2009 Strength and barrier properties of mfc films. *Cellulose* **16** (1), 75–85.

Thangawng, A. L., Howell Jr, P. B., Richards, J. J., Erickson, J. S. & Ligler, F. S. 2009 A simple sheath-flow microfluidic device for micro/nanomanufacturing: fabrication of hydrodynamically shaped polymer fibers. *Lab Chip* **9**, 3126–3130.

Wågberg, L., Winter, L., Ödberg, L. & Lindström, T. 1987 On the charge stoichiometry upon adsorption of a cationic polyelectrolyte on cellulosic materials. *Colloids Surf.* **27** (4), 163 – 173.